CHARACTERIZING THE PHOTOCHEMICAL ENVIRONMENT OVER CHINA

A Dissertation
Presented to
The Academic Faculty

by

Zhen Liu

In Partial Fulfillment
of the Requirements for the Degree
Doctor of Philosophy in the
School of Earth and Atmospheric Sciences

Georgia Institute of Technology
May 2012

CHARACTERIZING THE PHOTOCHEMICAL ENVIRONMENT OVER CHINA

Approved by:

Dr.Yuhang Wang, Advisor
School of Earth and Atmospheric Sciences
Georgia Institute of Technology

Dr. Rodney Weber
School of Earth and Atmospheric Sciences
Georgia Institute of Technology

Dr. Greg Huey
School of Earth and Atmospheric Sciences
Georgia Institute of Technology

Dr. Armistread (Ted) Russell
School of Civil and Environmental Engineering & School of Earth and Atmospheric Sciences
Georgia Institute of Technology

Dr. Athanasios Nenes
School of Earth and Atmospheric Sciences
Georgia Institute of Technology

Date Approved: 14 March 2012

To Xiaolu

ACKNOWLEDGEMENTS

I would like to thank my Ph. D. thesis committee members Drs. Greg Huey, Athanasios Nenes, Ted Russell, and Rodney Weber, for their constructive comments and suggestions for my research during all kinds of occasions throughout the years of my Ph.D. study. Their visions and insights not only helped me better address the scientific problems, but also guided me to learn to think more critically and creatively as a scientist. Thank all the instructors of my courses at EAS, who have led me to know the mysterious atmospheric science. Thanks go to all the current members and alumni of Yuhang Wang's group, especially Dasa Gu, Ja-ho Koo, Charles Smeltzer, Ran Yin, Zhenzhen Yin, Yuzhong Zhang, Drs. Yongjia Song, Qing Yang, Tao Zeng and Chun Zhao. I thank them for all the scientific discussions in the office and all the good time we spent together. I also thank all my good friends at EAS, especially Dr. Arsineh Hecobian, Zheng Lu, Wenxian Zhang, and Jin Liao.

I would like to thank the CAREBeijing Experiment science team, especially Drs Greg Huey, Robert Stickel, and Jin Liao from Georgia Tech, Drs Min Shao, Tong Zhu, Limin Zeng from Peking University, China; Drs Chih-Chung Chang and Shaw-Chen Liu from RCEC, Academic Sinica, Taipei, China; Drs Antonio Amoroso and Francesca Costabile from CNR–IIA, Rome, Italy. The CAREBeijing dataset as a result of their great experimental work is the foundation of my thesis. I also thank Drs Mihalis Vrekoussis, Andreas Richter, Folkard Wittrock, and John P. Burrows from IUP, University of Bremen, Germany for providing the SCIAMACHY glyoxal data and all the useful

scientific discussions. Thank Drs Hongli Wang and Changhong Chen for providing the Shanghai VOC data.

Thank Xiaolu Zhang, my fiancée, and parents of mine and hers back in China. I work hard and enjoy my life because of all of you.

Lastly and most importantly, I sincerely thank Dr. Yuhang Wang, who is a great scientist and advisor and also a nice friend of mine. I thank him for trusting me and recruiting me 5 years ago, when I was graduating from Peking University with poor GPA, an average background, and a strong curiosity in atmospheric chemistry. On my journey of exploring atmospheric chemistry during my Ph.D., his guidance made my eyes open, my mind clear, and my efforts worthwhile. I hope I earned his trust through hard working in the past 4 years and I sincerely wish him all the best in future.

TABLE OF CONTENTS

LIST OF TABLES

LIST OF FIGURES

LIST OF SYMBOLS AND ABBREVIATIONS

Symbols

A_i	surface area of particles
C_{CHOCHO}	vertical column density of CHOCHO
D_g	gas phase molecular diffusion coefficient
L_N	radical loss rate due to OH + NO_2 reaction
L_R	radical loss rate due to RO_2 + R'O_2 reactions
L_{ON}	radical loss rate due to RO_2 + NO_x reactions excluding L_N
L_{OH-NO_2}	loss rates of OH due to reaction with NO_2
L_{OH-VOC}	loss rates of OH due to reaction with VOCs
$L(O_3)$	O_3 loss rate
r_a	aerodynamic resistance
r_b	resistance in the quasi-laminar layer near the surface
r_p	radius of particles
$P(O_3)$	O_3 production rate
Q	total primary source rate of RO_x radicals
γ	reactive uptake coefficient
ω	mean molecular speed in the air

Abbreviation

1-D	one-dimentional
3-D	three-dimentional

AOD	Aerosol Optical Depth
ATSR	Along Track Scanning Radiometer
CAREBeijing	Campaign for Air quality REsearch over Beijing
CIMS	Chemical Ionization Mass Spectrometer
CTM	Chemical Transport Model
DOAS	Differential Optical Absorption Spectroscopy
GC/MS	Gas chromatography–mass spectrometry
GFED	Global Fire Emissions Database
HONO	nitrous acid (HNO_2)
MACR	methacrolein (CH_2CCH_3CHO)
MEGAN	Model of Emissions of Gases and Aerosols from Nature
MGLY	methylglyoxal ($CH_3C(O)CHO$)
MODIS	Moderate Resolution Imaging Spectroradiometer
MOPITT	Measurement of Pollution in the Troposphere
MVK	methyl vinyl ketone ($CH_2CHC(O)CH_3$)
NCEP	Natonal Centers for Environmental Prediction
NCP	North China Plain
NNRP	NCEP/NCAR Reanalysis Product
NO_x	Nitrogen Oxides ($NO + NO_2$)
NO_y	reactive nitrogen compounds
NO_z	$NO_y - NO_x$
NP	Northeast Plain
OMI	Ozone Monitoring Instrument

OVOCs	oxygenated volatile organic compounds
Pa	Pascal
PA	peroxy acetyl radical
PAN	peroxy acetyl nitrate
PER	peroxide formation rate
ppbv	part per billion by volume
pptv	part per trillion by volume
PRD	Pearl River Delta
REAM-1D	the 1-D verision of Regional chemical transport Model
REAM-3D	the 3-D verision of Regional chemical transport Model
RO_x	$RO_2 + HO_2 + OH$
SB	Sichuan Basin
SCIAMACHY	Scanning Imaging Absorption spectrometer for Atmospheric CHartographY
VCD	Vertical Column Density
VOCs	volatile organic compounds
WRF	Weather Research Forecasting model

SUMMARY

The rapid rising anthropogenic emissions driven by economic growth over China have been documented by satellite observations and bottom-up inventories. The large abundance of nitrogen oxides ($NO_x \equiv NO + NO_2$) and volatile organic compounds (VOCs) over the region has led to elevated secondary photochemical pollutants, e.g. peroxy acetyl nitrates (PANs) and O_3, and caused severely degraded air quality. Furthermore, the increased emissions over China might also have contributed to the recent upward trends of tropospheric O_3 over the regions downwind of China. Nevertheless, recent studies suggest that the chemistry over polluted regions in China could not be fully understood by current knowledge of atmospheric chemistry and emission estimates over the region.

In order to understand the apparently unique photochemical environment over China, multi-scale modeling analyses facilitated by ground-level, aircraft and satellite observations have been conducted. Summertime photochemistry at Beijing is analyzed using a 1-D chemical transport model (REAM-1D) constrained by measurements of a full-suite of chemical tracers during CAREBeijing-2007 Experiment in August of 2007. During the experiment, PAN and HONO (especially during daytime) were observed with outstandingly high abundance. REAM-1D modeling results suggest that reactive aromatic VOCs are the major source (~75%) of PAN and methylglyoxal (MGLY) is the predominant intermediate that produces peroxy acetyl (PAN) radicals; downward transport of PAN from the upper boundary layer contributes as much as chemistry near the surface in the observed PAN concentrations. Detailed radical budget analyses reveal

the very fast RO_x (OH + HO_2 + RO_2) production, recycling and destruction driven by VOC oxidation and heterogeneous processes. Photolysis of HONO and oxygenated VOCs (OVOCs) are the major primary RO_x sources, and aerosol uptake of HO_2 is a large and uncertain radical loss term due to high loading of aerosols. O_3 production is also very fast and is found to be in the transition regime, where reduction of NO_x or VOCs could both reduce O_3. Given the important role of nitrous acid (HONO) and aromatic VOCs in the chemical system, their sources and regional implications are investigated. Analysis of the observations and REAM-1D modeling consistently suggest that photoenhanced aerosol surface uptake of NO_2 is the predominant HONO source during daytime (~70%), followed by ground uptake of NO_2 and the gas-phase HONO source. Results from REAM-3D modeling show that such an aerosol heterogeneous HONO source could lead to notable (up to 50%) enhancement of regional hydroxyl radical (OH) level over central and southern China. REAM-3D modeling analyses of tropospheric vertical column densities of glyoxal (CHOCHO) from SCIAMACHY show that anthropogenic emissions of aromatic VOCs are substantially underestimated (by a factor of 5 – 6, regionally varied) over China. Such an underestimation is the main cause of a large missing source of CHOCHO over the region in current global models, and could also partly explain the underestimation of organic aerosols in previous modeling studies.

INTRODUCTION

1.1 Statement of problem

1.1.1 The increasing emissions over China and the rising trends of tropospheric O_3

Tropospheric O_3 is an important trace gas that has adverse impact on human health and ecosystems, and it also has greenhouse effect. Increased emissions of NO_x ($NO+NO_2$) and volatile organic compounds (VOCs) driven by the fast economic developments in China have been documented by both satellite observations [Richter et al., 2005] and bottom-up inventories [Ohara et al., 2007; Q Zhang et al., 2007; 2009]. The large abundance of NO_x and VOCs has led to elevated O_3 levels at both local [Shao et al., 2009; T Wang et al., 2006] and regional [C Zhao et al., 2009a] scales. Pollution outflow from this region can also affect air quality over regions downwind through long range transport [Cooper et al., 2010; Jacob et al., 1999; Y H Wang et al., 2006; Wilkening et al., 2000; L Zhang et al., 2009]. Increasing O_3 trends in the last two decades have been observed at the surface over China [T Wang et al., 2009], Japan [Tanimoto et al., 2009], in the marine boundary layer of the East Pacific Coast and Europe [Parrish et al., 2009], and even in the free troposphere over the western North America [Cooper et al., 2010]. Some of these studies suggest that the growing emissions of O_3 precursors over China may be a major contributor to such worldwide observed rising O_3 trends [Cooper et al., 2010].

Nevertheless, mechanistic and quantitative understanding of the impact of growing Asian emissions on tropospheric O_3 trends is still incomplete [Tanimoto et al., 2009]. As a matter of fact, none of those observed trends has been well reproduced by chemical transport model (CTMs) using current estimates of emissions and knowledge of

chemistry. Improved knowledge of emissions and chemistry of O_3 precursors in China is necessary to better understand their impacts on O_3 trends downwind of China and on the global tropospheric background O_3 levels.

1.1.2 Uncertainties in chemistry and emissions over China: lessons learnt from previous observations over the region

Chemistry

Recent observation studies have suggested that the chemistry over polluted regions in China may be much more complex than expected [Hofzumahaus et al., 2009]. For example, very large unknown daytime nitrous acid (HONO) source were inferred from observations at a rural site over Pearl River Delta (PRD) [Su et al., 2008]. Such excess HONO from acts as the most important primary source of hydroxyl radical (OH), and OH is the predominant oxidant and cleansing power in the troposphere. Missing such a HONO source and thus primary OH source in CTMs would cause incorrect representation of model sensitivity associated with chemistry. Furthermore, the VOC chemistry is highly complex and uncertain. Hofzumahaus et al. [2009] found that current standard photochemistry could not explain the observed OH level at another rural polluted site over PRD. The reason for such unexpected high OH level remains to be elusive [Lu et al., 2012] and current imcomplete knowledge of VOC chemistry, especially with respect to radical cycling efficiency, is thought to be the cause.

Properly representing chemistry in current CTMs is critical in using these models to assess emission impact on secondary pollutants such as O_3. It appears that current representation of chemical environemnt over China has isssues, based on aforemented

observational evidence. Efforts are needed to explore the reasons of those model discrapancies to improve model representation of those important and yet unclear processes through parameterization.

Emissions

A critical input for CTMs is emission inventory. Compilation of emission inventories for VOCs and NO_x over China is a challenging endeavor due to incomplete data and complex sources of these pollutants. Unlike in other developed countries, e.g. the United States and European countries, where efforts in compilation, evaluation and usage of these emission inventories began much earlier and have become a routine exercise in emission monitoring and air quality modeling, research-quality domestic emission inventories for China had been absent until the most recent decade [Ohara et al., 2007; Streets et al., 2003]. Due to the complex situation over China and lack of reliable data used for compiling these emission inventories, uncertainties associated with these 'bottom-up' emission estimates are often very large [Y Zhao et al., 2011].

An alternative approach to estimate emissions is through inverse modeling, which is to utilize the growingly available in situ [Palmer et al., 2003] and satellite [Martin et al., 2003] observations to generate a 'top-down' estimate and further develop an optimized emission estimate based on uncertainties in the 'top-down' and 'bottom-up' emissions, respectively. Inversion modeling technique has been successfully applied on a global scale [Martin et al., 2003], and also on regional scale to improve emissions of NO_x [C Zhao and Wang, 2009], carbon monoxide (CO) [Palmer et al., 2003], and VOCs [Fu et al., 2007].

Inverting NO_x and CO emissions is more straightforward problems than inverting VOCs. As such, current estimates of NOx and CO emissions over China have been tested extensively against in situ and satellite data, whereas VOC emissions have not. A major challenge of inverting VOC emissions is the lack of observations and methods to constrain emissions of multiple VOC species at a time. Most previous studies have been focused on isoprene (C_5H_8) [Shim et al., 2005], which is mainly biogenic in origin and one of the most reactive VOC species in the troposphere. Inverting emissions of other VOC species, especially those important anthropogenic VOC species, such as aromatic VOCs is very important given the potentially very large uncertainties of the emissions of these species over China [Y Zhao et al., 2011].

1.1.3 Characterizing the photochemical environment over China

The photochemical environment is defined as the factors that regulate the observed concentrations of various chemical compounds, including those important oxidants and photochemical pollutants, such as O_3 and PAN. The photochemical environment is largely determined by three components, emissions, chemistry and transport. These three components are highly coupled and interacted in reality, and are represented by current CTMs by three operators, i.e. the emission operator, the chemistry operator, and the transport operator.

The overarching goal of this thesis is to better characterize the photochemical environment over China, i.e. to better understand emissions, chemistry and transport over polluted regions in China.

1.2 Unique features of the photochemical environment over China

1.2.1 Highly concentrated population and anthropogenic emissions

Many factors have shaped the unique atmospheric environment over China, including the unique geographic location, topography, population and emission distributions, land cover types and biogenic emission sources, etc.

Figure 1.1 shows the distribution of population over the globe and over China. It is well known that China is the country with the largest population in the world, while the habited areas mostly concentrate over the eastern part of the country. Highly populous areas include Northeast Plain (NP), East China Plain (ECP), Sichuan Basin (SB), PRD, and also the southeastern coastal regions.

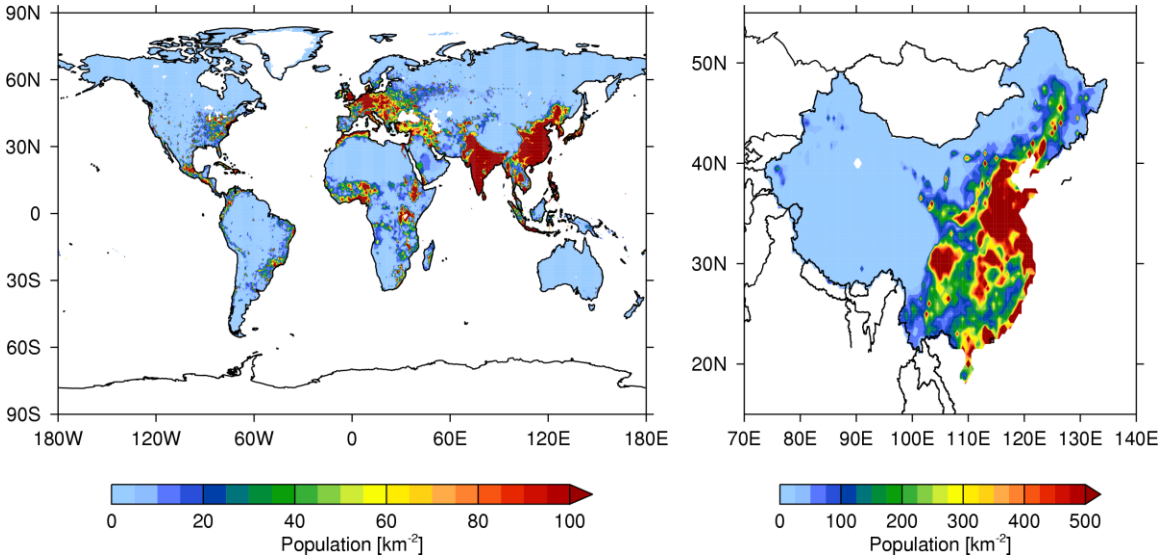

Figure 1.1 Population density (km^{-2}) over the globe and China

An inspection of distributions of anthropogenic emissions over China shows that most of those emissions have a spatial pattern that resembles the population distribution pattern. For example, Figure 1.2 shows the spatial distribution of tropospheric NO_2

columns from the Ozone Monitoring Instrument (OMI) (which has been used as an indicator of NO_x emissions) in August 2007. Enhanced OMI NO_2 columns mostly collocate with concentrated population. Such a spatial feature of anthropogenic emissions is typical for low to moderate developed regions, where emission amounts are largely proportional to magnitudes of production and consumption, which are mainly driven by population. It could also be found Figure 1.2 that ECP in China is in fact the largest region with highly concentrated large NO_2 abundance and thus NO_x emissions. This is quite different from other countries, where population and NO_x emissions are either not as large as in China or are less concentrated across an as large regional scale as over ECP in China. The highly concentrated anthropogenic emission driven by population is the first factor that defines the atmospheric chemical environment over the region.

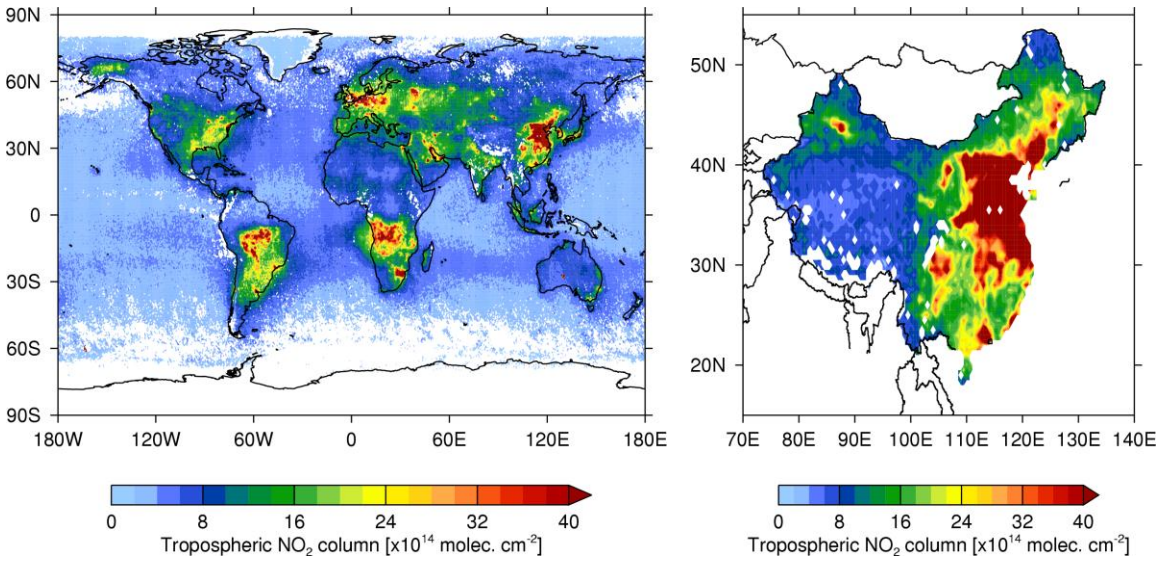

Figure 1.2 Tropospheric NO_2 columns from OMI in August 2007 over the globe and China.

1.2.2 Relatively low biogenic emissions over populous and polluted regions

O_3 precursors from natural sources such as isoprene and NO_x could be very important in contributing to O_3 pollution over regions with high vegetation coverage [Chameides et al., 1988]. Therefore, it is also crucial to assess the role and relative importance of biogenic and soil emissions over China. The role of soil NO_x over China has been assessed and constrained by seasonality of satellite observed NO_2 [Y X Wang et al., 2007]. Figure 1.3 shows isoprene emission fluxes on a global scale and over China during August of 2007 calculated by MEGANv2.1 model (http://tropo.aeronomie.be/models/ isoprene.htm) [Guenther et al., 2006; Müller et al., 2008].

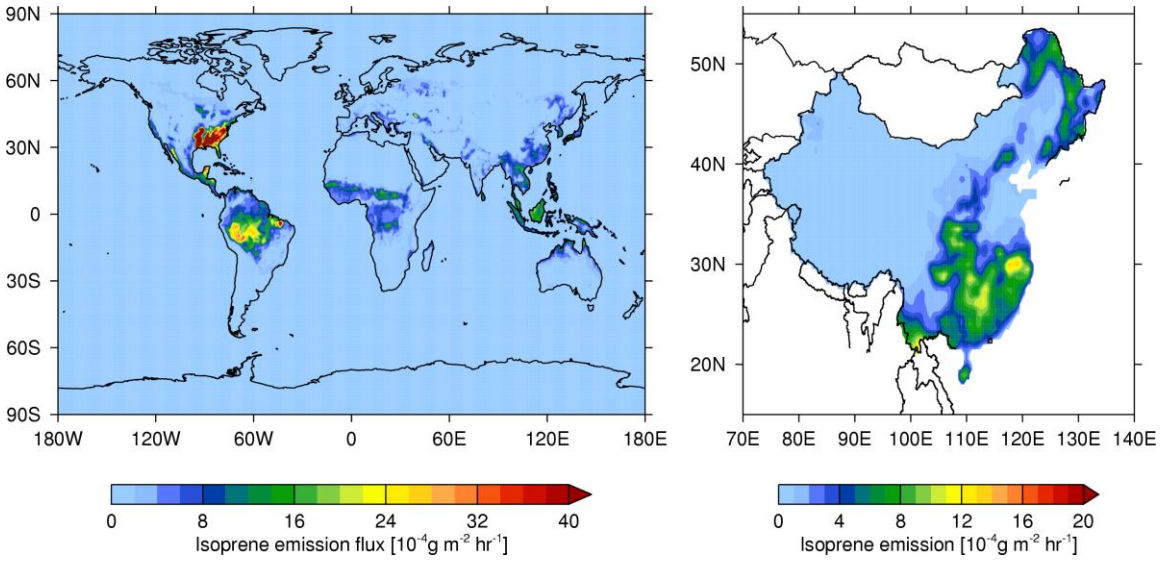

Figure 1.3 Biogenic isoprene emissions (MEGANv2.1) over the globe and China.

It is clear on Figure 1.3 that the most populous region over China – ECP is a region with relatively low isoprene emissions compared to other regions in China and also around the world. A closer inspection of Figure 1.3 indicates that isoprene emissions

over other polluted regions, such as SB, Yangtze River Delta (YRD), PRD and NP, are also not as high as the major isoprene emission region – the southern part of China. Therefore, it can be concluded from Figure 1.3 that those major populous and polluted regions over China generally have relatively low biogenic emission inputs. This is regarded as the second unique factor that contributes to define the photochemical environment over China.

1.2.3 The highest aerosol loading in the world

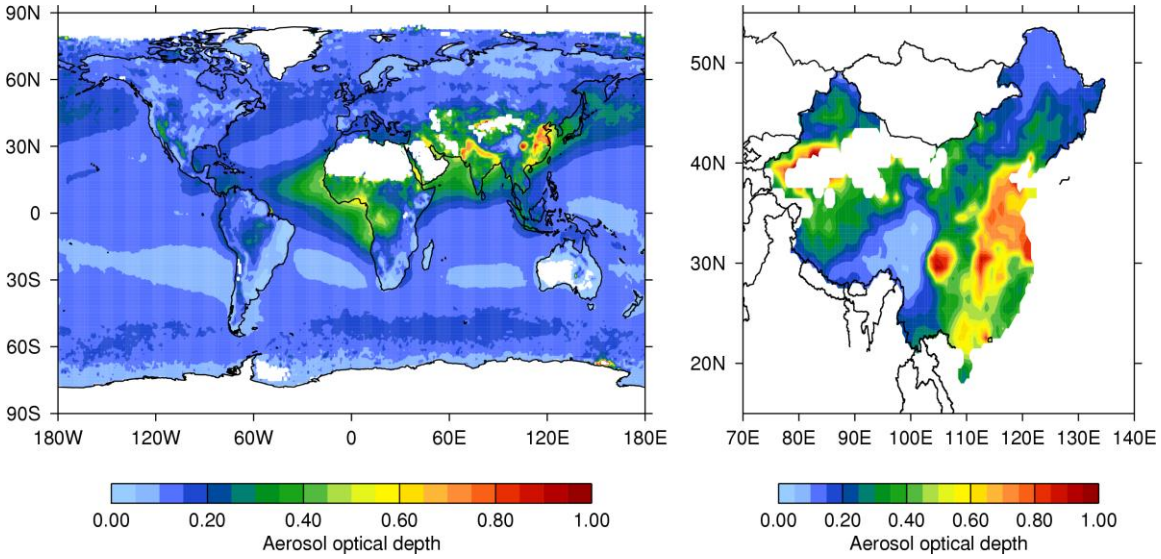

Figure 1.4 Long-term mean Terra MODIS aerosol optical depth (AOD) at 550nm over the globe and China during the years of 2001-2011.

Another important factor is the high aerosol loading over the China. The long-term mean spatial pattern of aerosol optical depth (AOD) at 550nm from Moderate Resolution Imaging Spectroradiometer (MODIS) on board the Terra satellite in Figure 1.4 shows that the eastern part of China is among the regions with the largest aerosol loading in the world. The finer spatial pattern of AOD resembles that of population and tropospheric NO_2, due in part to topographic impact and also in part to the collocating

sources of aerosols and NO_x. Such high loading of aerosols in the atmosphere could have substantial impact on chemistry via interference of solar radiation [Dickerson et al., 1997] and heterogeneous chemical reactions on aerosol surfaces [Jacob, 2000]. The first effect of aerosols will not be addressed in this work. Instead, the roles of various heterogeneous reactions in the chemical system over China will be assessed. The outstandingly high aerosol concentrations over polluted regions in China make heterogeneous reactions much more important than in other places.

In sum, three unique factors that contribute to form the photochemical environment over China are identified based on comparing the emissions and concentrations over China with other places in the world:

First, anthropogenic emissions over China are to a large extent driven by population, and thus are highly concentrated over those populous regions, including Northeast Plain (NP), East China Plain (ECP), Sichuan Basin (SB), PRD, and also the southeastern coastal regions. Some of these regions (e.g. NCP) are very large in spatial coverage.

Second, those high anthropogenic emission regions over China typically have relatively low biogenic emissions, implying the predominant role of anthropogenic emissions relative to biogenic emissions over these regions.

Third, the outstandingly large aerosol loading over polluted regions in China highlights the importance of heterogeneous reactions in the chemical system over these regions.

These unique features will be important context and prerequisite knowledge in characterizing and understanding the chemical environment over China.

1.3 Methodology: multi-scale modeling analysis

1.3.1 The multi-scale modeling framework

In this work, CTMs at multiple scales will be used in analyzing chemistry and emissions over China. The motivation and rationale of such a methodology are as follows.

First, a 1-D CTM constrained by observed chemical tracers is used to scrutinize chemical processes. The 1-D CTM resolves processes including chemistry, deposition, and vertical transport. By continuously constraining the model with observed chemical tracers near the ground level (the first layer of the model), chemistry and vertical transport of chemical species are reproduced based on information from the observation.

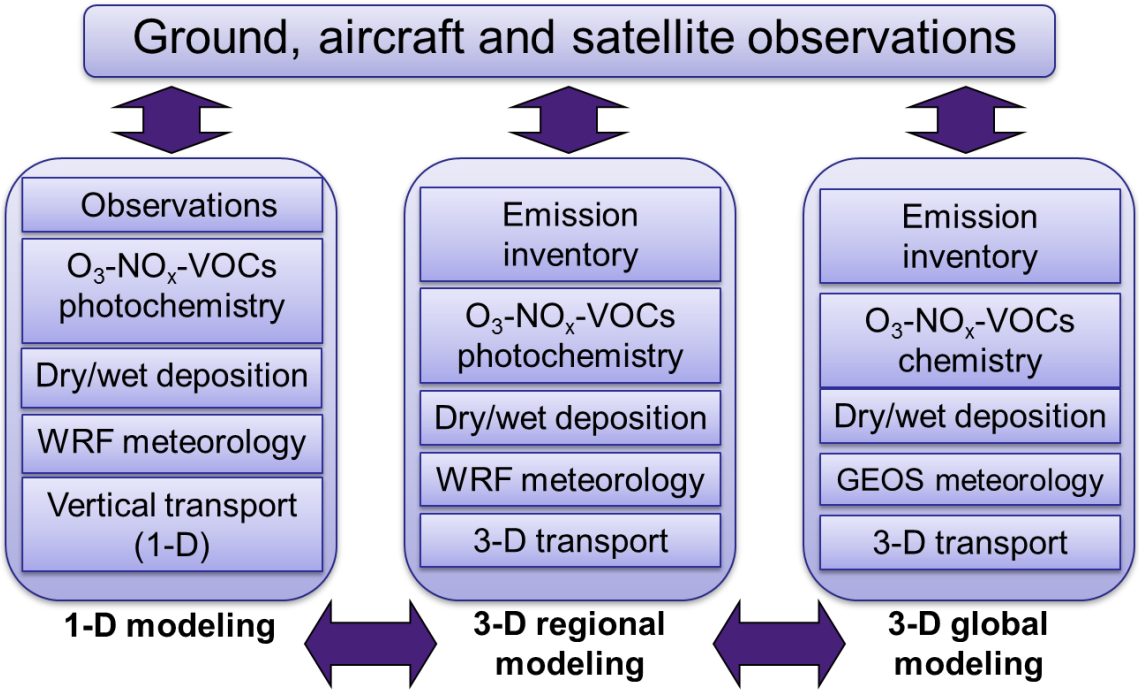

Figure 1.5 Schematic of multi-scale modeling analysis facilitated by observations

The scientific rationale of this 1-D model is the capability of isolating chemistry from emissions and allows examination of chemistry without interference from emission uncertainties. The main advantage of this 1-D model over traditional 0-D box model is its capability of resolving and quantifying the impact due to vertical transport on surface observed concentrations. Such a model setting assumes negligible contribution of horizontal transport on simulated concentrations. This assumption holds for short-lived secondary chemical compounds such as PAN, and also for radicals whose concentrations are maintained by chemistry only.

Second, a 3-D regional model is used to simulate emissions, chemistry and transport on a domain that covers the whole China mainland. The boundary conditions are taken from the global model GEOS-Chem [Bey et al., 2001]. The 3-D model is used to evaluate the accuracy of emission inventories, and to assess regional implications of findings on chemistry from the 1-D modeling analyses.

Both the 1-D and the 3-D models are driven by assimilated meteorological fields from the Weather Research and Forecast (WRF) model. Detailed descriptions of these two models are as follows.

1.3.2 The REAM-3D model

The 3-D REAM model has been applied over North America, East Asia and the polar regions [e.g., Choi et al., 2005; Wang et al., 2007; Choi et al., 2008ab; Zhao et al., 2009ab; Zhao and Wang, 2009; Zhao et al., 2010; Yang et al., 2011]. The model has a horizontal resolution of 70 km with 21 vertical layers in the troposphere. Transport is driven by WRF assimilated meteorological fields constrained by the NCEP reanalysis

products. Most meteorological inputs are archived every 30 min except those related to convective transport and lightning parameterizations, which are archived every 5 min. Chemical initial and boundary conditions for chemical tracers in REAM are obtained from the global simulation for the same period using the GEOS-CHEM model (v7-03-06) driven by GEOS-4 assimilated meteorological fields [Bey et al., 2001]. The chemistry of REAM is extended from that of standard GEOS-Chem by inclusion of aromatics, acetylene, and ethane. Biogenic emissions of isoprene and other species are based on MEGAN (v2.1) [Guenther et al., 2006]. Anthropogenic VOC emission inventory by Zhang et al. [2009] is used. The biomass burning emissions are obtained from the Global Fire Emissions Database, Version 2 (GFEDv2.1; available at http://daac.ornl.gov/).

1.3.3 The REAM-1D model

The REAM-1D model was developed recently based on the REAM-3D model. It shares the modules for O_3-NO_x-hydrocarbon photochemistry, vertical diffusion, convective transport, and wet/dry deposition [Liu et al., 2010] with the REAM-3D model. The chemical kinetics data were updated with the latest compilation by Sander et al. [2011], and the VOC chemistry in REAM-3D is expanded to include the chemistry of aromatics based on the SAPRC-07 chemical mechanism [Carter, 2009]. Vertical transport is driven by WRF assimilated meteorological fields based on the NCEP reanalysis data [Zhao et al., 2009a].

The model is constrained with measured CO, O_3, NO, HONO, NMHCs (C2–C9), OVOCs (acetone, acetaldehyde and formaldehyde) and aerosol surface areas and was run

with a 1–minute time step from 1 August to 30 August 2007. The results for the last 20 days were analyzed after a spin-up time of 10 days.

1.4 Descriptions of data

Multiple sets and types of data are used in this thesis to facilitate the modeling analysis. These data include (1) in situ measurements of a full suite of chemical tracers and physical parameters near the surface in Beijing during Campaigns of Air quality REsearch in Beijing (CAREBeijing) in August of 2007; (2) multiple sets of VOC ground measurements at Beijing, Shanghai and Backgarden of PRD; (3) satellite observations of glyoxal (CHOCHO) from SCanning Imaging Absorption SpectroMeter for Atmospheric CartograpHY (SCIAMACHY).

1.4.1 In situ measurements during the CAREBeijing-2007 Experiment

CAREBeijing-2007 Experiment is an intensive atmospheric observational campaign led by Peking University and occurred in August of 2007. Scientists from over 100 institutions around the world participated in the campaign and conducted comprehensive observations of the atmosphere in and surrounding Beijing. Figure 1.6 illustrates the geographical location of Beijing and two pictures taken on two contrasting days during the campaign, i.e. one clear day and one polluted day.

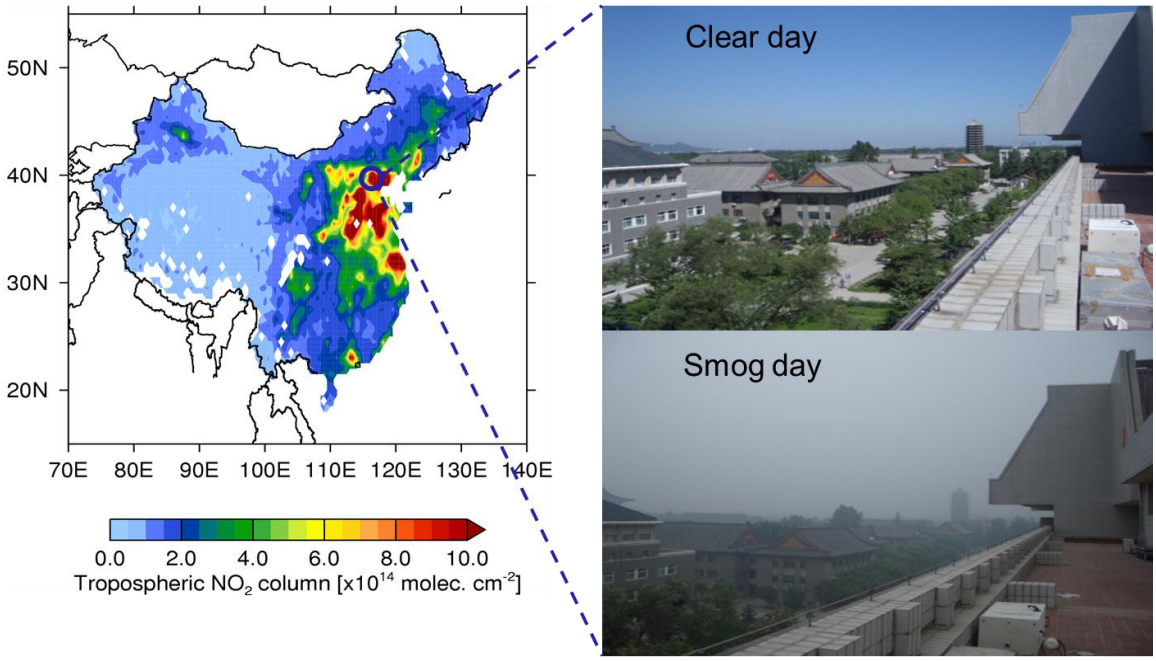

Figure 1.6 Geographical location of Beijing on top of a map of distribution of tropospheric NO_2 columns from OMI during August of 2007 (left) and the views from the sampling sites on the roof top of a building on Peking University campus.

During the CAREBeijing-2007 experiment [Zhu et al., 2009], a full suite of trace gases were measured concurrently in August 2007 at an urban site located on a building roof top (~20 m above the ground level) on the campus of Peking University (39.99 ℃N, 116.31 ℃E). Nitrogen monoxide (NO) was measured with a custom–made chemiluminescence detector [Ryerson et al., 2000]. Total reactive nitrogen compounds (NO_y, only gas phase) were measured by the conversion of the NO_y species to NO on a molybdenum converter operated at 300 ℃. PAN was measured using a chemical ionization mass spectrometer (CIMS) [Slusher et al., 2004]. HONO was measured with a liquid coil scrubbing/UV–VIS instrument [Amoroso et al., 2006]. O_3 and CO were measured by commercial instruments from the ECOTECH (EC9810 and EC9830). C_3–C_9 NMHCs were measured with a time resolution of 30 minutes using two online GC–FID/PID systems (Syntech Spectra GC–FID/PID GC955 series 600/800 VOC analyzer),

one for the C_3–C_5 NMHCs, and the other for C_6–C_9 NMHCs [Shao et al., 2009]. Another automated GC/MS/FID system was deployed to measure NMHCs in daytime (8:00–9:00 and 13:00–14:00) [Hofzumahaus et al., 2009]. OVOCs were measured using the PFPH–GC/MS method [Ho and Yu, 2004]. The uncertainties (1σ) for these measurements are estimated to be 5% for NO, O_3, CO, 3–5% for NMHCs, 10% for NO_y, PAN, HONO and OVOCs.

1.4.2 VOC measurements in Beijing, Shanghai and PRD

VOC observations at three sites, in Beijing (39.99 °N, 116.31 °E, August 2007), Shanghai (31.17 °N, 121.43 °E, July 2010) and the Back Garden site (23.5 °N, 113.03 °E, July 2006) over the Pearl River Delta (PRD), are used in the model evaluation. The first two are urban sites on the roof top of a building (~ 20 m above ground). The last one (~10 m above ground) is a remote site 60 km NW of Guangzhou. C2-C9 (or C12) VOC species were measured by online GC-FID/PID systems. The detection limits are 10-100 pptv and the estimated uncertainty is 5-10%.

1.4.3 SCIAMACHY CHOCHO vertical column densities (VCDs)

The differential optical absorption spectroscopy, DOAS, technique is applied to observations of the upwellingradition leaving the top of the atmosphere and measured by SCIAMACHY [Burrows et al., 1995, Bovennsmann et al., 1999 and references therein] glyoxal to retrieve CHOCHO VCD retrievals from SCIAMACHY using in the spectral window of 435-457 nm. The error comprises an absolute error of glyoxal VCDs of 2×10^{14} molecules cm^{-2} and the relative error is about 30%. For details of the retrieval processes, please refer to Vrekoussis et al. [2009].

1.5 Preliminary modeling analyses

1.5.1 Simulating PAN and HONO with the REAM-1D model

The standard version of the REAM-1D model is evaluated by comparing model simulated PAN and HONO with observations. Figure 1.7 shows that the model is not capable of simulating the observed concentrations, indicating important processes associated with PAN and HONO are not correctly represented or missing in the model. Since PAN is a secondary product from reaction between NO_x and oxygenated VOCs (OVOCs) and the model is constrained by observed NO_x and VOC concentrations, the model discrepancy of PAN suggests that some important OVOCs that are precursors of PAN are missing in the model. On the other hand, since the standard model only includes gas phase HONO chemistry, the severe underestimation of HONO in the standard model implies the predominant contribution from sources that is not in the gas phase. The missing sources of PAN and HONO are investigated in Chapter 2 and Chapter 3, respectively.

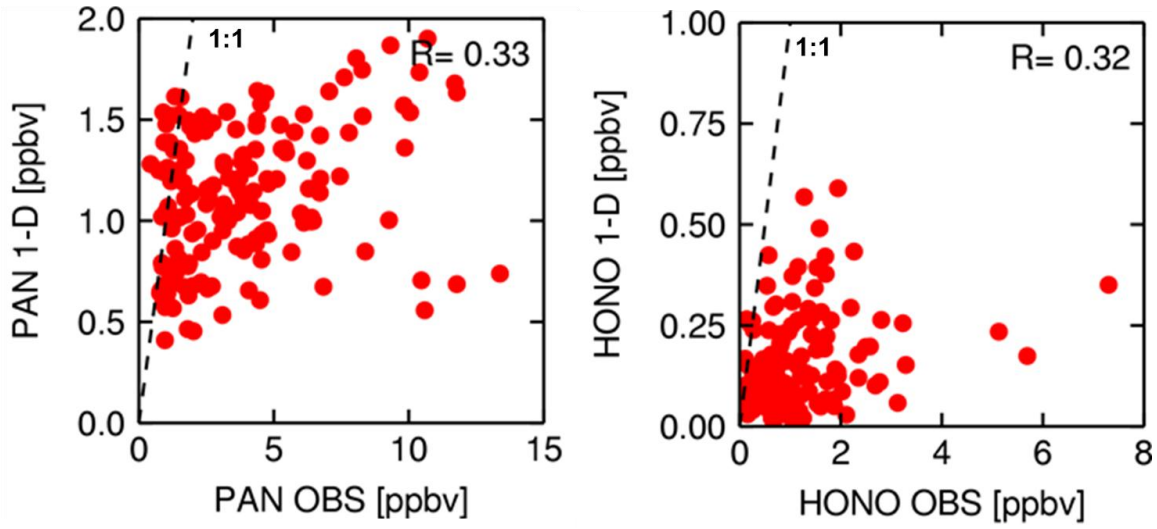

Figure 1.7 Observed versus model (REAM-1D) simulated PAN and HONO during daytime (6:00-18:00). The data points are showing hourly averaged concentrations from the observations and the model.

1.5.2 Simulating CO, NO_2 and glyoxal with the REAM-3D model

The REAM-3D model is evaluated against satellite observations of three species, i.e. CO, NO_2 and glyoxal. The model performance in simulating the former two allows evaluation of emissions of CO and NO_x in the model, whereas the model performance in simulating glyoxal is indicative for the ability of representing VOC emissions and chemistry.

Figure 1.8 shows that the model performance in simulating CO is generally good. It largely reproduces the spatial pattern of CO from Measurements Of Pollution In The Troposphere (MOPITT), while it underestimates CO in the southern China compared to MOPITT. This result indicates the CO emissions in the model are reasonable over most parts of China, except for the southern China.

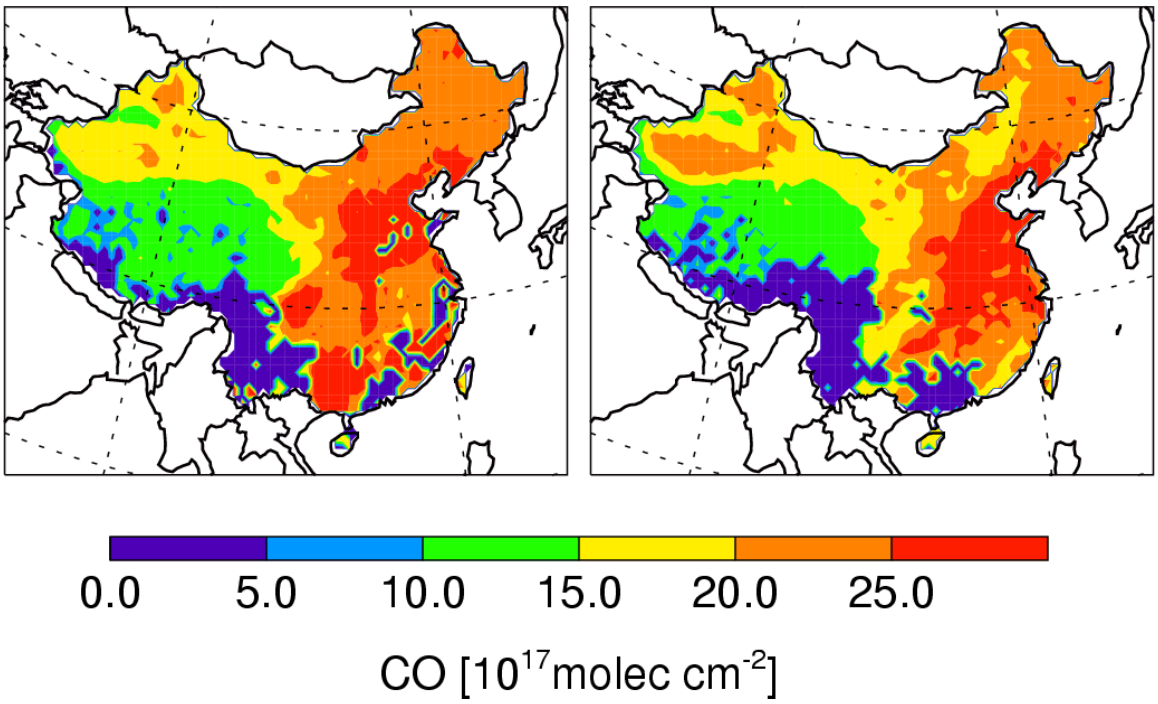

Figure 1.8 Monthly averaged vertical columns of CO over China from MOPITT and REAM-3D during August of 2007.

Figure 1.9 shows that the model reproduces the spatial pattern of NO_2 from OMI very well. This is understandable because the NO_x emissions in the model are from daily assimilated inversion results by Zhao and Wang [2009]. One of the major corrections through the inversion to the a priori emission of NO_x in Zhang et al. [2009] is on the emission spatial distribution. It was found that NO_x emissions over urban regions tend to be correct or overestimated, whereas those over rural regions are underestimated [Zhao and Wang et al., 2009]. The inverted emissions generated a new spatial distribution that allows current model to be in agreement with OMI.

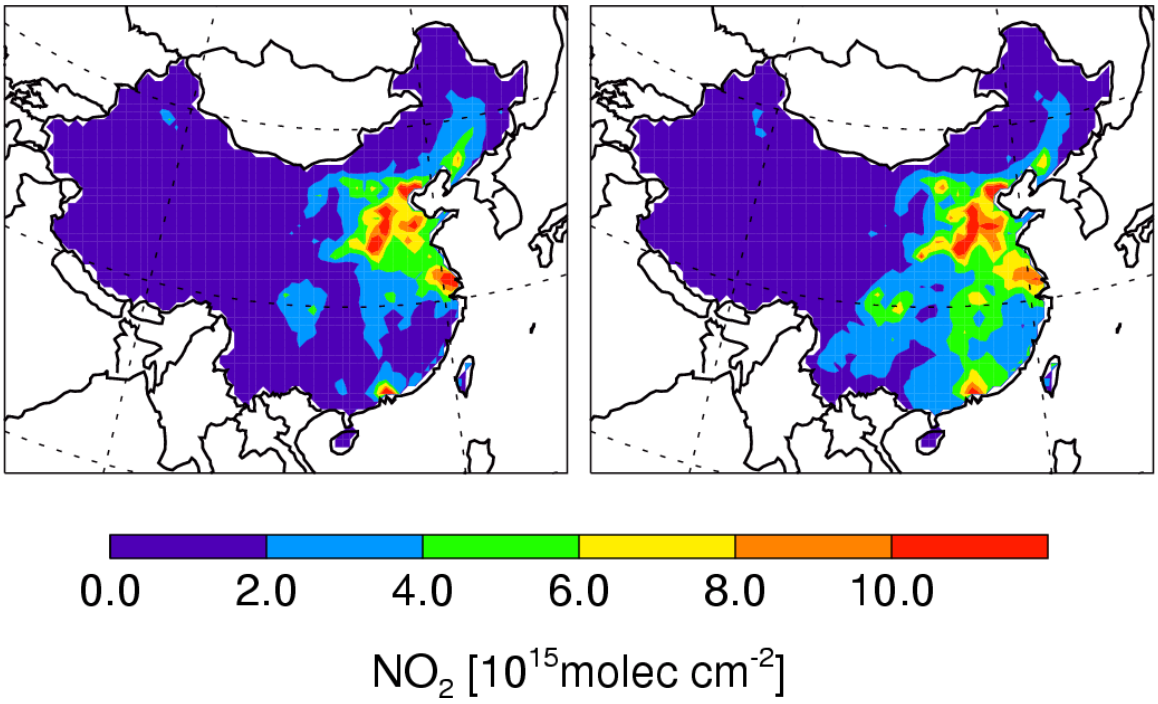

Figure 1.9 Monthly averaged vertical columns of NO_2 over China from OMI and REAM-3D during August of 2007.

Unlike the good model performance in simulating CO and NO_2, the model severely underestimated glyoxal compared to SCIAMACHY. The largest model biases are over those polluted regions, where the satellite can see elevated glyoxal levels whereas the model cannot. Over southern China where biogenic emissions are higher, the model performance is better. Considering glyoxal comes from both biogenic precursors and anthropogenic precursors and the fact that biogenic emissions are relatively low over polluted regions in China, as shown in Figure 1.2 and Figure 1.3, the model biases over those polluted regions may indicate biases in anthropogenic emissions of glyoxal precursors, such as acetylene, aromatics, etc. Furthermore, similar large model bias over China was found in previous global modeling studies of glyoxal budgets [e.g. Fu et al.,

2008]. Therefore, there seems to be a missing source of glyoxal in current CTMs that may indicate issues in VOC chemistry or emissions, (or both) over China.

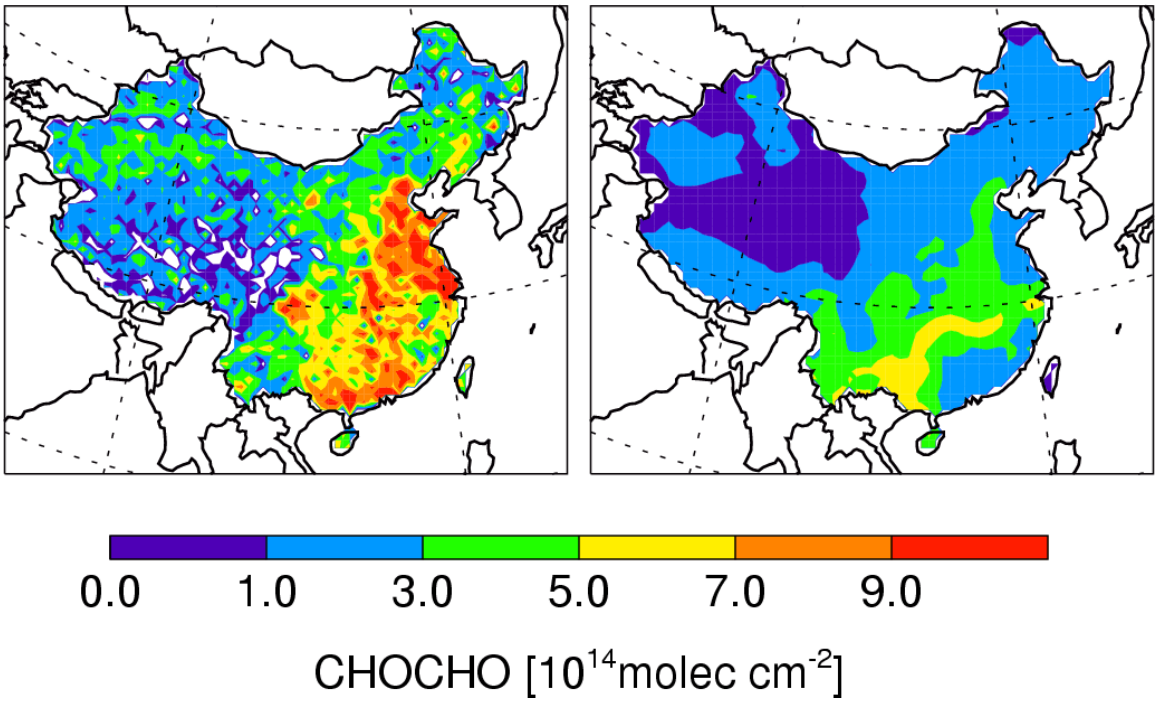

Figure 1.10 Monthly averaged vertical columns of CHOCHO over China from SCIAMACHY and REAM-3D during August of 2007.

Based on the above evaluation for REAM-3D model, it is concluded that the model is capable of simulating NOx and CO emissions and chemistry correctly. However, severe problems may exist regarding VOC emission, chemistry, or both. The missing source of glyoxal over China is investigated in Chapter 5.

1.6 Scope of this work

By conducting multi-scale modeling analysis, this dissertation (1) carefully examines the chemical system manifested by the measured concentrations from the in situ observations during the CAREBeijing-2007 experiment, and (2) evaluates VOC

emissions on a regional scale through modeling analysis of tropospheric CHOCHO columns from SCIAMACHY. CHOCHO is an oxidation product of many VOC species, including those from biogenic sources, e.g. isoprene, and also those from anthropogenic sources, e.g. aromatics, acetylene, and ethene, etc. Satellite observations of CHOCHO became available recently and have been validated through global modeling analysis and ground measurements of glyoxal [e.g. Fu et al., 2008].

Specifically, the following chapters are organized as follows.

Chapter 2, "Evidence of reactive aromatics as a major source of peroxy acetyl nitrate over China," describes the first attempt to use the newly developed REAM-1D model to analyze in situ measurements. Observation-based chemical budget analysis is applied to study the sources of PAN at Beijing. It is found that the model is capable of reproduce the observed PAN concentrations after incorporating chemistry of aromatic VOCs, which are neglected in current global and (to a lesser degree) regional CTMs. Reactive aromatics are found to be the major source of PAN at Beijing and probably over other polluted regions in China as well given the similar VOC compositions over these places. The 1-D model is also shown to be capable of simulating vertical transport of chemical tracers, and helps to identify the large contribution (~50%) from down-ward transport of PAN from the upper part of the boundary layer to the observed PAN near the surface. The success of this first attempt to use the REAM-1D model in studying chemical and transport sources of PAN at Beijing lends confidence in this model in simulating chemistry over polluted regions over China like Beijing. It is thereafter used in more detailed analysis of the chemical system to understand various chemical processes.

Chapter 3, "Summertime photochemistry during CAREBeijing-2007: RO_x budgets and O_3 formation," is a follow-up of the study presented in the first chapter. The capability of the REAM-1D model in simulating chemical processes over Beijing is evaluated during the study of PAN sources in the chapter 2. In chapter 3, a detailed analysis of RO_x (OH + HO_2 + RO_2) radical budgets is conducted to identify the key factors regulating the chemical system, especially the factors that lead to radical recycling, production, and losses. Those processes are likely to be unique for polluted regions in China and/or subject to large uncertainties due to incomplete knowledge are identified and discussed. Thereafter, the chemical budget of O_3 is analyzed to quantify the formation rate of O_3 in Beijing and its dependence on its precursors, i.e. NO_x and VOCs.

Chapter 4, "Evidence of photoenhanced aerosol uptake of NO_2 as the major daytime HONO source over China," addresses the missing source of HONO during daytime found in previous studies over China and in my modeling analysis. Observational evidence of the major HONO formation pathway is explored in the comprehensive data set during CAREBeijing experiment and modeling analysis is conduced to quantify contributions from different sources of HONO. Findings in this chapter will also help resolve the long-standing incomplete budget of HONO during daytime observed over the world by provide direct observational and modeling evidence from the region that is among those where the highest daytime level of HONO were observed in the past decade.

Chapter 5, "Exploring the missing source of glyoxal over China," assesses the accuracy of current standard VOC emission inventory [Zhang et al., 2009] that is being

used in current CTMs, using satellite observation of glyoxal and ground measurements of VOCs as constraints. This work is a supplement of previous extensive studies on constraining NO_x emissions over China using satellite. It helps to assess the ability of satellite observations in constraining the complex and uncertain VOC emissions, and evaluates a new methodology to use satellite observed glyoxal columns to obtain top-down estimates of VOC emissions.

Chapter 6, "Conclusions and future work," summarizes the findings in Chapter 2 – 5 and makes recommendations for future research on atmospheric chemistry over China.

2. [1]EVIDENCE OF REACTIVE AROMATICS AS A MAJOR SOURCE OF PEROXY ACETYL NITRATE OVER CHINA

2.1 Introduction

PAN ($CH_3C(O)OONO_2$) is one of the major components of photochemical smog, as well as an important player in atmospheric chemistry. It is formed by the reaction between acetyl peroxy (PA) radical ($CH_3C(O)OO$) and nitrogen dioxide (NO_2), and is removed mainly via thermal decomposition near the surface, with its lifetime ranging from less than one to several hours depending on the ambient temperature and the NO/NO_2 ratio [Roberts et al., 2007]. PA radical comes from photolysis or OH oxidation of a number of oxygenated volatile organic compounds (OVOCs), such as acetaldehyde (CH_3CHO), acetone (CH_3COCH_3), methyl vinyl ketone (MVK, $CH2CHC(O)CH_3$), methacrolein (MACR, CH_2CCH_3CHO), methylglyoxal (MGLY, $CH_3C(O)CHO$), and biacetyl ($CH_3C(O)C(O)CH_3$) [LaFranchi et al., 2009], which either form in situ by oxidation of various non–methane hydrocarbons (NMHCs) or are emitted from primary sources (e.g. acetaldehyde). The relative importance of PA radical precursors is highly variable depending on the composition of the NMHC and NO_x ($NO + NO_2$) mix [Bowman and Seinfeld, 1994; LaFranchi et al., 2009]. While acetaldehyde is often the dominant PA radical source over urban regions [Kondo et al., 2008; Roberts et al., 2001], isoprene oxidation products, e.g. MVK, MACR, and MGLY, usually play a significant role over regions with significant biogenic emissions [LaFranchi et al., 2009; Roberts et

[1] This chapter is an extension of "Evidence of reactive aromatics as a major source of peroxy acetyl nitrate over china," published on Environmental Science &Technology in 2010 (Environ. Sci. Technol., 44, 7017-7022). Co-authors are Yuhang Wang, Dasa Gu, Chun Zhao, L. Gregory Huey, Robert Stickel, Jin Liao, Min Shao, Tong Zhu, Limin Zeng, Shaw-Chen Liu, Chih-Chung Chang, Antonio Amoroso, and Francesca Costabile.

al., 2007]. Occasionally, OVOCs from aromatics and alkenes could be more important than acetaldehyde over some urban regions [E Grosjean et al., 2002]. Due to the much shorter lifetime of PAN than that of O_3 in the boundary layer, in situ measurements provide considerably better constraints for PAN chemistry than for O_3 chemistry, and analyzing PAN sources can provide insights into formation mechanisms of photochemical pollution.

Photochemical pollution has become an important air quality issue in China, due to increased emissions of NO_x and volatile organic compounds (VOCs) driven by the rapid economic growth. Remarkably elevated O_3 levels have been found at both local [T Wang et al., 2006] and regional [C Zhao et al., 2009a] scales. While more measurements of O_3 and its precursors become available [Chou et al., 2009; Shao et al., 2009; Y H Zhang et al., 2008], more detailed modeling analysis of the photochemistry and transport is desirable [Hofzumahaus et al., 2009; Lu et al., 2010].

PAN has been measured in many urban and suburban regions across the world [D Grosjean, 2003; Kondo et al., 2008; LaFranchi et al., 2009; Marley et al., 2007; Roberts et al., 2001; Roberts et al., 2007]. To our knowledge, PAN measurements and analysis of PAN photochemsitry in China are still sparse. Up to 10 ppbv of PAN has been observed at an urban site (the same site as ours) of Beijing [Shao et al., 2009]. Elevated PAN levels (up to 9 ppbv) have also been measured at a suburban site of Lanzhou in the western part of China, accompanied by moderate PAN levels (0.44 ± 0.16 ppbv) at a downwind remote site of Wuliguan, which was suggested to be mainly due to transport from Lanzhou [J M Zhang et al., 2009]. Recently, measurements of peroxyacetic acid were

reported in China and aromatics were identified as the major source (45%) of peroxyacetic acid [X Zhang et al., 2010].

In this work, we employ the 1–D version of a CTM (Regional chEmical and trAnsport Model, REAM) to analyze in situ measurements of a full suite of pollutants in Beijing, China, focusing on both photochemical and transport sources of PAN.

2.2 Methods

2.2.1 Measurement methods

Within the framework of the Campaign of Air Quality Research in Beijing 2007 (CAREBeijing–2007), a full suite of trace gases were measured simultaneously in August 2007 at an urban site in Beijing. The site is located on a building roof top (~20 m above the ground level) on the campus of Peking University (39.99 °N, 116.31 °E). Nitrogen monoxide (NO) was measured with a custom–made chemiluminescence detector [Ryerson et al., 2000]. Total reactive nitrogen compounds (NO_y, only gas phase) were measured by the conversion of the NO_y species to NO on a molybdenum converter operated at 300 °C. Laboratory tests show that the conversion efficiency for NO_2 and HNO_3 is measured to be larger than 95% and 85%, respectively. PAN was measured using a chemical ionization mass spectrometer (CIMS) [Slusher et al., 2004]. HONO was measured with a liquid coil scrubbing/UV–VIS instrument [Arnorosoa et al., 2006]. Under summer conditions at Beijing, interferences during sampling on the order of 2–9% of the measured HONO mixing ratios were observed and corrected using sodium carbonate denuders (supporting information) [Amoroso et al., 2008; Febo et al., 1993]. O_3 and CO were measured by commercial instruments from the ECOTECH (EC9810 and

EC9830). C3–C9 NMHCs were measured with a time resolution of 30 minutes using two online GC–FID/PID systems (Syntech Spectra GC–FID/PID GC955 series 600/800 VOC analyzer), one for the C3–C5 NMHCs, and the other for C6–C9 NMHCs [Shao et al., 2009]. Another automated GC/MS/FID system was deployed to measure NMHCs at daytime (8:00–9:00 and 13:00–14:00) [Hofzumahaus et al., 2009]. OVOCs were measured using the PFPH–GC/MS method [Ho and Yu, 2004]. The uncertainties (one standard deviation) for these measurements are estimated to be 5% for NO, O_3, CO, 3%–5% for NMHCs, 10% for NO_y, PAN, HONO and OVOCs. More detailed descriptions of the instruments and experimental methods are available in supporting information.

2.2.2 1-D REAM model

Previously, we have applied the 3–D Regional chEmical and trAnsport Model (REAM) to investigate O_3 photochemistry and transport at north mid-latitudes [Choi et al., 2005; Y. Choi et al., 2008; Yunsoo Choi et al., 2008; Y Wang et al., 2007; C Zhao and Wang, 2009; C Zhao et al., 2009b]. In this work, the 1–D version of the REAM model (1–D REAM), including the modules for O_3–NOx–hydrocarbon photochemistry, diffusion and convective transport, and wet/dry deposition, was used for analyzing the measurements in Beijing. The kinetic data were updated with the latest compilation [Sander et al., 2006]. The NMHC chemistry is expanded by including chemistry of aromatics based on the SAPRC–07 chemical mechanism (supporting information) [Carter, 2009]. Transport is simulated using the WRF assimilated meteorological fields based on the NCEP reanalysis data (supporting information) [C Zhao et al., 2009b]. In order to simulate PAN, the model is constrained with measured CO, O_3, NO, HONO,

NMHCs (C2–C9) and OVOCs (acetone, acetaldehyde and formaldehyde) at every 1–minute time step. Free radicals and other OVOC species that are also important in PAN chemistry but were not measured, such as MVK, MACR, MGLY and biacetyl, are simulated in the model, and we note that measurements of all these intermediates will further improve this type of study. We ran the model continuously from August 1 to 30, 2007 and results for the last 20 days were analyzed because PAN measurements are available for the last 20 days of the measurement period.

2.3 Results and discussions

2.3.1 Observed elevated PAN levels

The mean diurnal profiles of measured PAN, O_3, NO_y, NO, and HONO during August 10 to 30, 2007 are shown in Figure 2.1. The mean daily maximum PAN mixing ratio is 5 ppbv, occurring in the afternoon around 15:00, and the maximum during the measurement period reaches as high as 14 ppbv. Such abundance of PAN is comparable with that in Los Angeles during late 1980s [D Grosjean, 2003], and among the highest records in the past decade [Kondo et al., 2008; LaFranchi et al., 2009; Luke et al., 2010; Marley et al., 2007; Roberts et al., 2001; Roberts et al., 2007]. The lifetime of PAN (calculated based on simulated PAN concentrations and loss reaction rates) is very short at daytime (~0.5 hour), mainly due to high temperature at surface (28 ℃–38 ℃) and relatively large NO/NO_2 ratio (~0.5), which facilitate thermal decomposition of PAN and removal of PA radicals, respectively. Therefore, the large abundance of PAN at daytime indicates a large source of PA radicals from VOC oxidation and very fast photochemical processing in Beijing.

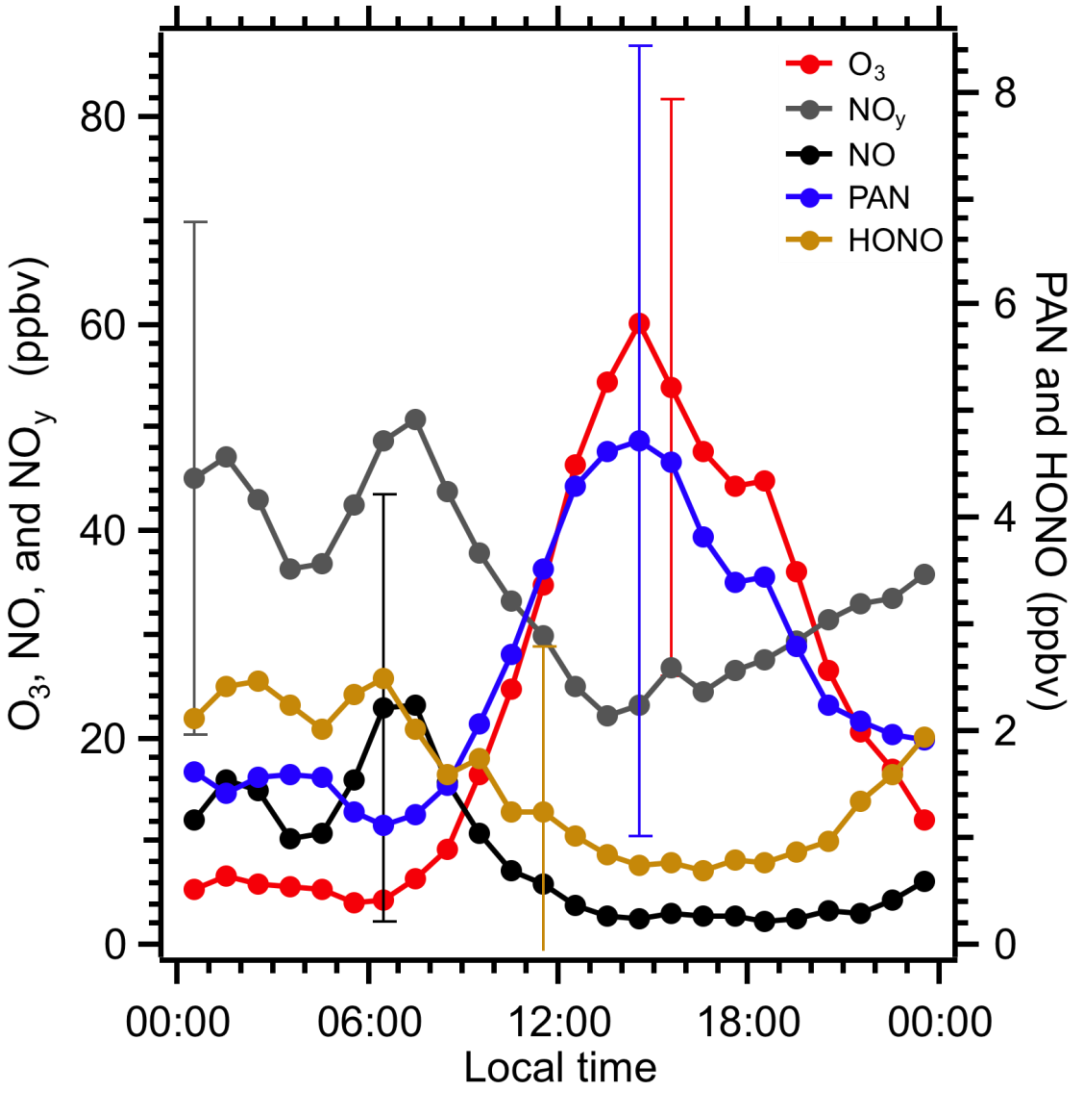

Figure 2.1 Average hourly diurnal profiles for measured O_3, NO_y and its components during 10–30 August 2007, including NO, HONO, PAN, together with corresponding standard deviations (only the largest hourly standard deviation for each species is shown).

Also notable are the observed high nighttime PAN levels (1–2 ppbv), which are among the highest in published literatures [Luke et al., 2010; Marley et al., 2007; J M Zhang et al., 2009]. After inspecting measurements from previous studies and this experiment, we found that the ratio of nighttime average to daytime peak value, i.e. 1.5

ppbv/5 ppbv in this work lies in the range of 0.2–0.35 of previous measurements, e.g. 1 ppbv/5 ppbv for Mexico City [Marley et al., 2007], 0.45 ppbv/2 ppbv for Lanzhou of China [J M Zhang et al., 2009], and 0.29 ppbv/0.91 ppbv for Houston [Luke et al., 2010], suggesting that the nighttime PAN levels are associated with the corresponding daytime magnitudes. The relatively long lifetime of PAN (2–5 hours) due to low temperature (e.g. 21 ℃–28 ℃ during our measurements) and larger NO_2/NO ratio, and shallow mixing layer are the two main factors leading to the continuous presence of PAN at night.

2.3.2 Daytime NO_y budget

We examined the closure of NO_y budget at daytime when photochemistry is active. Average daytime (9:00~18:00) NO_y budget comprised of measured (NO, PAN, HONO) and model predicted (NO_2, N_2O_5, HNO_4, and gaseous HNO_3) mixing ratios of NO_y species is shown in Figure 2.2. The budget is reasonably closed with ~10% NO_y not accounted for. Some of the error may lie in the model simulation of HNO_3, the lifetime of which is ~6 hours (against deposition to surface) longer than the other reactive nitrogen species. NO_z ($[NO_z] = [NO_y] – [NO_x]$) species together accounted for ~50% of total NO_y, consistent with a previous study in Beijing [Chou et al., 2009], suggesting the large abundance of oxidants from fast photochemical oxidation of NO_x. On average, PAN accounted for ~14% of total NO_y. From morning to afternoon, PAN percentage increases from ~5% to ~25% (Figure 2.1). It is also noteworthy that over 1 ppbv of HONO was observed at daytime (Figure 2.1), accounting for ~4% of the total NO_y (Figure 2.2). Such high levels of daytime HONO are significantly higher than other urban regions [Arnorosoa et al., 2006; Elshorbany et al., 2009b; Kanaya et al., 2007]. Analyses of

model results indicate that if assuming HONO is produced through heterogeneous processes [Gerecke et al., 1998; Kleffmann, 2007], photolysis of HONO contributes to

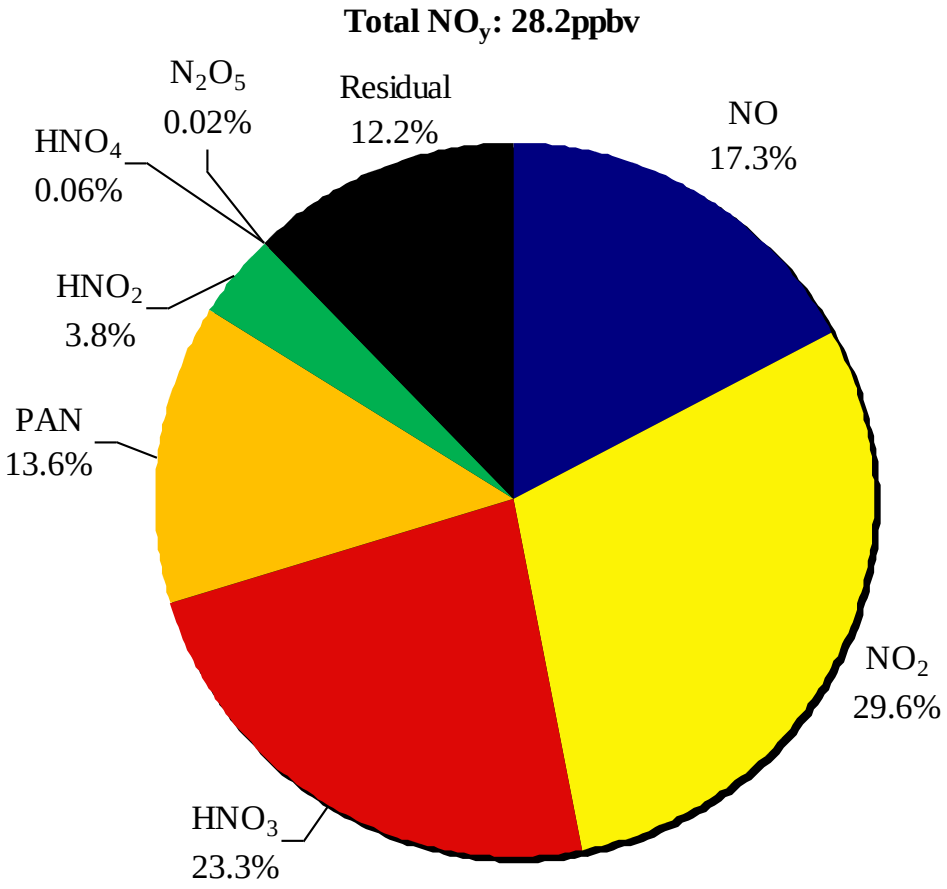

Figure 2.2 Average daytime (9:00–18:00) NO_y budget during 10–30 August 2007, in which NO, NO_y, PAN, HONO are measured and the other species (not directly measured) are from the 1–D model simulation (full aromatics). Residual denotes the difference between measured NO_y and the sum of measured and simulated NO_y components.

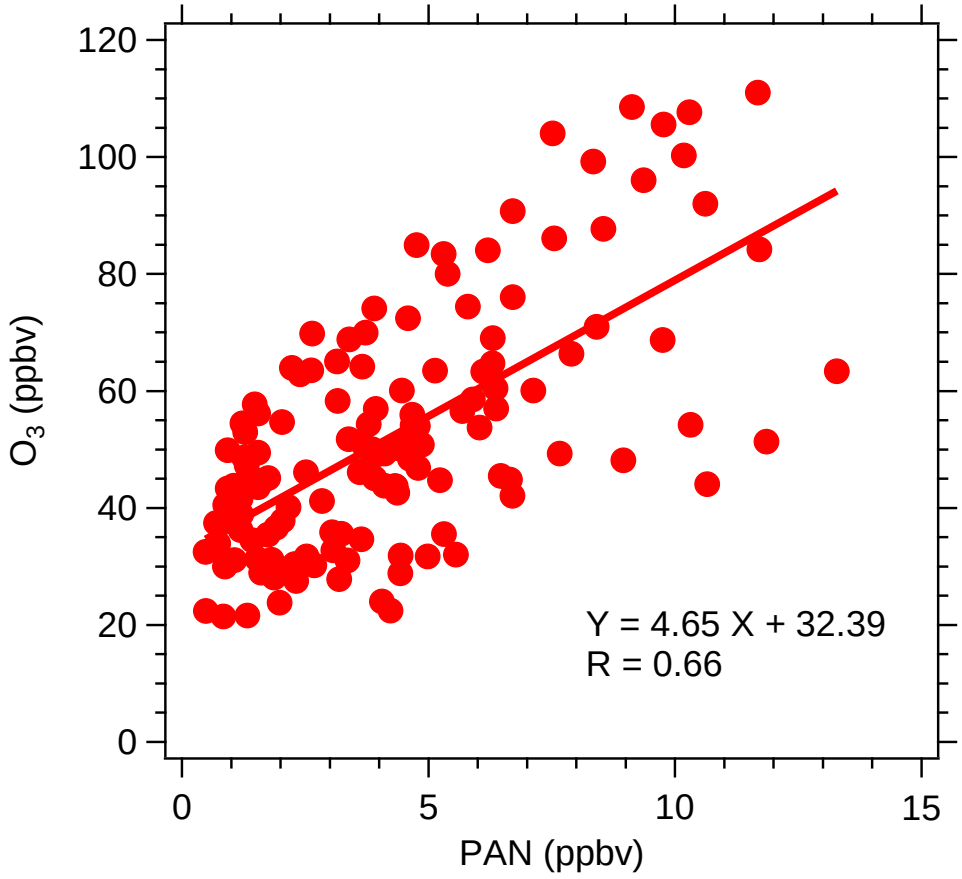

Figure 2.3 1–hour mean observed O_3 mixing ratios as a function of observed PAN for daytime (9:00–18:00) during 10–30 August 2007. Data points with O_3 larger than 20 ppbv are shown.

25% of the average 24–hour OH concentration and the majority (more than 60%) of the primary OH production rate throughout the daytime (unpublished results). The impact of HONO on PAN formation is also discussed in this paper.

The diurnal variations of PAN and O_3 tracked each other well, with their peaks at ~15:00 (Figure 2.1). Figure 2.3 shows good correlations of PAN and O_3 mixing ratios during daytime (9:00–18:00). The linear correlation between PAN and O_3 reflects that

both species are products of NO_x and peroxy radicals. Thus, understanding the chemistry of PAN formation also facilitates the investigation of O_3 formation mechanism.

2.3.3 Chemical and transport sources of PAN

The original REAM photochemical mechanism is adopted from the GEOS–Chem model [Bey et al., 2001]. Using this base version of 1–D REAM model, we found that the model significantly underestimated PAN by a factor of 4 (Figure 2.4). In this simulation, the model was constrained by observed acetaldehyde and acetone, which are major sources of PA radical, and all the observed NMHCs except for aromatics. Although methylglyoxal (MGLY) is also a major source of PA radical, there were few MGLY measurements available (August 15–20, 3–hour resolution), so we did not use measured MGLY. We noticed that the simulated MGLY (less than 0.1ppbv) concentrations are much lower than the observed values (0.9 ± 0.4 ppbv), indicating some important NMHCs as MGLY sources are missing in the model.

Inspection of the measurements of NMHCs shows that ~50% of observed NMHCs are aromatics (Figure A.1). Among fast–reacting NMHCs, toluene, xylenes, and ethyl benzene are among the group with highest mixing ratios. A major oxidation product of these aromatic species is MGLY (Table A.1 and Figure A.1 in Appendix A). In subsequent simulations we expanded the photochemical mechanism in the model with chemistry of aromatic NMHCs based on the SAPRC–07 mechanism [Carter, 2009]. The model predicted PAN values increase considerably, leading to better agreement with the measurements (Figure 2.4), but there is still on average ~25% of 24–hour average PAN

unexplained in the model (all relative changes are with respect to 24–hour mean values hereafter).

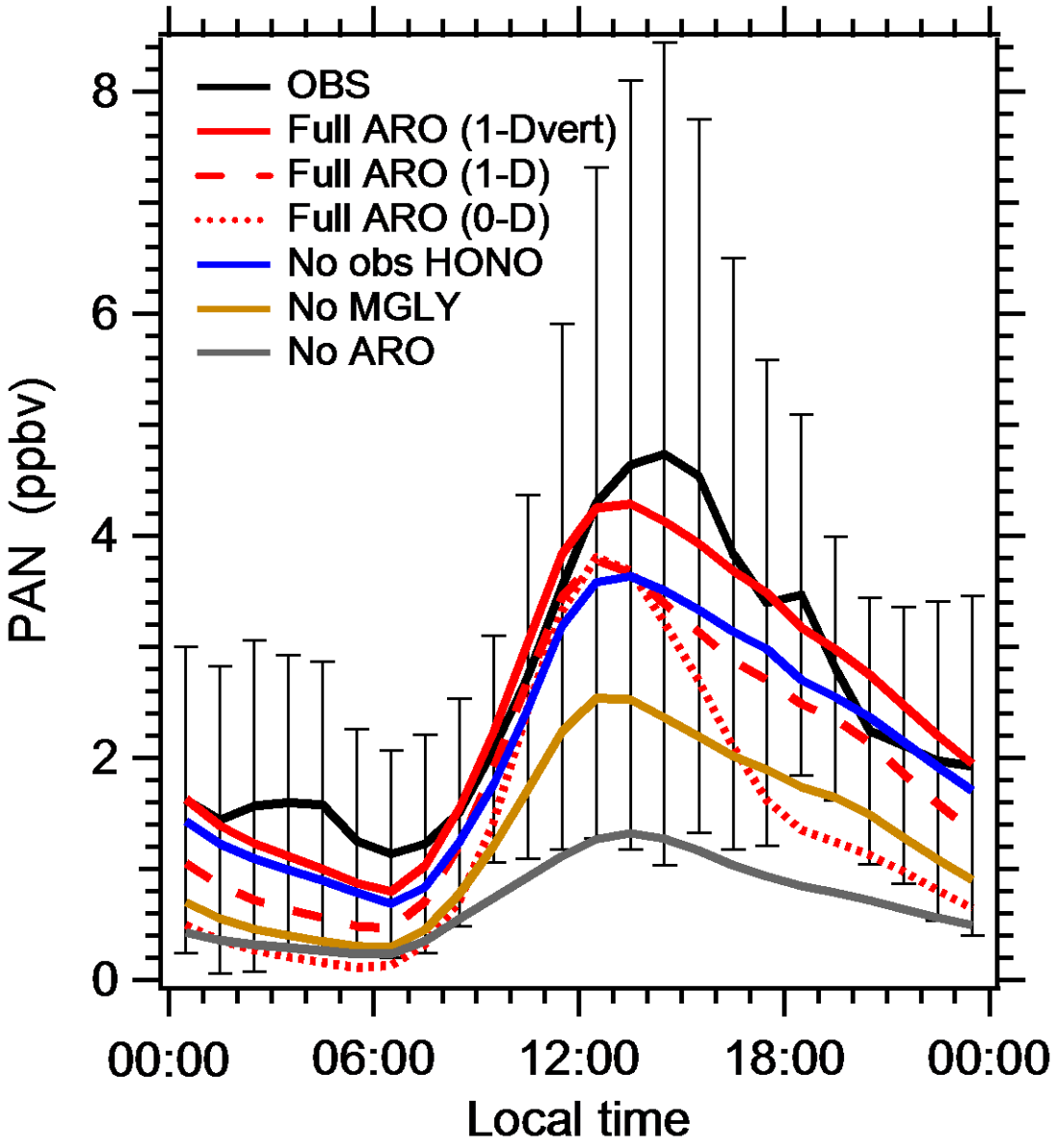

Figure 2.4 Average hourly diurnal profiles of measured PAN (black line) together with standard deviations (black bars), and model predicted PAN in different scenarios: (1) 1–D model incorporating a full aromatics–degradation mechanism (red solid line) using observed vertical profiles (36); (2) 1–D model incorporating a full aromatics–degradation mechanism (red dashed line) with only surface aromatics constrained by the

observations; (3) a box model simulation incorporating a full aromatics–degradation mechanism (red dotted line); (4) 1–D model incorporating a aromatics–degradation mechanism, which does not include the production of MGLY (brown line), using the observed aromatic VOC vertical profiles (36); (5) 1–D model without surface HONO constrained by the measurements (blue line), using the observed aromatic VOC vertical profiles (36); (6) 1–D model without aromatics (grey line). "1–Dvert" and "1–D" denote with and without observed NMHC vertical profiles, respectively.

In the two simulations mentioned above, the model is only constrained by surface observations since we did not have measurements at higher altitudes. Such a model configuration is equivalent to assuming that all the emission sources are located at the surface and the trace gases in the boundary layer are all due to transport from surface by turbulent diffusion. By comparing with previous measurements in Beijing, we found that model simulated vertical gradients of aromatics are evidently larger than the measurements in a previous study [T Mao et al., 2008]. Although those measurements were at a different site in Beijing in the fall, it points to the possibility of large underestimates of aromatic NMHCs at 100–400m in our model. One potential model bias is that WRF simulated eddy diffusion coefficients are too low, leading to overestimated vertical concentration gradient. Therefore, we conducted a sensitivity simulation by increasing the boundary layer eddy diffusion coefficients by a factor of 5, and the simulated vertical gradient of aromatics was still too large, which suggests that there are other reasons for underestimation of aromatics in the boundary layer, e.g. maybe there were some non–surface sources of aromatics around the site. Coincidentally, previous studies found that in addition to vehicle emissions and solvent evaporations, several petrochemical plants located 10–30 km from our sampling site, e.g., Yanshan Petrochemical Plants in Fangshan, Beijing Chemical plants in Chaoyang, and Eastern

Chemical Works in Tongzhou, are also major sources of aromatics at the observation site [Song et al., 2007]. It is likely that these non–surface point sources at 100–200m above the surface are responsible for the missing aromatics at 100–400m in our model.

In a third simulation, by assuming there are non–surface emissions of aromatics we further constrained our model at 20–400m according to the observed vertical profiles of aromatics [T Mao et al., 2008]. Within our expectation, the model shows further improvements of simulated PAN from the previous results. The 1–D model reasonably reproduces the observed diurnal PAN profile, accounting for ~95% of the measured values on average (Figure 2.4) as well as the day–to–day variation of PAN and most daytime peak values (R = 0.71, Figure A.2). Including profiles of other VOCs (such as alkenes) from the same study [T Mao et al., 2008] in the model simulation does not significantly affect the model results. Detailed examination of the interaction between surface and boundary layer PAN production requires more measurements than available in this study and should be targeted in a future study at the measurement site.

Comparing the results of the third simulation to the second one shows that non–surface aromatic NMHC emissions increased near–surface PAN concentrations by ~20%. This result indicates the significant impact of downward transport of PAN produced aloft in the boundary layer on the measured PAN levels near the surface. In a previous study of PAN sources at Tokyo, Kondo et al. [2008] suggested that missing downward transport of PAN from the boundary layer is a main factor leading to the underestimation of PAN in their box model [Kondo et al., 2008]. They argued that the lower temperature at higher altitudes results in longer lifetimes and facilitates the downward transport of PAN to the surface. In order to investigate the contribution from downward transport, we ran the 1–D

model as a box model by turning off the vertical transport. In this manner, the fraction of PAN produced at the surface layer and the rest transported from aloft to the surface can be isolated and compared. Figure 2.4 shows that on average this box–model only explains about half of the measured PAN near surface, thereby suggesting that downward transport of PAN from aloft contributes the rest 50%. Our results are consistent with the previous study [Kondo et al., 2008], and suggest that vertical mixing in the boundary layer is an important factor for generating elevated pollutant levels near the surface. Specifically with respect to PAN chemistry, downward transport has the direct effect of increasing PAN concentrations near the surface. Further, the decomposition of PAN transported from above provides a radical source and speeds up photochemical processing near the surface. For example, the 1–D model predicts 10% higher 24–hour average OH concentration than the 0–D model.

We conducted a fourth sensitivity simulation to investigate the impact of MGLY on PAN formation. After removing the formation of MGLY in the model, simulated PAN concentrations drop by ~50% (Figure 2.4), suggesting that half of the observed PAN concentrations are due to the production of MGLY during the oxidation of aromatics. The difference between the first (without aromatics, grey line) and the fourth (without MGLY, yellow line) simulations mainly reflects the contribution (~20%) from another PAN precursor produced from aromatics – biacetyl. We further evaluated the contributions by each aromatic species to MGLY (and further to PAN) production based on their measured concentrations, reaction rate constants with OH and MGLY molar yields (Table A.1 in Appendix A). The results show that m–xylene and 1,3,5–trimethyl benzene are the most efficient PAN precursors because of their relatively faster reaction

rates with OH and larger MGLY yields (e.g. 64% for 1,3,5–trimethyl benzene), although their concentrations are only ~20% and ~4% of the most abundant aromatic species, toluene, respectively (Table A.2 in Appendix A).

Based on the results of above four simulations, we estimate that aromatics account for ~75% of the total PAN source and MGLY from the oxidation of aromatics accounts for ~50%. Most of MGLY (more than 90%) is produced by oxidation of aromatics. Considering the uncertainties introduced by using previously measured aromatics vertical profiles [T Mao et al., 2008], the contribution of aromatics would lie in the range of 55 – 75% (by comparing PAN levels in "NO–ARO", "1–D", and "1–Dvert" simulations in Figure 2.4). The dominant role by aromatics is due to their larger proportion in the total NMHCs (~50% in Figure A.1) and faster production of PA radicals (through MGLY and biacetyl) than the other OVOCs. Contributions from the other major OVOCs are also obtained and tabulated in Table A.3 in Apendix A.

Since PAN formation chemistry is initiated by reactions between NMHCs and OH, another necessity for maintaining the measured high PAN levels is a sufficient supply of OH. As mentioned above, our model analyses suggest that HONO serves as an important OH producer in Beijing (unpublished results), but current known HONO sources can only explain a small portion (~0.1 ppbv) of the observed HONO (~1ppbv). We examined the impact from HONO on PAN formation chemistry by conducting a fifth sensitivity simulation in which we removed the observational constraint on HONO. Without fixing model HONO to the observed values, model predicted PAN concentrations drop considerably, by ~15% on average and even more in the afternoon

hours (Figure 2.4), underlining the important role of the abundant HONO (~1 ppbv) during daytime as a major OH primary source for PAN formation.

2.4 Implications

Our finding that aromatics are the dominant (55–75%) source of PAN in Beijing is consistent with a recent study suggesting that aromatics account for ~45% of the observed peroxyacetic acid [X Zhang et al., 2010]. Previous studies reported comparable or even larger abundance of aromatic NMHCs over the southern [X M Wang et al., 2002; J Zhang et al., 2007] and eastern [Ran et al., 2009] China. Specifically, toluene has been found to be the main contributor to ozone formation in southern China [X M Wang et al., 2002; J Zhang et al., 2007]. Therefore, aromatics appear to be a major PAN (and O_3) precursor over polluted East China [C Zhao et al., 2009a], in contrast to previous studies outside China indicating that alkenes and acetaldehyde are more important for PAN production [Kondo et al., 2008; Roberts et al., 2001]. However, aromatics are often ignored in global [Bey et al., 2001; Emmerson and Evans, 2009] and (to a lesser degree) regional 3–D photochemical transport models [Y Wang et al., 2008]; their emissions [Q Zhang et al., 2009] over China, as well as photochemistry [Bloss et al., 2005], are still quite uncertain. Ongoing modeling analysis (unpublished) reveals that regional anthropogenic emissions of aromatics are significantly underestimated over China. Our findings suggest that critical assessments of aromatics emissions and chemistry (such as the yields of MGLY) are necessary to understand and assess ozone photochemistry and export in China.

In addition, the comparison between a 1–D and box model simulation suggests that 1–D models may be more suitable than box models in analyzing in situ measurements of species such PAN, the lifetime of which changes drastically in the boundary layer. Downward transport of PAN from the boundary layer affects not only surface concentrations but also surface chemical reactivity by providing a source of radicals through decomposition. At polluted urban sites like Beijing, there is also evidence that non–surface VOC and other precursor sources appear to be an important factor for surface concentrations of PAN via boundary layer–surface exchange.

3. [2]SUMMERTIME PHOTOCHEMISTRY DURING CAREBEIJING-2007: RO_X BUDGETS AND O_3 FORMATION

3.1 Background and motivation

Photochemical smog was first documented in 1950s in Los Angeles [Haagen-Smit and Fox, 1954], and is nowadays a prevalent air pollution phenomenon around the world [Molina and Molina, 2004]. A major contributor to smog is the production of secondary pollutants such as O_3 and aerosols from photochemical reactions involving NO_x ($NO_x \equiv NO + NO_2$) and volatile organic compounds (VOCs), which are emitted from various anthropogenic and natural sources. Over the past decades, continuously improving knowledge of photochemical pollution has successfully served as the basis for formulating the pollution control strategies over the United States [NRC, 1991; NARSTO, 2000]. Uncertainties of photochemical modeling in some regions remain large due to the lack of accurate emission inventories [NARSTO, 2005] and incomplete knowledge of chemistry [Volkamer et al., 2010].

A region of concern is China. The rapid increasing emissions of NO_x and VOCs over China since 1980s driven by economic growth have been observed by satellites [Richter et al., 2005] and documented in bottom-up inventories [Q Zhang et al., 2009]. As an expected consequence, elevated O_3 [T Wang et al., 2006] and peroxy acetyl nitrates (PANs) [Z Liu et al., 2010] accompanied by high loadings of aerosols [Chan and Yao, 2008; Y H Zhang et al., 2008] have been observed in the country. Severe O_3 and

[2] This chapter is an extension of "Summertime urban photochemistry during CAREBeijing-2007: ROx radical budgets and O3 formation," published on Atmospheric Chemistry and Physics Discussions in 2012 (Atmos. Chem. Phys. Discuss., 12, 4679-4717). Co-authors are Y. Wang, D. Gu, C. Zhao, L. G. Huey, R. Stickel, J. Liao, M. Shao, T. Zhu, L. Zeng, A. Amoroso, F. Costabile, Chih-Chung Chang, and Shaw-Chen Liu.

aerosol pollution on an unprecedented large regional scale [van Donkelaar et al., 2010; C Zhao et al., 2009a] have also drawn attention given the large impacts on public health.

Furthermore, some recent observations over China demonstrated the complexity of photochemistry that cannot be fully explained by current knowledge. For example, surprisingly high daytime HONO concentrations from unknown sources have been observed in Beijing [An et al., 2009] and the Pearl River Delta (PRD) region [Su et al., 2008]. At a suburban site over PRD, the current standard photochemistry could not explain the observed level of OH, the key oxidant in the troposphere [Hofzumahaus et al., 2009; Lu et al., 2012]. Due to high loading of aerosols, heterogeneous chemistry appears to be important in the radical budget [Kanaya et al., 2009] and reactive nitrogen processing [Pathak et al., 2009]. A case in point is that we still do not have a clear understanding of how the large emission reductions affected secondary pollutants during the 2008 summer Beijing Olympic and Paralympic Games. Chemical transport modeling study by Yang et al. [2011] demonstrated the highly variable chemical sensitivities of O_3 to its precursor emissions due to the uncertainties in the emissions of aromatic VOCs. However, the sensitivity relationships are very difficult to derive from the observations. For example, T Wang et al. [2010] found increases of O_3, sulfate and nitrate while NO_x and VOCs decreased at an urban site in Beijing in the first two weeks after emission control for the Olympics Game. Similar finding was reported at another urban site in Beijing [Chou et al., 2011]. These findings reflect the fact that the effects on O_3 from precursor emission changes can be masked by the variations in the spatial pollutant distribution and meteorological conditions for dispersion, transport, and chemical photolysis.

Given the difficulty of interpreting empirical evidence, another approach is through in-depth observation-based chemical budget analyses to gain insight into the chemical system. In this work, we analyze the O_3 photochemical processes in Beijing in August 2007 during the CAREBeijing (Campaigns of Air quality REsearch in Beijing) Experiment employing the 1-D version of the Regional chEmical and trAnsport Model (REAM-1D) constrained by observed chemical species and physical parameters, including O_3, NO, PAN, HONO, VOCs, and aerosol surface areas. The goal is to gain a detailed understanding of the budgets of RO_x (OH + HO_2 + organic peroxy radicals (RO_2)) radicals and formation processes of O_3 and to understand the implications on emission control strategies in Beijing and other polluted regions in China.

The remainder of this chapter proceeds as follows. In Section 3.2, we describe the measurement methods and the REAM-1D model. Section 3.3 presents the modeling analysis results. We examine the budgets of RO_x radicals in Section 3.3.1, which will form the basis for analyzing production and loss rates of O_3 in Section 3.3.2. We then analyze the specific roles of aromatics, HONO, and aerosol uptake of HO_2 in the budgets of radicals and O_3, respectively, in Section 3.3.3. We investigate the sensitivities of O_3 production to NO_x and VOCs in Section 3.3.4. In Section 3.4, we summarize our findings and discuss the implications for O_3 control strategies over China.

3.2 Methods

3.2.1 Measurement methods

During the CAREBeijing-2007 experiment [Zhu et al., 2009], a full suite of trace gases were measured concurrently in August 2007 at an urban site located on a building roof top (~20 m above the ground level) on the campus of Peking University (39.99 ℃N,

116.31 ℃E). Nitrogen monoxide (NO) was measured with a custom–made chemiluminescence detector [Ryerson et al., 2000]. Total reactive nitrogen compounds (NO_y, only gas phase) were measured by the conversion of the NO_y species to NO on a molybdenum converter operated at 300 ℃. PAN was measured using a chemical ionization mass spectrometer (CIMS) [Slusher et al., 2004]. HONO was measured with a liquid coil scrubbing/UV–VIS instrument [Amoroso et al., 2006]. O_3 and CO were measured by commercial instruments from the ECOTECH (EC9810 and EC9830). C_3–C_9 NMHCs were measured with a time resolution of 30 minutes using two online GC–FID/PID systems (Syntech Spectra GC–FID/PID GC955 series 600/800 VOC analyzer), one for the C_3–C_5 NMHCs, and the other for C_6–C_9 NMHCs [Shao et al., 2009]. Another automated GC/MS/FID system was deployed to measure NMHCs in daytime (8:00–9:00 and 13:00–14:00) [Hofzumahaus et al., 2009]. OVOCs were measured using the PFPH–GC/MS method [Ho and Yu, 2004].

3.2.2 The REAM-1D model setup

The 3-D version of the Regional chEmical and trAnsport Model (REAM-3D) has been applied in a number of studies on O_3 photochemistry and transport at north mid-latitudes [Choi et al., 2005; Wang et al., 2007; Choi et al., 2008a; Choi et al., 2008b; Zhao et al., 2009ab; Zhao and Wang, 2009; Zhao et al., 2010; Yang et al., 2011]. The REAM-1D model shares the modules for O_3-NO_x-hydrocarbon photochemistry, vertical diffusion, convective transport, and wet/dry deposition [Liu et al., 2010] with the REAM-3D model. The chemical kinetics data were updated with the latest compilation by Sander et al. [2011], and the VOC chemistry in REAM-3D is expanded to include the chemistry of aromatics based on the SAPRC-07 chemical mechanism [Carter, 2009]. Vertical

transport is driven by WRF assimilated meteorological fields based on the NCEP reanalysis data [Zhao et al., 2009a].

The model is constrained with measured CO, O_3, NO, HONO, NMHCs (C_2–C_9), OVOCs (acetone, acetaldehyde and formaldehyde) and aerosol surface areas and was run with a 1–minute time step from 1 August to 30 August 2007. The results for the last 20 days were analyzed after a spin-up time of 10 days. The REAM-1D model has been shown to be able to reproduce the observed PAN in Beijing, which is sensitive to the VOC oxidation mechanism and transport within the boundary layer [Liu et al., 2010]. Our model simulated OVOCs, including formaldehyde, acetaldehyde, and acetone, agree with the observations within 20% in terms of diurnal average concentrations, indicating that secondary production is the predominant source. Additional detailed descriptions of the REAM-1D model including VOC input and model error estimates are available in the supplement.

Exceptionally high level of HONO was observed at daytime (~1ppbv in the afternoon) during the study period. The gas-phase source from the NO+OH reaction alone could only explain a small portion (~10%) of the observed HONO concentrations. We therefore introduced a pseudo-reaction of $NO_2 \rightarrow$ HONO in the model in order to reproduce the observed daytime HONO and quantitatively estimate the primary radical source from the heterogeneous HONO production pathway. Due to the large aerosol surface areas (~1000 $\mu m^{-2} cm^{-3}$), the uptake of HO_2 by aerosols may become a large HO_2 sink. The HO_2 aerosol sticking coefficient, γ, is still quite uncertain and may be a function of temperature and aerosol composition

Table 3.1 Sensitivity simulation scenarios

Scenarios or purposes	Description
S0	Standard setup: with full VOC chemistry, excess HONO, $\gamma(HO2) =$ 0.02
S0a	S0 with $\gamma(HO_2) = 0$
S0b	S0 with $\gamma(HO_2) = 0.2$
S1	S0 without excess HONO
S2	S0 without aromatics
S3	S0 without excess HONO or aromatics
S3a	S3 with $\gamma(HO_2) = 0$
$P(O_3)_{senst}$	S0, S0b, S1, S2, S3, S3a constrained with 50%, 70%, 90%, 110% of observed values of NO, VOCs respectively, and both of them
$\gamma(HO_2)_{senst}$	S0 with $\gamma(HO_2) = 0$, 0.02, 0.05, 0.1, 0.15, 0.2

[Kanaya et al., 2009; J Mao et al., 2010; J Thornton and Abbatt, 2005; J A Thornton et al., 2008]. In this work, we use a $\gamma(HO_2) = 0.02$ in the standard model (S0 in Table 3.1) based on model performance in simulating PAN, and we evaluate model sensitivities by varying the value of $\gamma(HO_2)$ from 0 to 0.2 (Section 3.3.3).

We conducted a number of model simulations, summarized in Table 3.1, to understand the sensitivities of radical budgets and O_3 production to aerosol uptake of HO_2, high daytime HONO concentrations, and NO_x and VOCs. S0 is the standard model; S0a and S0b are S0 with varied $\gamma(HO_2)$ values, 0 in S0a and 0.2 in S0b, respectively. S1 is S0 without the "excess" HONO that cannot be explained by gas-phase HONO production; S2 is S0 without aromatics; S3 is S0 without excess HONO or aromatics, and S3a further removes the aerosol HO_2 uptake ($\gamma(HO_2) = 0$) in S3. The $P(O_3)_{senst}$ simulations compare O_3 production rates under varied NO_x and VOCs conditions. The $\gamma(HO_2)_{senst}$ simulations examine the sensitivities of O_3 production to different $\gamma(HO_2)$ values ranging from 0 to 0.2. In the sensitivity simulations, we did not constrain OVOCs to the observations in order to retain the feedback from OVOCs. Removing the constraint of observed OVOCs in the standard model did not lead to notable changes in RO_x concentrations or O_3 production/loss rates.

3.3 Results and discussions

The chemical dependence of O_3 formation on the emissions of its precursors, including NO_x and VOCs, is driven by the cycling of a variety of RO_x radicals. In this work, with the 1-D model constrained by observations of O_3 and its precursors, we first examine the abundances and budgets of RO_x radicals, and characterize the main features and uncertainties of chemistry in Beijing. Then, by focusing on the chemical pathways

controlling the O_3 formation, we quantitatively examine the O_3 production and loss processes and their responses to varied precursor changes, in order to understand the chemical regime of O_3 formation and its implications on O_3 control strategies.

3.3.1 Budgets of RO_x radicals

Model simulated concentrations of OH, HO_2 and RO_2

Figure 3.1 shows the average diurnal profiles of OH, HO_2 and RO_2 concentrations simulated in the standard model (S0). The 20-day average diurnal maximum concentrations of OH, HO_2, and RO_2 are 9×10^6, 6.8×10^8, and 4.5×10^8 molecules cm^{-3}, respectively. RO_x radical measurements over mainland China are still sparse. The maximum OH concentration (9×10^6 molecules cm^{-3}) simulated in this study for Beijing is ~50% higher than that simulated over Mountain Tai in June of 2006 (6×10^6 molecules cm^{-3}) [Kanaya et al., 2009], and lies between the observed (13×10^6 molecules cm^{-3}) and simulated (7×10^6 molecules cm^{-3}) values at a site in PRD [Hofzumahaus et al., 2009]. The maximum HO_2 concentration simulated for Beijing (6.8×10^8 molecules cm^{-3}) is close to that over Mountain Tai [Kanaya et al., 2009], and is only half of that in PRD [Hofzumahaus et al., 2009]. We note that the model simulated HO_2 concentrations over China are quite sensitive to $\gamma(HO_2)$, due to the large abundance of aerosols. Removing the aerosol HO_2 sink in this study would lead to higher simulated HO_2 and OH concentrations in good agreement with the observed values at the PRD site by Hofzumahaus et al. [2009], although the locations and time of the two studies are different. Compared to urban areas outside China, the simulated OH and HO_2 concentrations for Beijing are similar to those observed in Mexico City [Dusanter et al.,

2009; Shirley et al., 2006], and yet higher than those in New York City [Ren et al., 2003] and Birmingham of the UK [Emmerson et al., 2005b].

RO_2 radicals include all organic peroxy radicals derived from VOC oxidation, and they are categorized into 7 groups (Figure 3.1), i.e. methyl peroxy radicals (CH_3O_2), first generation peroxy radicals from alkanes ($ALKA_p$), alkenes except isoprene ($ALKE_p$), isoprene (ISO_p), aromatics (ARO_p), acyl peroxy radicals (RCO_3), and peroxy radicals from OVOCs ($OVOC_p$). The most abundant 3 groups of RO_2 are CH_3O_2, AROp and RCO_3. The largest contribution of CH_3O_2 is expected. Aromatics have higher concentrations and reactivities than alkenes and alkanes [Liu et al., 2010], producing more RO_2 radicals upon oxidation. $RC(O)O_2$ radicals are produced from OH oxidation or photolysis of a variety of carbonyl compounds. $CH_3C(O)O_2$ is the simplest and most abundant $RC(O)O_2$, and also the precursor of PAN. Liu et al. (2010) showed that methylglyoxal from aromatics is the predominant source (~75%) of $CH_3C(O)O_2$ and PAN in Beijing.

<u>RO_x budgets</u>

Figure 3.2 illustrates schematically the RO_x daytime (6:00 – 18:00) budgets simulated in the model. The fast RO_x cycling is driven by NO_x catelyzed VOC oxidation, which is typical in NO-rich environments [Dusanter et al., 2009; Elshorbany et al., 2009a; Emmerson et al., 2005a; Shirley et al., 2006]. NO + HO_2 (19.8 ppbv h^{-1}) and NO + RO_2 (12.2 ppbv h^{-1}) are the two largest pathways of radical cycling in the system, mainly due to the abundance of NO (e.g. ~ 5ppbv around noontime).

It is more constructive to examine the primary sources and sinks of RO_x radicals in this relatively complex system to understand the controlling factors.

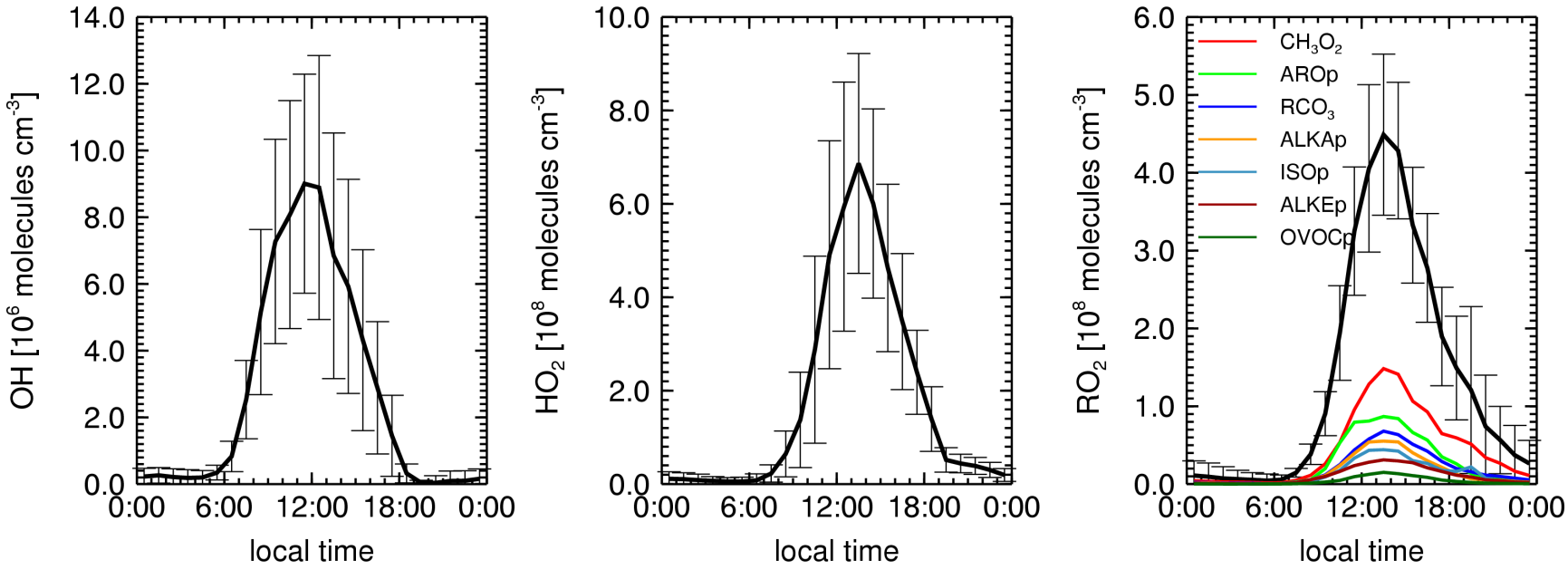

Figure 3.1 Average diurnal profiles of OH, HO_2 and RO_2 (black lines) in the standard model (S0). The vertical bars show the hourly standard deviations. The color lines in the right panel show the major components of RO_2, which are described in the text.

Photolysis of OVOCs turns out to be the predominant primary RO_x source (4.0 ppbv h^{-1}), and is also the largest sources of HO_2 (2.4 ppbv h^{-1}) and RO_2 (1.6 ppbv h^{-1}), consistent with previous urban studies [Jenkin and Clemitshaw, 2000; Emmerson et al., 2005b; Dusanter et al., 2009]. Photolysis of excess HONO is the second largest RO_x source (3.0 - 0.8 = 2.2 (ppbv h^{-1})), as well as the largest source of OH. At noontime the excess HONO produces OH at ~5 ppbv h^{-1} (Figure 3.3), a rate that is comparable to that found by Su et al. [2008] at Xinken in PRD, and slightly higher than that at another site, Backgarden, in the same region [Hofzumahaus et al. 2009]. However, the excess daytime HONO source strength found in China is significantly larger than most urban areas outside China [e.g. Acker et al., 2006; Kleffmann, 2007 and references therein; Dusanter et al., 2009; Elshorbany et al., 2009; Costabile et al., 2010]. The reasons for such a uniquely large HONO source in China are still unknown. The $O^1D + H_2O$ reaction only contributes 0.4 ppbv h^{-1} of primary OH production. Summing up all these aforementioned sources gives a total primary RO_x production rate at 6.6 ppbv h^{-1} (2.6 ppbv h^{-1} for OH, 2.4 ppbv h^{-1} for HO_2, and 1.6 ppbv h^{-1} for RO_2), which is comparable to that in Santiago of Chile (7.0 ppbv h^{-1}) [Elshorbany et al., 2009], but ~50% higher than those in Mexico City in 2006 (4.75 ppbv h^{-1}) [Dusanter et al., 2009], and Birmingham of the UK (4.5 ppbv h^{-1}) [Emmerson et al., 2005b].

RO_x radicals are removed ultimately from the atmosphere via deposition of radical reservoir species, e.g. HNO_3, H_2O_2, ROOH. The net radical losses via NO_x-radical reactions are 3.6 ppbv h^{-1}, including NO_2 + OH producing HNO_3 (1.7 ppbv h^{-1}), RO_2 + NO_2 reaction producing organic peroxy nitrates (RO_2NO_2, mostly PANs) (1.1 ppbv $^{-1}$), and RO_2 + NO reaction producing organic nitrates ($RONO_2$) (0.8 ppbv h^{-1}). By contrast,

the radical loss rates via radical-radical reactions producing peroxides such as H_2O_2 and ROOH are much lower (0.6 ppbv h^{-1} in total). Such a contrast has been typically seen as a feature of chemistry in NO_x-rich urban environments. Another important and yet uncertain RO_x sink in Figures 3.2 and 3.3 is the aerosol uptake of HO_2 (1.1ppbv h^{-1}), mainly owing to abundant aerosols in Beijing. The magnitude of this radical sink varies significantly with values of $\gamma(HO_2)$ used in the model (Section 3.3.3).

It is also noteworthy that the two RO_2 + NO_x reaction pathways collectively contribute a net RO_x loss at 1.9 ppbv h^{-1}, larger than that of NO_2+OH (1.6 ppbv h^{-1}), which is different from most urban environments outside China [Emmerson et al., 2005b; Dusanter et al., 2009; Elshorbany et al., 2009]. Figure 3.4 shows the diurnal transition of RO_2NO_2 production and loss. During most of the daytime, RO_2NO_2 production dominates over its loss processes (mainly via thermal decomposition) leading to the net formation of RO_2NO_2 and thus sequestering of NO_2 and $R(O)O_2$ radicals. RO_2NO_2 loss starts to dominate over production from the late afternoon into the evening. Such a diurnal transition of RO_2NO_2 production and loss differs from the often used steady-state assumption of RO_2NO_2, and has significant impacts on O_3 production (Section 3.3.2). $RONO_2$ is formed from minor channels in NO + RO_2 reactions, and the importance of this channel is known to be a function of the size of RO_2. $RONO_2$ has longer lifetimes (at least 2 days) than RO_2NO_2, and its loss by transport and deposition is a net loss of RO_x radicals.

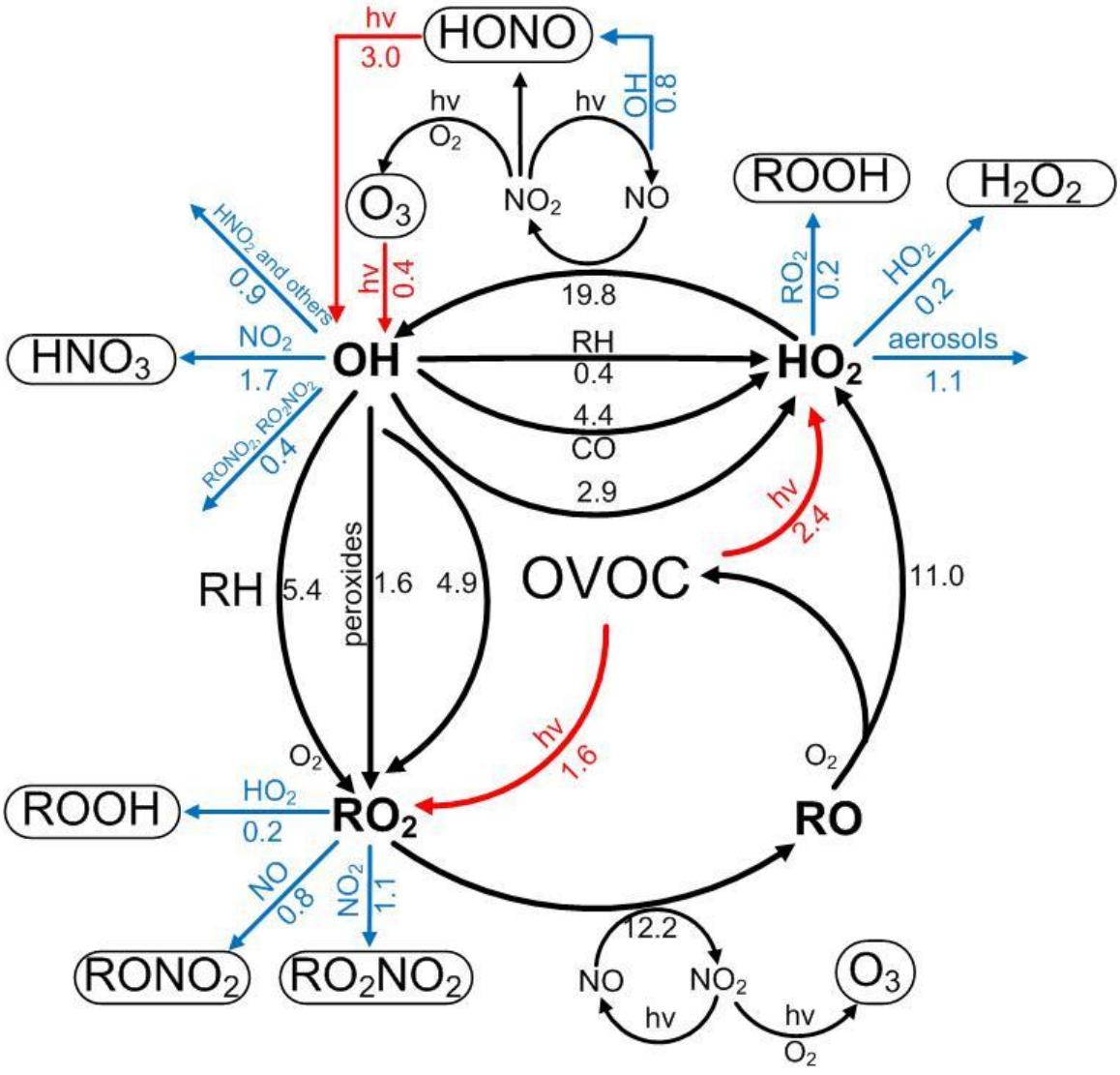

Figure 3.2 Daytime (6:00 - 18:00) average budgets of RO_x radicals. Primary RO_x sources and sinks are in red and blue, respectively. The production and loss rates are in ppbv h^{-1}.

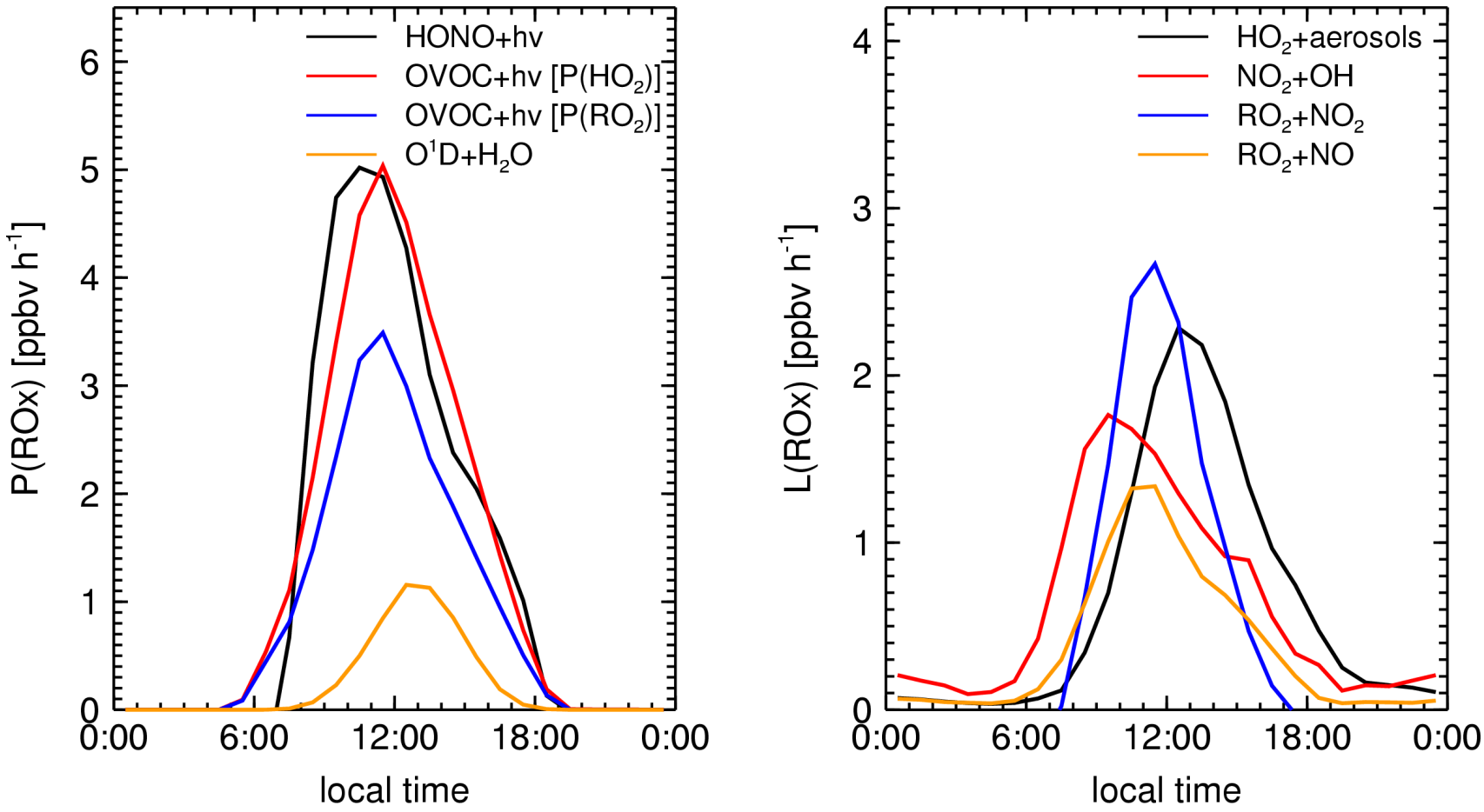

Figure 3.3 Average diurnal profiles of major RO_x primary sources and sinks.

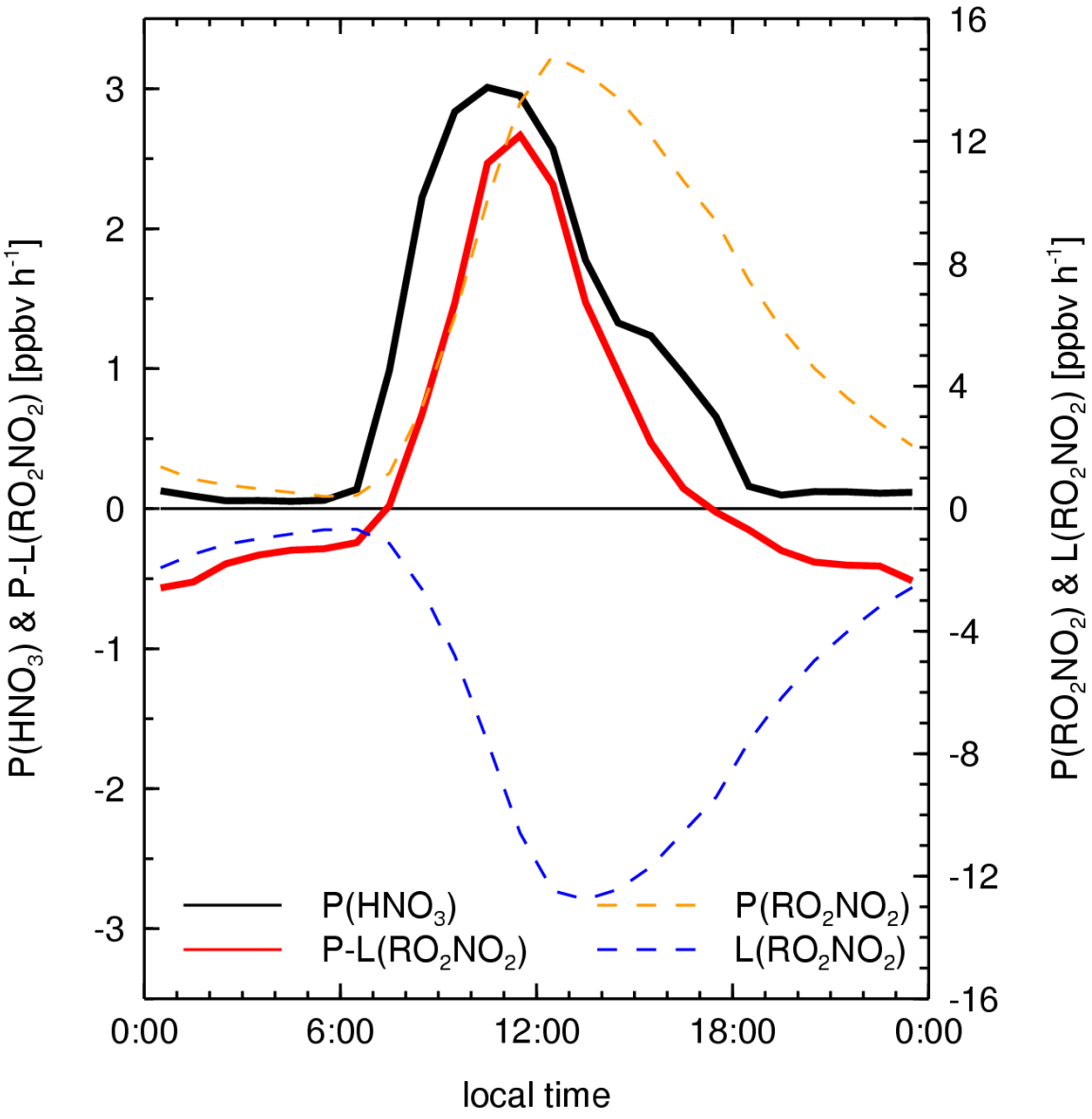

Figure 3.4 Average diurnal profiles of net formation rates of PANs and HNO_3. Production and loss rates of PANs are also shown.

Another feature in the chemical system in Figure 3.2 is the coupling of NO_x and VOCs chemistry. Both are involved in major RO_x primary sources, i.e. $NO_2 \rightarrow HONO \rightarrow OH$ (2.2 ppbv h^{-1}) and photolysis of OVOCs (4.2 ppbv h^{-1}). Meanwhile, some of the RO_x sinks, i.e. RO_2 + NO/NO_2 also depend on both NO_x and VOCs, rather

than only one of them. These aspects of chemistry have implications for O_3 sensitivities to NO_x and VOCs. In Section 3.3.2 – 3.3.3, we examine the formation of O_3, and its sensitivities to various factors, including excess HONO, aromatics, $\gamma(HO_2)$, as well as NO_x and VOCs.

3.3.2 O_3 photochemistry

O_3 production and loss rates

The formation of O_3 in the troposphere is via the reactions of NO and peroxy radicals. On the other hand, due to the fast cycling of O_3 and NO_2 under urban conditions, O_3 loss is due to a number of reactions leading to the destruction of O_3 and NO_2. The daytime average $P(O_3)$ as the sum of HO_2+NO (19.8 ppbv h^{-1}) and RO_2 +NO (12.2 ppbv h^{-1}) is 32 ppbv h^{-1}(Figure 3.2), comparable to previous calculations for Beijing [Lu et al., 2011], and is near the top of reported values for urban environments [e.g. Ren et al., 2003; Shirley et al., 2006; Kanaya et al., 2008; Wood et al., 2009]. The reaction of HO_2+NO accounts for roughly 2/3 of $P(O_3)$. RCO_3 + NO, CH_3O_2 + NO and AROp + NO are the predominant RO_2 + NO reactions, due to the relative abundance of RO_2 radicals (Figure 3.1) and the larger reaction rate constant of RCO_3 + NO. The mean daytime peak of $P(O_3)$ is ~60 ppbv h^{-1}, occurring around 11:00 (Figure 3.5), earlier than the peaks of both HO_2 and RO_2 around 13:00 because of the decrease NO concentrations from morning to early afternoon. $P(O_3)$ is also found to peak around 10:00 – 11:00 local time in Mexico City [Shirley et al., 2006].

The daytime mean and maximum $L(O_3)$ rates are 6.2 ppbv h^{-1} and 12 ppbv h^{-1}, respectively, roughly 1/5 of $P(O_3)$. $L(O_3)$ consists of NO_2 → HONO (2.2 ppbv h^{-1}), NO_2 + OH (1.7 ppbv h^{-1}), RO_2 + NO_2 (1.1 ppbv h^{-1}), O^1D + H_2O (0.4 ppbv h^{-1}), and other

minor reactions. Given the noontime O_3 and NO_2 concentrations (~55ppbv and ~10 ppbv) and the loss rate of O_3, the chemical lifetime of O_3 is ~5 hours. It is interesting that the unknown source of HONO from NO_2 also serves as a $L(O_3)$ term, and is in fact the most important $L(O_3)$ reaction (~40%), directly affecting O_3 formation and the lifetime of O_3. The average daytime net formation rate of O_3, i.e. $P(O_3) – L(O_3)$, is ~26 ppbv h^{-1}.

O_3 production efficiency

Alongside O_3 formation, NO_x is transformed into oxidized nitrogen compounds NO_z ($NO_z \equiv NO_y - NO_x$), e.g. $RONO_2$, RO_2NO_2, and HNO_3, and then eventually removed from the atmosphere by deposition. NO_z compounds at daytime account for 20 - 50% of total NO_y (Figure 3.6). The O_3 production efficiency (OPE) of NO_x is defined as the amount of O_3 produced during the lifetime of NO_x [S C Liu et al., 1987]. Based on our model calculated $P(O_3)$ and $P(NO_z)$ (Figure 3.2), we estimate a daytime average OPE to be 9.7, which is much larger than that estimated by Wang et al. [2010] for the summer of 2008, and yet within the estimates by Chou et al. [2011] for the summer of 2006. It is also within the estimated range for Mexico City (4–12) [Lei et al., 2007; Wood et al., 2009]. Considering the moderate concentrations of HO_2 and RO_2 compared to other urban environments, the relatively high OPE from our calculation is mainly due to the high daytime NO concentration (~5 ppbv at noontime).

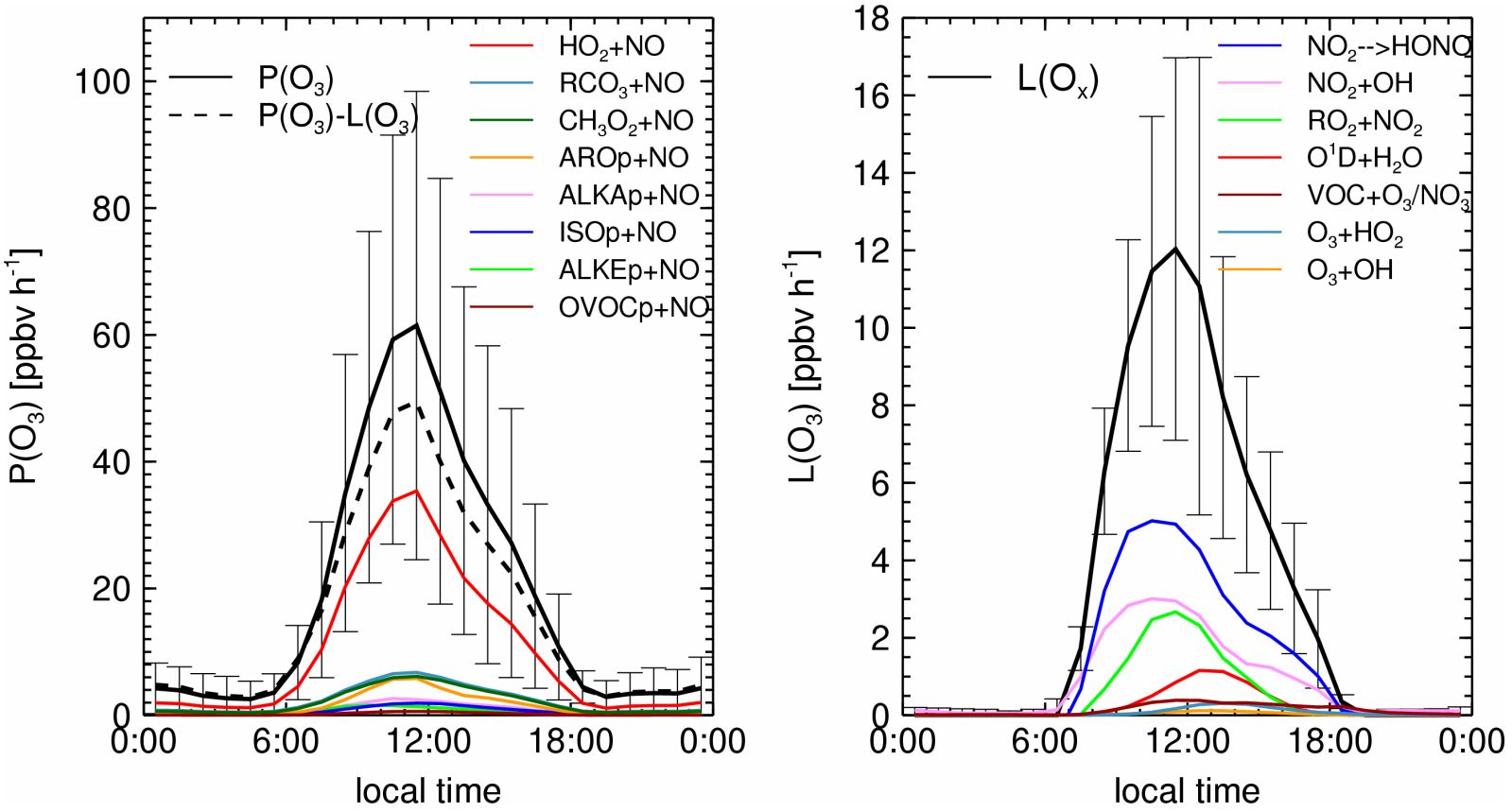

Figure 3.5 Average diurnal profiles and breakdowns of O_3 production (left) and loss rates (ppbv h^{-1}) (right). The vertical bars show the standard deviation.

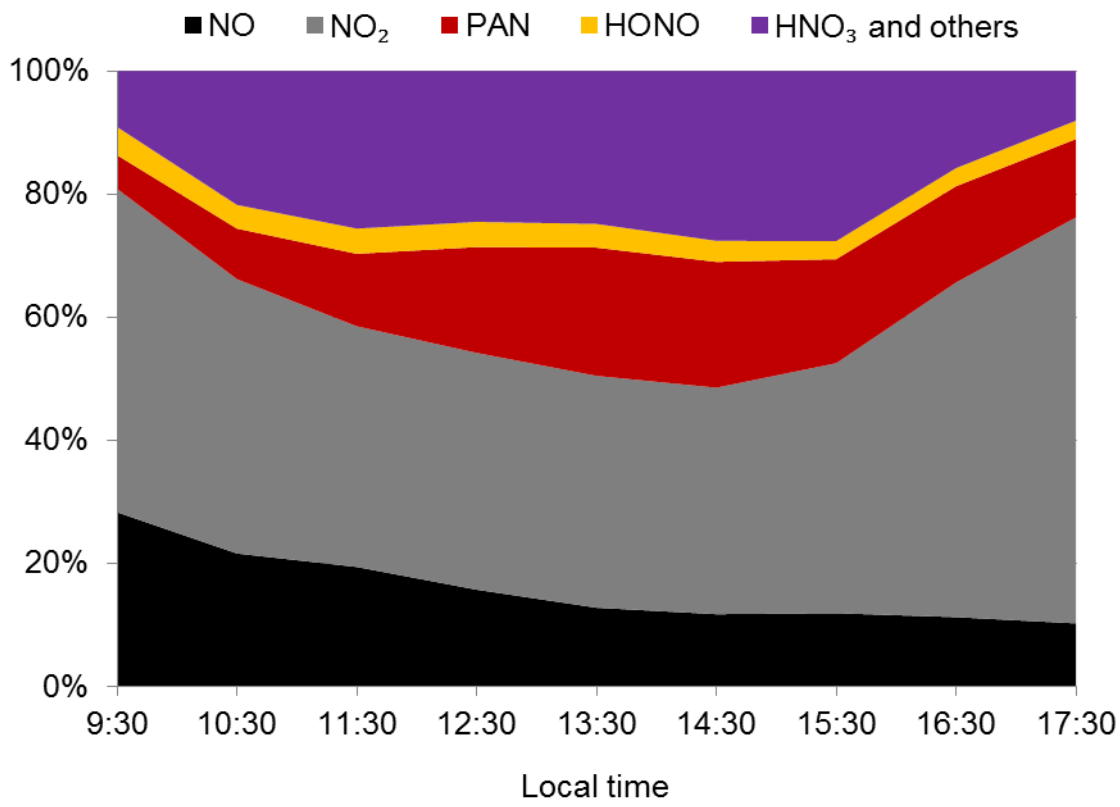

Figure 3.6 Daytime evolution of NO_y components.

3.3.3 Sensitivity studies

Based on the results from standard model (S0) results discussed above, we found that excess HONO, reactive aromatic VOCs, and aerosol uptake of HO_2 are important factors in the photochemical system in Beijing. In next section, we extend our analyses of these individual factors by comparing results from a series of sensitivity simulations listed in Table 3.1.

Impacts of excess HONO on RO_x budgets and O_3 formation

The large net OH source from the photolysis of excess HONO relative to the other primary OH sources has been shown in Figure 3.2. Figure 3.7 shows the sensitivity simulation results without excess HONO (S1). The standard model (S0) has ~60% higher daytime average OH concentration than S1 due to the excess HONO. Increased OH leads to more active photochemistry and thus ~50% increases of HO_2 and RO_2 concentrations, as well as $P(O_3)$. A second consequence is the large sink (~40%) of O_3 due to excess HONO production (Section 3.2). The impact of excessive HONO is even larger (~130%) when aromatics are not included (comparing S3 to S2 in Figure 3.7). This excess HONO term is usually not considered in the budget of O_3 in previous studies. For locations like Beijing, it appears necessary to take into account the production and loss of O_3 due to excess HONO. More importantly, the nature of excess HONO is currently unknown and needs to be considered as a major source of uncertainty for understanding O_3. We note that the daytime HONO concentrations measured in this and other studies over China [e.g. Su et al., 2008], i.e. roughly 1 ppbv on average during daytime, are substantially higher than studies elsewhere. Therefore, our finding of the important role of excess HONO should suffer much less from the instrument uncertainties than studies outside

China. The large abundance of HONO actually makes polluted regions over China a uniquely ideal place for quantitative studying HONO sources and chemistry.

Direct and secondary impacts from aromatics

Aromatics are the most reactive and abundant VOC group measured in Beijing [Liu et al., 2010]. The direct impact of aromatics on radical budgets and O_3 formation is via contributing first generation RO_2 (AROp) upon oxidation by OH; and we refer the effect due to subsequent oxidation products as secondary. Comparing the results of S0 to S2 (Figure 3.7), adding aromatics leads to a factor of 2 increase of HO_2, RO_2, and $P(O_3)$. These changes obviously could not be explained solely by the addition of AROp radicals (Figure 3.5). Careful inspection of the model results shows that OVOCs concentrations increase drastically (by 50% - 80%) after adding aromatics, and their photolysis further produces substantial amounts of primary RO_2 and HO_2. More significantly, the presence of aromatics in S0 increases OH by ~30% compared to S2 despite of the loss of OH by reacting with aromatics. Therefore, the overall increase of primary RO_x production from the secondary impact by aromatics is large enough to compensate for the shift from OH to peroxy radicals in the RO_x family. If the reactions of excess HONO are not included, the impacts by aromatics (from S3 to S1) are even more drastic, leading to more than 100% increase of HO_2, RO_2 and $P(O_3)$, and 50% increase of OH. We note that the finding on the significance of aromatics VOCs on photochemistry is qualitatively robust. However, the quantitative results presented here depend on the chemical mechanism used for aromatic VOC oxidation, for example, the yields of dicarbonyls, which are uncertain [e.g. Carter, 2009]. In situ measurements of OVOC species, especially those dicarbonyls, such as methylglyoxal and glyoxal, will be needed to further constrain the model.

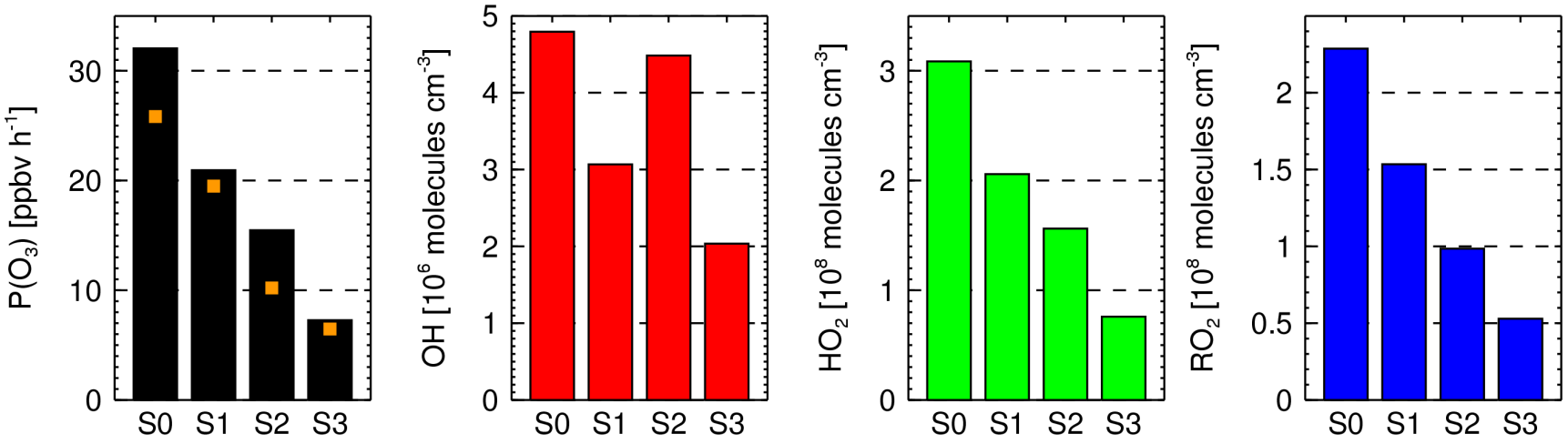

Figure 3.7 Daytime average O_3 production rates and concentrations of OH, HO_2, and RO_2 under scenarios S0, S1, S2, and S3. The yellow squares show the net O_3 formation rates ($P(O_3) – L(O_3)$).

Aerosol uptake of HO_2

Figure 3.8 shows the variations of daytime average HO_2, OH concentrations and $P(O_3)$ rates as a function of $\gamma(HO_2)$ value. HO_2 concentration drops by about ~60% from 4.05×10^8 molecules cm^{-3} at $\gamma(HO_2) = 0$ to 1.65×10^8 molecules cm^{-3} at $\gamma(HO_2) = 0.2$. Correspondingly, $P(O_3)$ decreases by ~50% from 35.4 ppbv h^{-1} to 23.3 ppbv h^{-1}, and OH drops by 30% from 5.26×10^6 molecules cm^{-3} to 3.65×10^6 molecules cm^{-3}. $P(O_3)$ and OH changes are not as large as HO_2 in part because the impact of $\gamma(HO_2)$ on RO_2 radicals is indirect and not as large. Figure 3.8 suggests that $\gamma(HO_2)$ is a large source of uncertainty in current HO_x simulation studies over pollute regions of China, where aerosol loading is high [Kanaya et al., 2009].

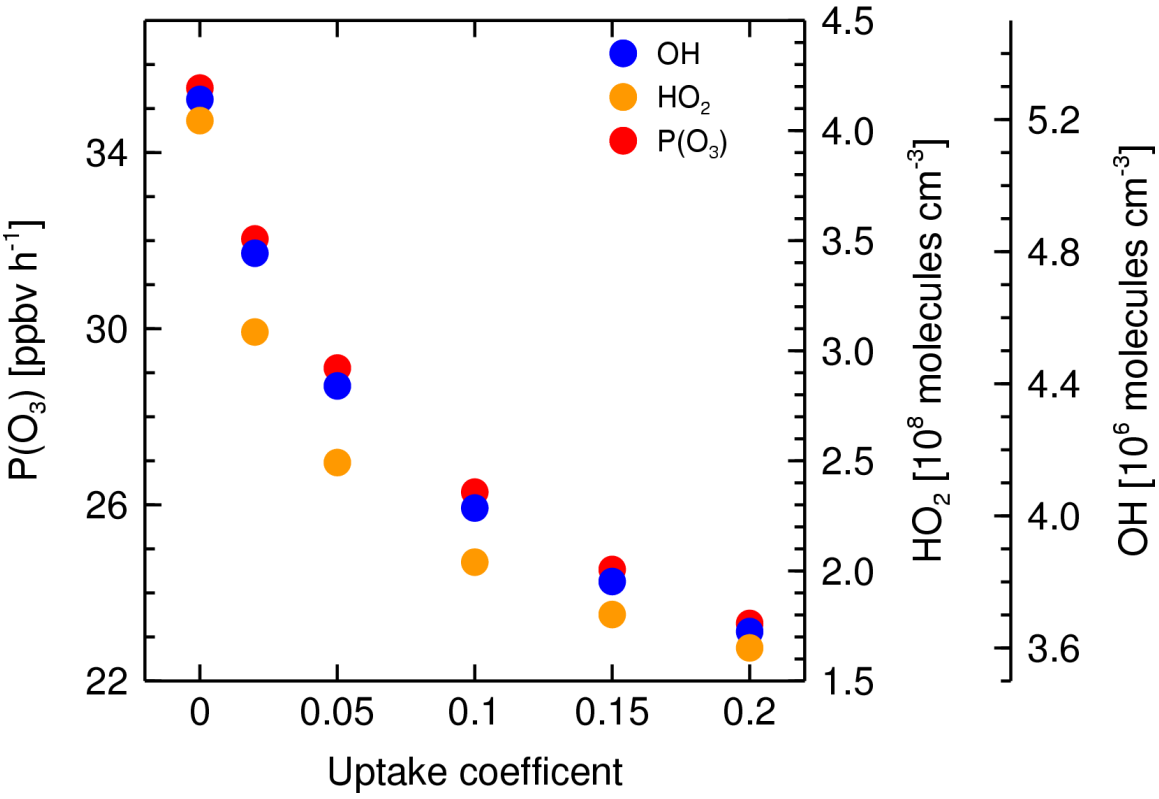

Figure 3.8 Daytime average HO_2, OH and $P(O_3)$ as a function of $\gamma(HO_2)$.

3.3.4 Chemical regimes of O_3 production

We diagnose the $P(O_3)$ chemical regimes in Beijing using two approaches. First, we examine the sensitivity of $P(O_3)$ to perturbations of NO and VOC concentrations; we also try to use previously proposed diagnostic equations [Daum et al., 2000; Kleinman et al., 1997; Sillman et al., 1990] for NO_x-limited and VOC-limited regimes, as has been done in previous studies [Lei et al., 2007]. Since the chemical environment in Beijing is strongly affected various factors, e.g. excess HONO, aromatics, and aerosol uptake of HO_2, not presented in the U. S. where those previous theoretical studies [e.g. Sillman et al., 1990; Kleinman et al., 1997] were conducted, we analyze all the scenarios listed in Table 3.1 and then discuss the possible impacts from those factors on $P(O_3)$ chemical regimes in Beijing.

Sensitivity simulation results

In the sensitivity analyses (Table 3.1), we vary NO and VOCs concentrations (110%, 90%, 70%, and 50% of the observed values) and examine the change of $P(O_3)$, i.e. $\Delta P(O_3)$. $P(O_3)$ consistently show positive responses to ΔNO, i.e. an increase of NO leads to an increase of $P(O_3)$, although the former is always larger than the latter, i.e., the $\Delta P(O_3)$-ΔNO lines are to the left of the 1:1 line. $P(O_3)$ is largely determined by the product of NO and HO_2 (RO_2) concentrations (Figure 3.9a). The non-linear dependence of $P(O_3)$ on NO is a reflection of the dependence of HO_2 and RO_2 on NO. For example, increasing NO leads to decreased peroxy radicals due in part to the conversion of peroxy radicals to OH and RO by reacting with NO; the degree of peroxy radical decrease is also a function of the change in primary RO_x sources and sinks. Comparing scenarios without aromatics and HONO (S3 and S3a) with those with both or either one of them (S0, S1 or

S2), $P(O_3)$ in the former scenarios (S3 and S3a) is much less sensitive to ΔNO (e.g., the flat shapes of the orange lines in Figure 3.9a). The larger sensitivity of peroxy radicals to NO change in S3 and S3a is because of a much smaller primary RO_x source without excess HONO or aromatics or both (section 3.3). Similarly, inspection of the difference between S0 and S0a or among S3, S3a and S3b shows that a larger HO_2 aerosol sink leads to a lesser sensitivity of peroxy radicals to NO and hence a higher sensitivity of $P(O_3)$ to NO.

The complexity of the $P(O_3)$ - NO sensitivity also results in part from the change over the course of a day (Figure 3.10). Generally, $P(O_3)$ shows a larger sensitivity to NO in the afternoon than in the morning. Under different scenarios, such as S0 and S3a in Figure 3.10, $P(O_3)$-NO sensitivities show different transitions over the course of daytime. This daytime transition of $P(O_3)$-NO sensitivity is due to the fast decreasing NO_x from the morning towards the afternoon and thus reducing the importance of NO_x in sequestering radicals, while the primary RO_x source increases into the afternoon.

In contrast to the largely varying degrees of sensitivities of $P(O_3)$ to NO, the sensitivity of PO_3 to VOCs is much more uniform and closer to the 1:1 linear response (Figure 3.9b). The largest deviation from the 1:1 response line is the simulation without aromatics (S2) due to the large impact of aromatics to primary RO_x sources (section 3.3.2). Figure 3.9a and 3.9b show that the $P(O_3)$-VOC response resembles the VOC-limited chemical regime [Sillman et al., 1990], although the $P(O_3)$-NO response does not, suggesting that photochemical O_3 production in Beijing is neither NO_x-limited nor VOC-limited, but lies in a transition regime where reduction of both can reduce $P(O_3)$.

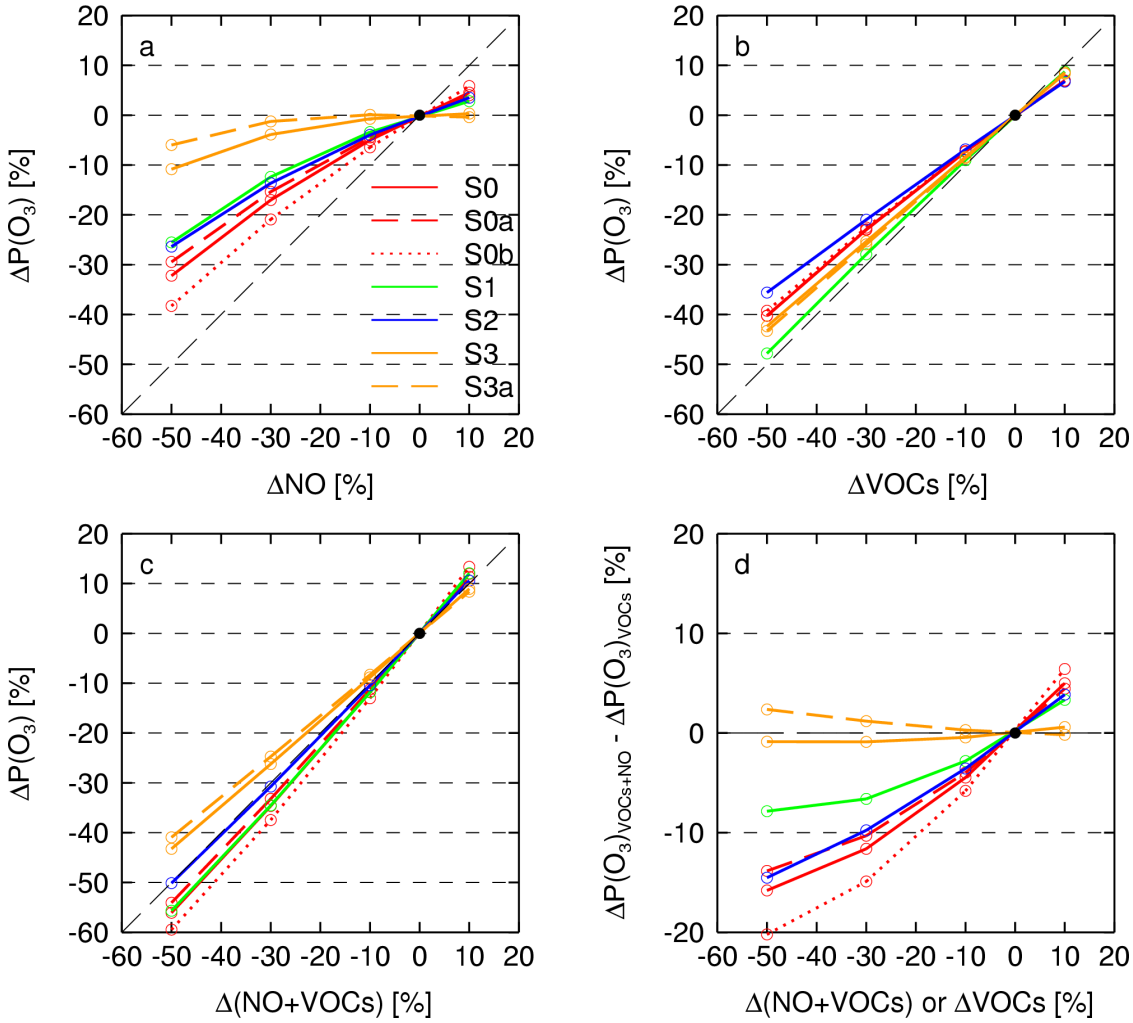

Figure 3.9 Changes of O_3 production ($\Delta P(O_3)$) as a function of NO, VOCs, and both under different scenarios in Table 3.1.

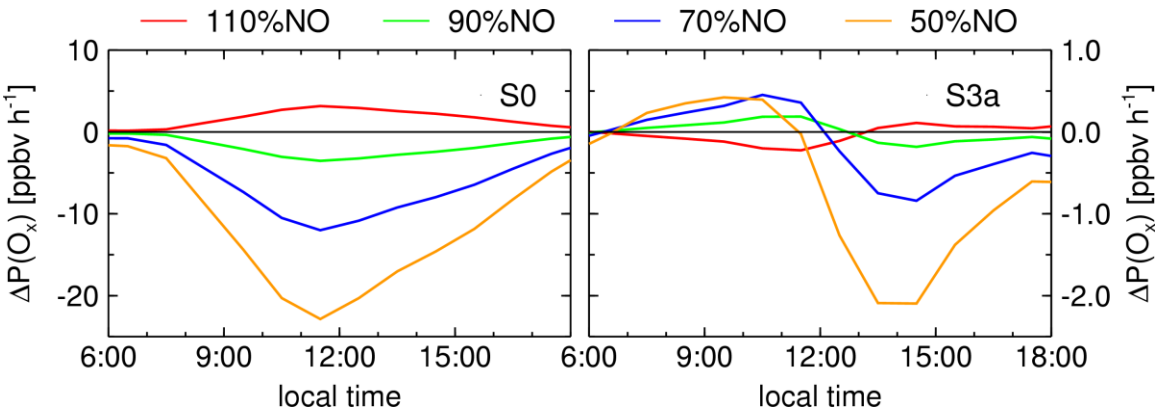

Figure 3.10 Hourly $\Delta P(O_3)$ due to NO changes under S0 and S3a.

Concurrent reduction of NO and VOC concentrations leads to greater $P(O_3)$ reduction than reducing either (Figure 3.9c), although the additional reduction from VOC-reduction only scenarios (Figure 3.9d) varies. In agreement with the $P(O_3)$-NO sensitivity (Figure 3.9a), the least change from the VOC-only scenarios is from the simulations S3 and S3a in which neither excess HONO nor aromatics is included.

Evaluation with diagnostic equations of O_3 production for different chemical regimes

An important implication from Figure 3.9 is that concurrent reduction of both NO and VOCs only gives limited additional $P(O_3)$ reduction than reducing one of them. For example, $\Delta P(O_3)_{NO+VOCs}$ from 50% reductions of both NO and VOC is only 20% more than $\Delta P(O_3)_{VOCs}$ of 50% reduction in VOC (Figure 3.9d for S1b). Under the most likely scenario (with excess HONO and aromatics) based on the in situ observations, reducing either NO_x or VOCs can be effective while reducing both may not bring enough air quality benefits to justify the social-economic costs.

Various studies have provided easier diagnostics on O_3 production regimes [e.g. Sillman et al., 1990; Kleinman et al., 1997; Daum et al., 2000]. Lei et al. [2007] summarized these studies into two equations:

$$\text{NO}_x\text{ – limited regime, } P(O_3) = Y \frac{k_t}{\sqrt{2k_{eff}}} \sqrt{Q - L_N - L_R}[NO] \quad (1)$$

$$\text{VOC – limited regime, } P(O_3) = Y \frac{L_{OH-VOC}}{L_{OH-NO_2}} (Q - 2PER - L_R - L_{ON}) \quad (2)$$

where k_t is the weighted average rate constant for reaction of HO_2 and RO_2 with NO; k_{eff} is the effective rate constant for peroxide (H_2O_2 and ROOH) formation; Q is the total primary source of RO_x radicals, in ppbv h^{-1}; L_N, L_R and L_{ON} are the radical loss rates due to the reactions of OH + HO_2, RO_2 + R'O_2, and radical-NO_x reactions excluding OH + NO_2, respectively; Y is the average yield of HO_2 and RO_2 for each OH + VOC reaction; L_{OH-VOC} and L_{OH-NO_2} are the loss rates of OH due to reactions with VOCs and NO_2, respectively; PER is the peroxide formation rate.

We compare the correlations between model calculated hourly $P(O_3)$ (ppbv h^{-1}) and those from the diagnostic equations [Lei et al., 2007]. The results for different model sensitivity simulations are shown in Table 3.2 and Figure 3.11. We also show in Table 3.2 the correlations with NO and the primary RO_x source Q. In the standard model (S0), $P(O_3)$ shows better correlation with $\frac{L_{OH-VOC}}{L_{OH-NO_2}} (Q - 2PER - L_R - L_{ON})$ (afternoon R^2 = 0.79; daytime R^2 = 0.79) than with the NO_x-limited diagnostics ($\sqrt{Q - L_N - L_R}[NO]$) (afternoon R^2 = 0.50; daytime R^2 = 0.19), mainly due to the much better $P(O_3)$-Q correlation (afternoon R^2 = 0.66; daytime R^2 = 0.74) than the $P(O_3)$-NO correlation

(afternoon R^2 = 0.22; daytime R^2 = 0.002). These suggest that $P(O_3)$ during our observations in Beijing behave more like in the VOC-limited regime than the NO_x-limited regime. This is particularly true when morning data are taken into account since O_3 production can clearly reside in the VOC-limited regime (Figure 3.10). In the afternoon when O_3 production is large, however, both diagnostics show reasonably good correlations with the $P(O_3)$. An outlier is the scenario of S2 when aromatics are not included; the chemical regime clearly shifts into the VOC-limited regime given the much better correlation (R^2 = 0.79) with $\frac{L_{OH-VOC}}{L_{OH-NO_2}}(Q-2PER-L_R-L_{ON})$ than with ($\sqrt{Q-L_N-L_R}[NO]$) (R^2 = 0.26). In the scenario of S0a (without HO_2 aerosol uptake) for the afternoon, $P(O_3)$ correlate even better with the NO_x-limited diagnostics (R^2 = 0.56) than with the VOC-limited diagnostics (R^2 = 0.49). Comparing the results of S0, S0a, and S0b, aerosol uptake of HO_2 tends to shift the O_3 production more towards the VOC-limited regime.

In general, the diagnostic equations are consistent with our sensitivity simulations, suggesting that under the most realistic scenario (S0), O_3 production in Beijing is in the transition regime. Aromatics and excess HONO tend to shift O_3 production into NO_x-limited regime, while aerosol HO_2 sink tends to shift it towards VOC-limited regime.

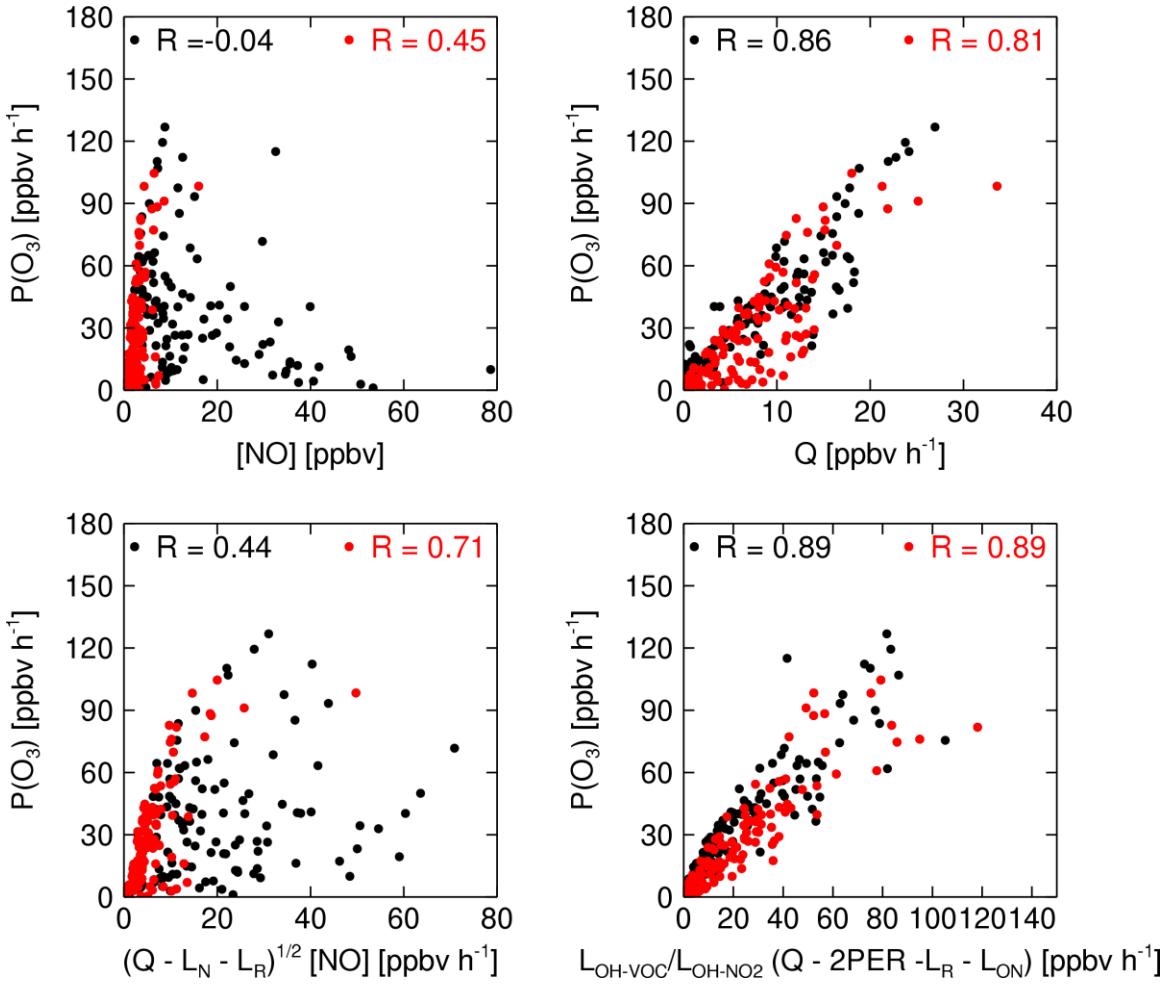

Figure 3.11. Correlations between $P(O_3)$ and [NO], Q, $\sqrt{Q-L_N-L_R}[NO]$ and $\frac{L_{OH-VOC}}{L_{OH-NO_2}}(Q-2PER-L_R-L_{ON})$ in the standard model S0. Black color indicates the daytime (6:00-18:00) data points and red color indicates afternoon (12:00 – 18:00) data points.

Table 3.2 R^2 values beteewn $P(O_3)$ and $\sqrt{Q-L_N-L_R}[NO]$, $\frac{L_{OH-VOC}}{L_{OH-NO_2}}(Q-2PER-L_R-L_{ON})$, Q, and NO during the daytime (6:00 – 18:00) and afteroon (12:00 – 18:00).

	$\sqrt{Q-L_N-L_R}[NO]$		$\frac{L_{OH-VOC}}{L_{OH-NO_2}}(Q-2PER-L_R-L_{ON})$		Q		NO	
	day	afternoon	day	afternoon	day	afternoon	day	afternoon
S0	0.19	0.5	0.79	0.79	0.74	0.66	0.002	0.2
S0a	0.18	0.56	0.49	0.49	0.79	0.72	0.002	0.18
S0b	0.2	0.34	0.72	0.77	0.58	0.46	0.002	0.14
S1	0.09	0.69	0.77	0.77	0.86	0.85	0.03	0.09
S2	0.14	0.26	0.77	0.79	0.49	0.34	0.01	0.06
S3	0.1	0.59	0.76	0.79	0.77	0.72	0.07	0.03
S3a	0.06	0.56	0.76	0.77	0.62	0.79	0.08	0.03

3.4 Conclusions and implications

Through a detailed chemical budget analysis, we find that summertime photochemistry in Beijing is driven by fast formation, recycling and removal of RO_x radicals. The total RO_x primary source (and sink) (6.6 ppbv h^{-1}) in Beijing is close to the largest values reported for urban environments. Photolysis of OVOCs (4.2 ppbv h^{-1}) and excess HONO (2.2 ppbv h^{-1}) are the two largest RO_x sources, much more important than that from O^1D+H_2O (0.4 ppbv h^{-1}). Formation of RO_2NO_2 (1.0 ppbv h^{-1}) and $RONO_2$ (0.7 ppbv h^{-1}) are as important as the typical major RO_x sink via $OH+NO_2$ reaction (1.6 ppbv h^{-1}). Aromatics are the major player in OVOC and organic nitrate formation. Aerosol uptake of HO_2 may also be a major RO_x sink due to the large aerosol surface area in Beijing, although this sink is quite sensitive to the value of $\gamma(HO_2)$. The importance of aromatics, heterogeneous HONO production, and possibly large aerosol uptake of HO_2 signifies the unique photochemical environments in Beijing. These characteristics are likely to be present over many regions of the polluted eastern China with large clusters of cities and industrial regions. Observation-based modeling studies of RO_x radical chemistry over these regions by including high quality comprehensive measurements of RO_x radicals, HONO, organic nitrates, and VOCs (aromatics in particular) and their oxidation products will be necessary to reduce the uncertainties of the factors discussed in this study and develop more accurate quantitative understanding of the chemical system.

The chemical production of O_3 in Beijing is extremely fast, at 32 ppbv h^{-1} on average during daytime. The high concentrations of NO (~5 ppbv at noontime), excess HONO and aromatic VOCs are the major driving factors. The chemical loss of O_3 is also

fast, about 6 ppbv h^{-1}, and the heterogeneous formation of excess HONO via $NO_2 \rightarrow$HONO is actually the largest (~40%) O_3 loss term. Sensitivity simulations and analysis using diagnostic equations suggest that the O_3 production in Beijing does not lie in either the VOC-limited regime or in the NO_x-limited regime, but in the transition regime, where reduction of either NO_x or VOCs could lead to reduced O_3 production. In the transition regime, the co-benefit of concurrent reduction of both NO_x and VOCs is small, which may not bring enough air quality benefits to justify the social-economic costs. However, it also implies that there is flexibility in choosing either NO_x or VOC reduction to achieve the most cost-effective O_3 reduction.

In this study, we have focused on understanding the photochemistry using observation-constrained modeling. Our results point to the chemical characteristics not yet well represented in current 3-D modeling studies. The large clustering of concentrated city and industrial regions in the eastern China, such as North China Plain (NCP), Yangtze River Delta (YRD), and PRD, would suggest that fast photochemistry plays a critically important role in determining O_3 levels in these regions. 3-D modeling analysis, ideally constrained by in situ or remote sensing observations, will be necessary to understand the interplay of chemistry and transport on the regional and global scales.

4. [3]PHOTOENHANCED AEROSOL HETEROGENEOUS SOURCE OF DAYTIME HONO AND AMPLIFIED OXIDATION CAPACITY OVER CHINA

4.1 Background and motivation

Daytime HONO much higher than expected from gas-phase HONO chemistry have been observed in various environments, including urban and suburban polluted atmospheres [Acker et al., 2006b; Alicke et al., 2002; Alicke et al., 2003; An et al., 2009; Bari et al., 2003; Costabile et al., 2010; Elshorbany et al., 2009a; Hofzumahaus et al., 2009; Kanaya et al., 2007; Li et al., 2011; Qin et al., 2009; Stutz et al., 2002; Su et al., 2008; Wong et al., 2011; Ziemba et al., 2010] and background clean regions [Kleffmann et al., 2005; Wentzell et al., 2010; N Zhang et al., 2009; Zhou et al., 2002; Zhou et al., 2011]. Photolsysis of the "excess" HONO apparently serves as a major (and in some cases the predominant) primary OH source, and a driver of photochemistry over these regions. Nevertheless, the source of the daytime excess HONO remains unclear.

Laboratory studies and atmospheric observations consistently indicate that the missing daytime HONO source is the most probably some heterogeneous reduction of oxygenated nitrogen species (primarily NO_2, HNO_3) on surfaces [Finlayson-Pitts, 2009; Finlayson-Pitts et al., 2003]. While thermodynamic hydrolysis of NO_2 has been found to be the main heterogeneous HONO source at night [Finlayson-Pitts et al., 2003; Stutz et al., 2002], certain photochemical processes appear to operate during daytime, which is

[3] This chapter is an extension of "Photoenhanced aerosol heterogeneous HONO source and amplified regional oxidation capacity to be submitted. Co-authors are Y. Wang, C. Zhao, A. Amoroso, F. Costabile, L. G. Huey, R. Stickel, J. Liao, L. Zeng and T. Zhu.

supported by the radiation enhancement of NO_2 uptake on various surfaces during controlled experiments [Kleffmann, 2007], an also by the pronounced diurnal cycle of the missing HONO source inferred from observations in the atmosphere [Su et al., 2008].

An important issue that remains elusive is the roles of different surfaces, i.e. surfaces of ground and those of aerosols, in HONO formation. Aerosol and ground surfaces interfere with the atmosphere in different manners given their different spatial distributions. HONO formed on aerosol or ground surfaces has quite different vertical distributions and implies contrasting importance of HONO in atmospheric chemistry. It has been speculated that aerosol surface is only of minor importance due to the presumably too small surface-to-volume ratio. However, to our knowledge, no direct evidence has been shown so far to support this argument. Intriguingly, recent observed vertical profiles of HONO or HONO/NO_x ratios actually do not exclude or even support the existence of certain airborne HONO source [Kleffmann, 2007; Villena et al., 2011; Vogel et al., 2003; Wong et al., 2011; N Zhang et al., 2009].

A major challenge in apportioning daytime HONO sources is the very low atmospheric HONO concentrations, often close to the instrument detection limit, due to the fast photolysis of HONO offsetting the not strong enough HONO source strength [Kleffmann, 2007]. A survey of daytime HONO observations in the past decade reveals that those over China are outstanding. High HONO concentrations are observed during daytime at multiple sites over polluted regions in China, accompanied by actually moderate levels of HONO precursors (NO_x) relative to those outside China, pointing to a hitherto unknown HONO source that is much larger than most of other places.

4.2 Methods

4.2.1 HONO measurement method

HONO was measured with a liquid coil scrubbing/UV–vis instrument. Briefly, gaseous HONO was trapped quantitatively in a 10-turn coil sampler using 1mm phosphate buffer. The scrubbing solution was then derivatized with sulfanilamine (SA)/N-(1-naphtyl)-ethylendiamine (NED), subsequently analyzed using high-performance liquid chromatography (HPLC), and detected by UV-vis absorption. Interferences during sampling were studied in our laboratory in Rome and directly at Beijing using sodium carbonate denuders. We used the denuder respectively in front of the Teflon tube and before the trap coils. The denuder in front of Teflon tube was used to study the possible formation of HONO from NO_2 and humidity on the tubing walls. While, the denuder before the inlet traps was used to study the nitrite formation in the water solution due to: $NO_3^- + SO_3 \rightarrow NO_2^- + SO_4^{2-}$. Under summer conditions at Beijing we observed interferences on the order of 2–9% of the observed HONO mixing ratio. The inlet tube was 70 cm and the residence time of the air in the tube was less than 2 sec. The detection limit of the HONO instrument is less than 0.8 pptv. The uncertainty for HONO measurements is estimated to be 10%.

4.2.2 The REAM-1D model

The 3-D version of the Regional chEmical and trAnsport Model (REAM-3D) has been applied in a number of studies on O_3 photochemistry and transport at north mid-latitudes [Choi et al., 2005; Wang et al., 2007; Choi et al., 2008a; Choi et al., 2008b; Zhao et al., 2009ab; Zhao and Wang, 2009; Zhao et al., 2010; Yang et al., 2011]. The

REAM-1D model shares the modules for O_3-NO_x-hydrocarbon photochemistry, vertical diffusion, convective transport, and wet/dry deposition [Liu et al., 2010] with the REAM-3D model. The chemical kinetics data were updated with the latest compilation by Sander et al. [2011], and the VOC chemistry in REAM-3D is expanded to include the chemistry of aromatics based on the SAPRC-07 chemical mechanism [Carter, 2009]. Vertical transport is driven by WRF assimilated meteorological fields based on the NCEP reanalysis data [Zhao et al., 2009a].

The model is constrained with measured CO, O_3, NO, HONO, NMHCs (C_2–C_9), OVOCs (acetone, acetaldehyde and formaldehyde) and aerosol surface areas and was run with a 1–minute time step from 1 August to 30 August 2007. The results for the last 20 days were analyzed after a spin-up time of 10 days. The REAM-1D model has been shown to be able to reproduce the observed PAN in Beijing, which is sensitive to the VOC oxidation mechanism and transport within the boundary layer [Liu et al., 2010]. Our model simulated OVOCs, including formaldehyde, acetaldehyde, and acetone, agree with the observations within 20% in terms of diurnal average concentrations, indicating that secondary production is the predominant source. Additional detailed descriptions of the REAM-1D model including VOC input and model error estimates are available in Appendix A.

4.2.3 Parameterizations of aerosol and ground heterogeneous HONO sources

The aerosol uptake of NO_2 is parameterized as Eq. (4.1):

$$k_a = -\sum_{i=1}^{n}\left[\frac{r_p^i}{D_g} + \frac{4}{\gamma\omega}\right]^{-1} A_i \qquad (4.1)$$

in which k_a is the first order rate coefficient; D_g is the gas phase molecular diffusion coefficient ($m^2 s^{-1}$) for NO_2; A_i and r_p are the particle radius (μm) and surface area ($\mu m^2 cm^{-3}$) for the i th size bin; γ is the reactive uptake coefficient; ω is the mean molecular speed of NO_2 in the air ($m\ s^{-1}$).

The ground uptake of NO_2 is parameterized to resemble the dry deposition process of NO_2, as described in Eq. (4.2)

$$k_g = f \times \frac{1}{r_a + r_b} \times \frac{1}{h} \tag{4.2}$$

in which k_g is the first order rate coefficient; r_a and r_b are aerodynamic resistance and resistance in the quasi-laminar layer near the surface, respectively; h is the height of first model layer near the surface (m); f is an 'apparent' yield of HONO from NO_2 and is assumed to be 1 to allow a maximum source strength from the ground and is adjusted to 0.5 for the purpose of sensitivity test.

4.3 Results and discussions

4.3.1 Observational evidence of photoenhanced aerosol uptake of NO_2

We investigate the missing daytime HONO source over China by analyzing in situ observations of HONO and associated trace gases and parameters at an urban site in Beijing during the summer of 2007. Constantly elevated daytime HONO was observed throughout the experiment period, with an average of 0.8 – 1 ppbv in the afternoon (Figure 4.1). NO_x concentrations are actually not very high (~16 ppbv in total, including 5ppbv of NO and 11ppbv of NO_2), leading to a ratio of $HONO/NO_x$ at 0.05 – 0.06. A budget analysis of HONO sources using an observation-based 1-D model shows that the

gas-phase NO and OH reaction only accounts for ~10% of the total HONO source, while an unknown excess HONO source with a daytime maximum of ~5 ppbv h^{-1} is required to explain the observed HONO during daytime [Z Liu et al., 2012]. The observed $HONO/NO_x$ ratio is larger than typical emission ratio of $HONO/NO_x$ (around 0.5%) despite of the much shorter lifetime of HONO than NO_x, indicating the minor contribution from direct HONO emission. Therefore, about 90% of observed HONO should be coming from the excess HONO source that remains to be explored. Assuming NO_2 to be the precursor for this missing source, $HONO/NO_2$ ratio could be used as a measure of the efficiency of NO_2-to-HONO conversion. The sharp noontime peak of $HONO/NO_2$ ratio corresponding to the peak of UVA radiation in Figure 4.1 has been regarded as evidence for radiation enhanced NO_2-to-HONO conversion [Ramazan et al., 2004; Wong et al., 2011]. We note that the strength and the radiation enhancement of the excess HONO source at Beijing are comparable to those at two suburban sites over the Perl River Delta region in southern China. Such large amount of excess HONO acts as the predominant primary OH source over these places [Hofzumahaus et al., 2009; Z Liu et al., 2012; Su et al., 2008].

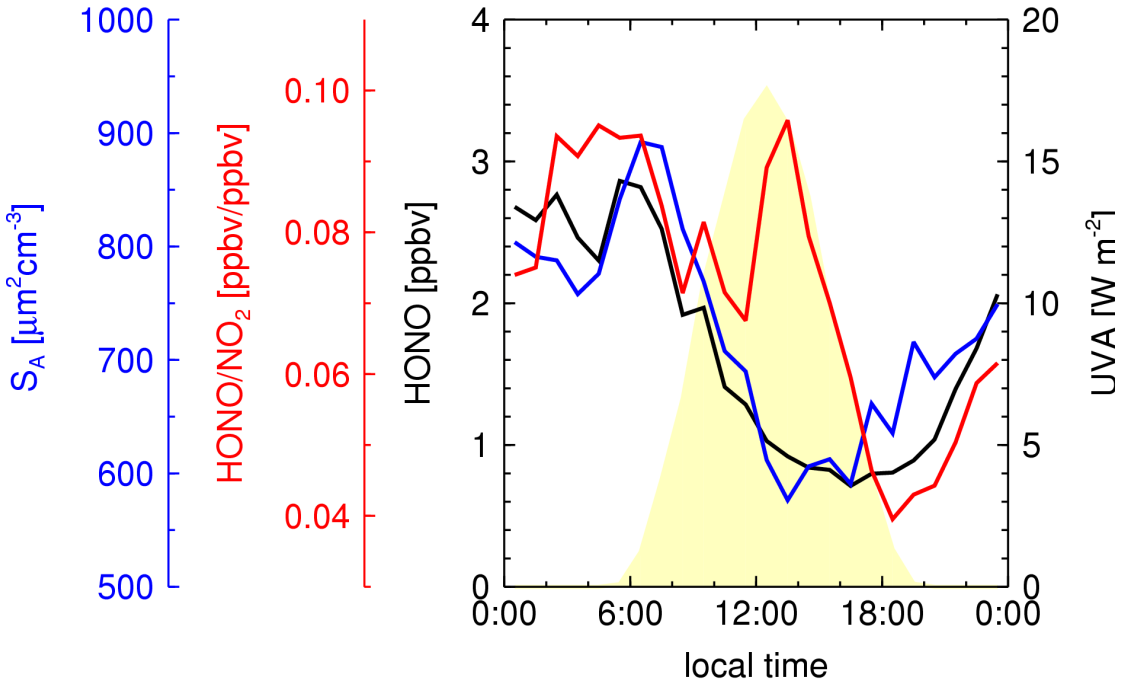

Figure 4.1 Average diurnal profiles of HONO, aerosol surface area (S_A), HONO/NO_2 ratio, and UVA radiation.

High loading of aerosols at Beijing in summer provides a potential interface for heterogeneous reactions. Calculated aerosol surface area S_A based on the observed 3nm - 10μm aerosol size distributions is ~750 um^{-2} cm^{-3} on average, with considerable viability from 100 to 1300 $um^{-2}cm^{-3}$ during daytime. S_A and HONO show very similar diurnal profiles (Figure 4.1), which has also been found in previous studies over China and was speculated to be evidence for an aerosol HONO source [An et al., 2009]. Because aerosols and HONO have quite different lifetimes during daytime, therefore it is possible that the chemical link between them two may be the reason for their correlation [An et al., 2009].

With the attempt to explore such a possibility, we further find that HONO/NO_2 ratio and S_A are also correlated (Figure 4.2). Although the degree of correlation is not

high given the scattered data points, the averaged $HONO/NO_2$ ratios binned by S_A clearly shows an upward trend of $HONO/NO_2$ ratio as a function of S_A. If the $HONO/NO_2$ ratio is indicative of NO_2-to-HONO transformation efficiency, the increase of $HONO/NO_2$ ratio corresponding to increased S_A suggests more efficient HONO formation under high aerosol loading. A closer inspection of Figure 4.2 shows that the $HONO/NO_2$ ratio of 0.04 corresponding to the lowest S_A (100 - 300 $\mu m^{-2}cm^{-3}$) is still higher than expected from gas-phase PSS HONO concentrations (~0.005). A non-aerosol heterogeneous HONO source, e.g. ground uptake of NO_2, may be responsible for the rest of NO_2 to HONO transformation and the enhancement of the $HONO/NO_2$ ratio. The evident enhancement of $HONO/NO_2$ ratio corresponding to increasing S_A in Figure 4.2 provides direct observational evidence for the enhancement of HONO formation due to aerosols.

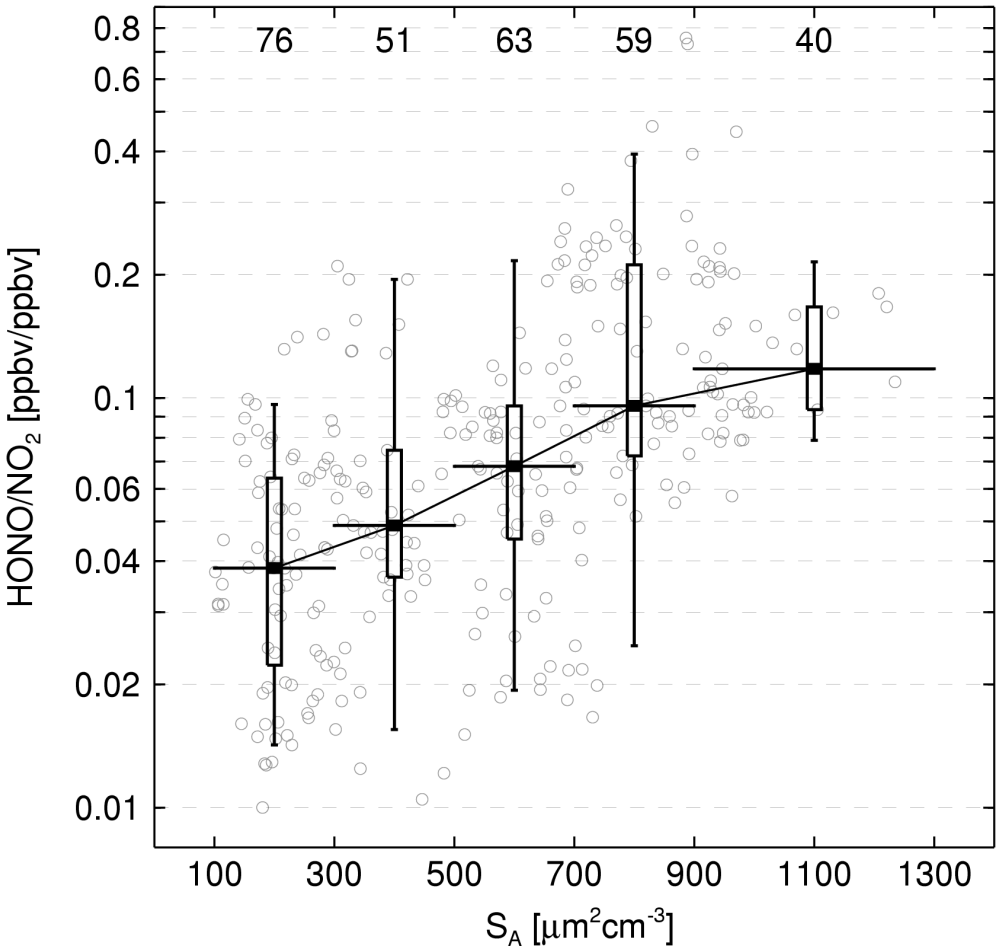

Figure 4.2 Dependance of $HONO/NO_2$ ratio on S_A; gray dots include a total of 345 10-minute merged data points during 10:00 – 15:00; the horizontal error bars indicate the bin size of S_A for each whisker box and there are more than 40 data points in each bin; the vertical error bars, box edges and black squares in the box indicate, respectively, (from top to bottom) 95% percentile, 75% percentile, median, 25% percentile and 5% percentile of the $HONO/NO_2$ ratios in each bin.

To confirm the role of aerosols in HONO formation, we also examine the correlations between the excess HONO source strength (pHONO) with various factors. pHONO shows some degree of dependence on NO_2 (R = 0.18) and UVA radiation (R = 0.32) (Figure 4.3(a)(b)). Further, a better correlation is found between pHONO and the product of NO_2 and UVA (R = 0.43 in Figure 4.3(c)), suggesting that both NO_2 and solar radiation are playing a role in this HONO source. If aerosol surfaces indeed play a role as inferred from Figure 4.2, one would expect the correlation with pHONO to further improve when S_A is incorporated into the product, i.e. $NO_2 \times UVA \times S_a$. This actually would also be in line with the gas-to-particle transfer rate approximation, in which the NO_2 transfer flux is proportional to the product of surface area (S_A) and the concentration in the gas phase (NO_2). Remarkably, in Figure 4.3(d) the correlation between pHONO and the product of NO_2, UVA and S_a turns out to be much better than those in Figure 4.3(a)(b)(c) with correlation coefficient increased to 0.67. The correlation coefficient does not get higher mainly due to measurement uncertainties for HONO, NO_2 and S_A and interference of pHONO from additional HONO sources such as the ground surface.

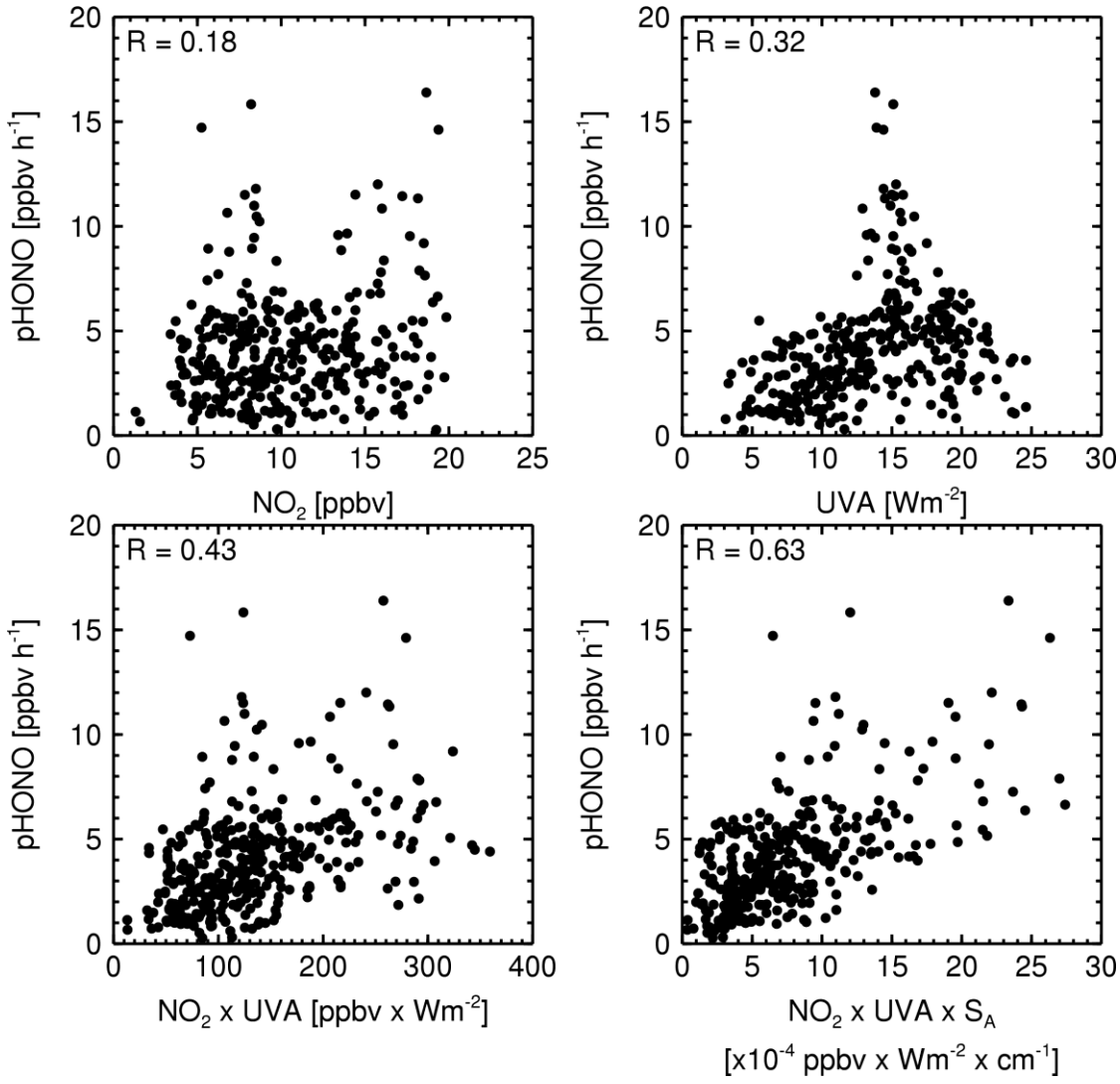

Figure 4.3 Correlations between the excess HONO production rates (pHONO) and (a) NO_2 mixing ratios, (b) UVA, (c) product of NO_2 mixing ratios and UVA (S_A), (d) product of NO_2 mixing ratio, UVA and S_A. 10-minute merged data during 10:00 – 15:00 are shown.

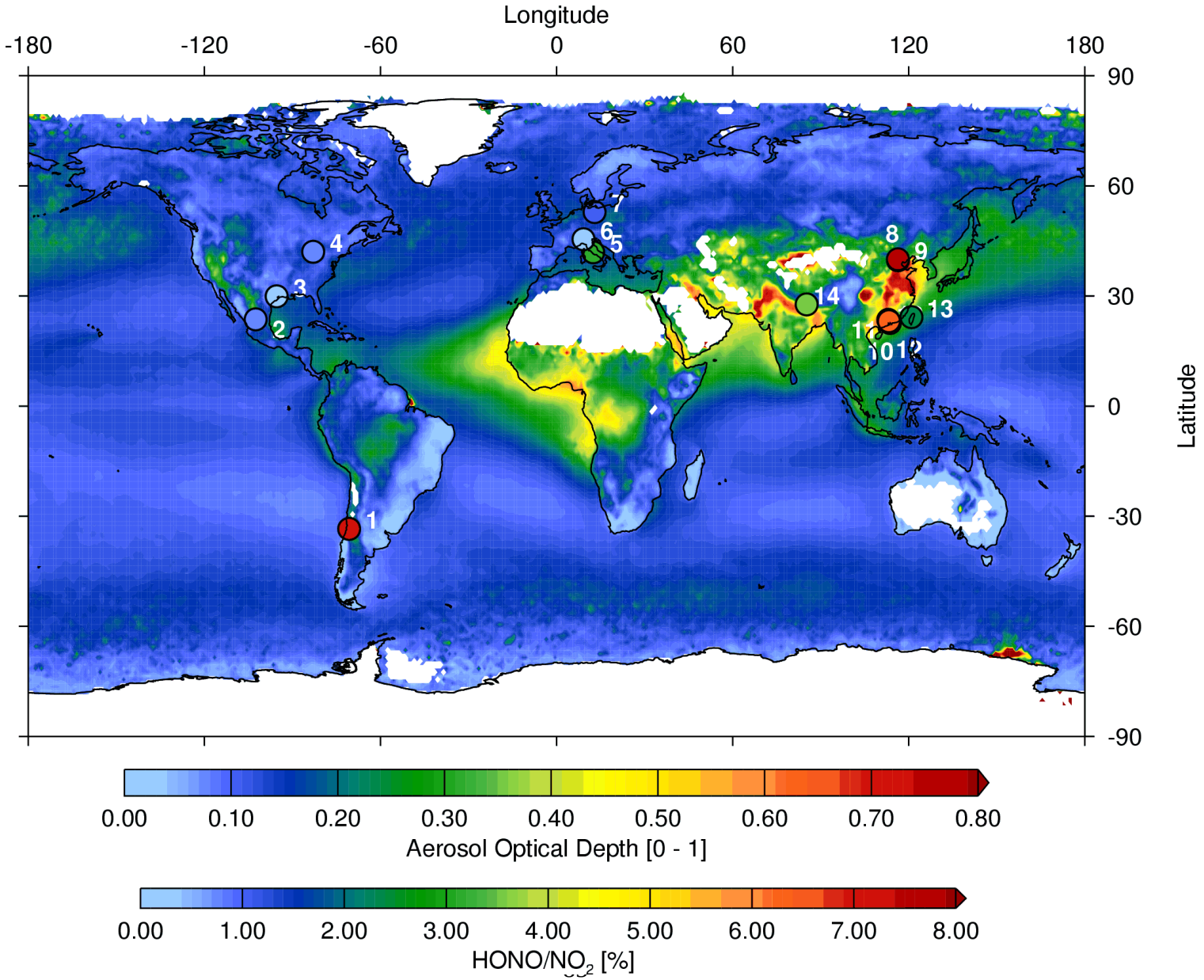
Longitude
-180
-120
-60
0
60
120
180
90
60
30
0
-30
-60
-90
Latitude
1
2
3
4
5
6
7
8
9
13
14
0.00
0.10
0.20
0.30
0.40
0.50
0.60
0.70
0.80
Aerosol Optical Depth [0 - 1]
0.00
1.00
2.00
3.00
4.00
5.00
6.00
7.00
8.00
HONO/NO2 [%]

Figure 4.4 Average global distribution of MODIS Aqua aeorosol optical depth (AOD) at 550nm from 2002-2011 and $HONO/NO_2$ ratios observed at 14 sites. 1. Santiago (33.45S, 70.67E); 2. Mexico (23.63N, 102.51W); 3. Houston (29.9N, 95.36W); 4. Harrow (42.03N, 82.92W); 5. Rome (41.9N, 12.5E); 6. Milan (45.45N, 9.18E); 7. Pabstthum (52.85N, 12.96E); 8. Yufa (39.72N, 116.33E); 9. Beijing (39.99N, 116.31E); 10. Xinken (22.63N, 113.6E); 11. Backgarden (23.5N, 113.03E); 12. Guangzhou (23.12N, 113.25E); 13. Taichung (24.23N, 120.93E); 14. Kathmandu (27.7N, 85.22E). For details of these observations see Table 4.1.

Table 4.1 Previous daytime HONO observations over polluted regions. The concentrations and ratios are average values during 12:00 – 15:00.

NO	site	country	time	HONO	NO_x			AOD	HONO/NO_x	HONO/NO_2	Reference
					NO	NO_2	NOx				
1	Santiago (33.45S, 70.67E)	Chile	Mar 2005	1.5	20	20	40	0.216	0.038	0.075	Elshorbany et al., 2009
2	Mexico (23.63N, 102.51W)	Mexico	Mar 2006	0.43	16.4	28.4	44.8	0.162	0.010	0.015	Dusanter et al., 2009
3	Houston (29.9N, 95.36W)	USA	Sep 2006	0.1	NA	10	10	0.160	0.010	0.010	Wong et al., 2011
4	Harrow (42.03N, 82.92W)	Canada	Jun 2007	NA	NA	NA	NA	0.186	0.015	0.015	Wentzell et al., 2010
5	Rome (41.9N, 12.5E)	Italy	May-Jun 2001	0.15	1	4	5	0.175	0.030	0.038	Acker et al., 2006
6	Milan (45.45N, 9.18E)	Italy	May 1998	0.14	5.1	18.3	23.4	0.271	0.006	0.008	Alicke et al., 2002
7	Pabstthum (52.85N, 12.96E)	Germany	Jul-Aug 1998	0.07	1	3.6	4.6	0.164	0.015	0.018	Alicke et al., 2003
8	Yufa (39.72N, 116.33E)	China	Jul-Aug 2006	0.43	1.4	8	9.4	0.584	0.046	0.054	Yang et al., 2010
9	Beijing (39.99N, 116.31E)	China	Jun 2006	0.9	5	11	16	0.584	0.056	0.082	This study
10	Xinken (22.63N, 113.6E)	China	Oct-Nov 2004	0.8	10	30	40	0.869	0.020	0.027	Su et al., 2008
11	Backgarden (23.5N, 113.03E)	China	Jun 2006	0.24	1	4.5	5.5	0.596	0.044	0.053	Li et al., 2011
12	Guangzhou (23.12N, 113.25E)	China	Jun 2006	2	NA	30	30	0.596	0.067	0.067	Qin et al., 2009
13	Taichung (24.23N, 120.93E)	China	Jul-Jan 2005/06	0.5	NA	16.7	16.7	0.355	0.030	0.030	Cheng et al., 2008
14	Kathmandu (27.7N, 85.22E)	Nepal	Jan-Feb 2003	0.35	4.4	8.6	13	0.292	0.027	0.041	Yu et al., 2009

[Acker et al., 2006a; Alicke et al., 2002; Alicke et al., 2003; Dusanter et al., 2009; Elshorbany et al., 2009a; Li et al., 2012; Qin et al., 2009; Su et al., 2008; Wentzell et al., 2010; Wong et al., 2012; Yu et al., 2009]

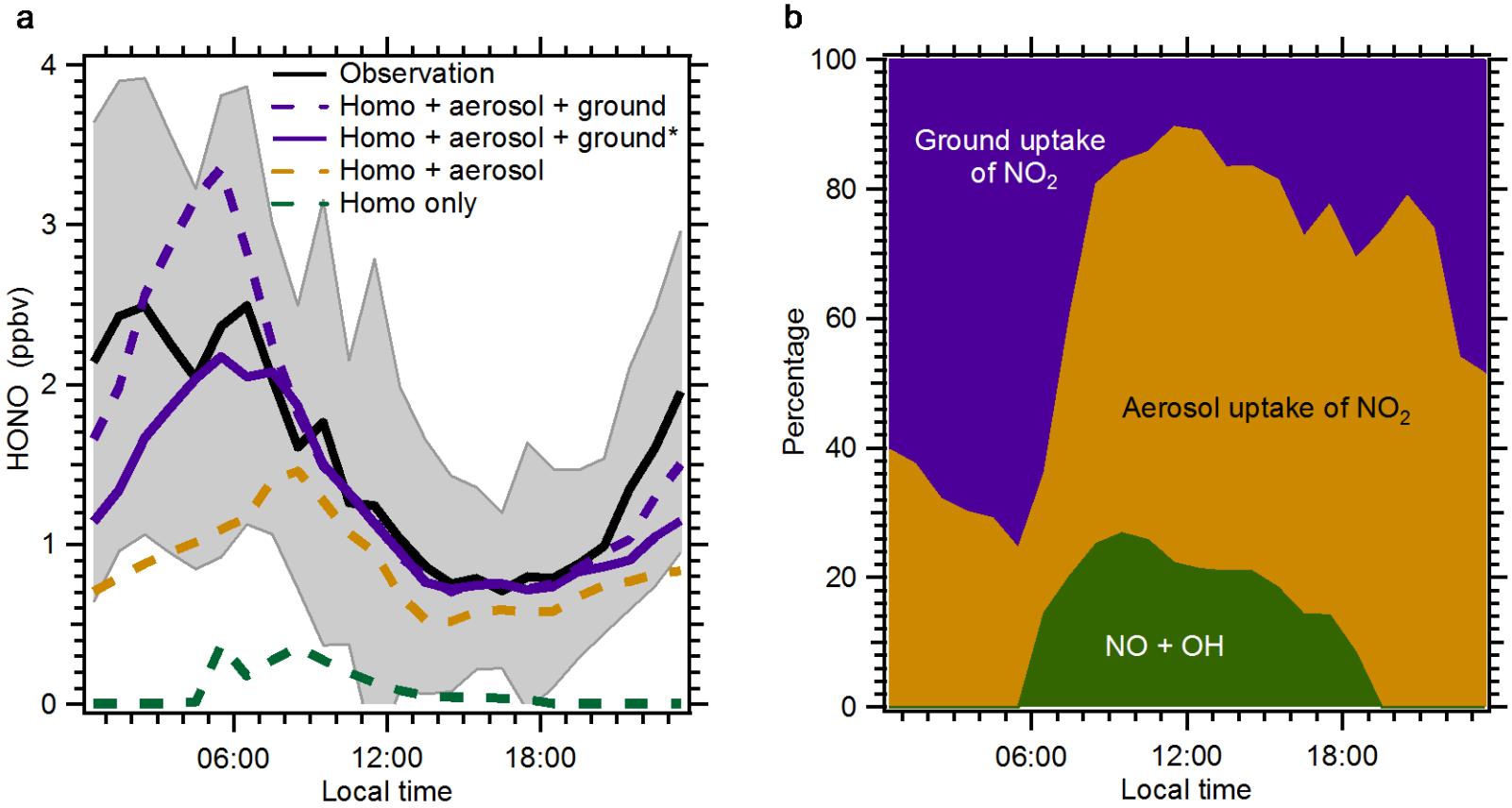

Figure 4.5. (a) Observed and model simulated average HONO diurnal profiles; the purple solid and dashed lines indicate two scenarios with 50% and 100% yield of HONO from NO_2; (b) breakup (%) of the contributions from 3 processes to HONO formation.

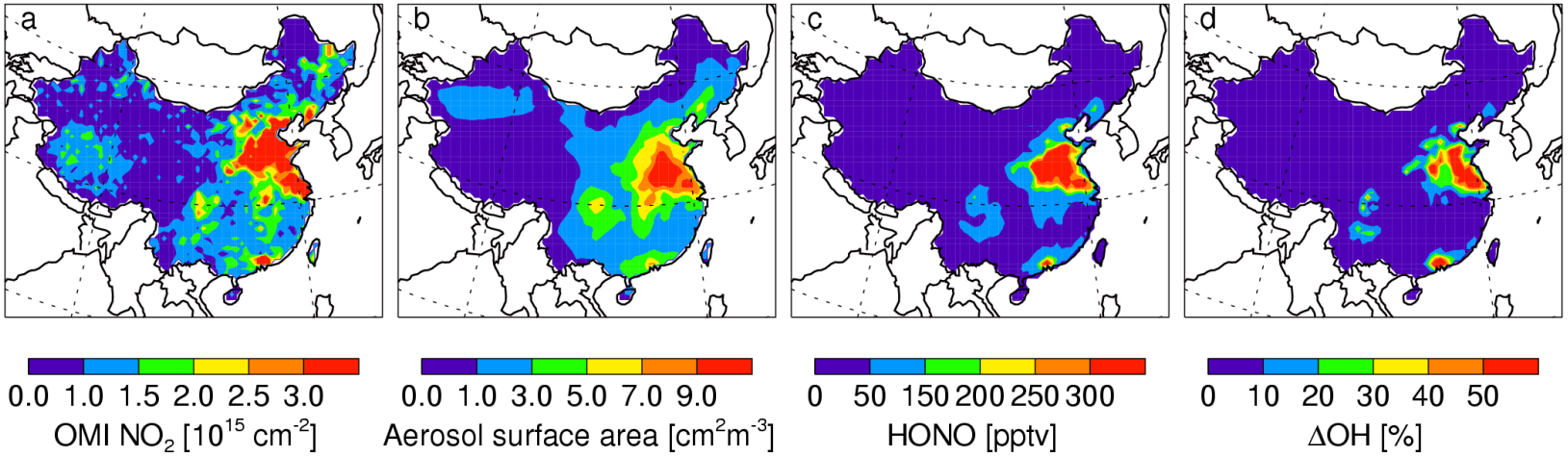

Figure 4.6 Monthly mean spatial distributions of a number of variables over China during August of 2007: (a) OMI NO_2 tropospheric columns; (b) 24-h averaged WRF-Chem model simulated aerosol surface areas; (c) REAM-3D model simulated afternoon (13:00) HONO mixing ratios and (d) changes of OH concentrations as seen in comparing two simulations with and without non-homogenious HONO formation processes.

The dependence of $HONO/NO_2$ ratio on S_A (Figure 4.2) and the correlation comparisons in Figure 4.3 combined suggests that aerosol uptake of NO_2 may be the key process leading to the high daytime HONO level in Beijing. In addition, we find notable degrees of correlations between HONO or pHONO and chemical components in aerosols, such as PAHs, black carbon, which have all been suggested to react with NO_2 producing HONO in laboratory studies. It is not clear which one of these components are more important in HONO formation. The extraordinary aerosol abundance and complex chemical composition in Beijing might both contribute to the important role of aerosols in HONO formation.

We also tried to understand why previous observations over polluted regions outside China did not find such a large HONO source on aerosol surfaces, as we show here for Beijing. The extraordinary aerosol abundance over eastern China has been shown by satellite observed aerosol optical depth (AOD). We plot the observed $HONO/NO_2$ ratios from literature in the last decade on a global map of AOD. Remarkably, the spatial patterns of AOD and $HONO/NO_2$ ratios are quite consistent in Figure 4.4. Especially, the high aerosol loading over China leads to substantially higher $HONO/NO_x$ ratios than other places. Therefore, the aerosol abundances in previous studies outside China are not high enough to generate an adequate aerosol HONO source that could be manifested in their HONO observations.

4.3.2 Simulation of HONO using REAM-1D

Our analyses so far suggest that the missing HONO source at Beijing is comprised of heterogeneous processes taking place on aerosols and ground, with the former being predominant. To quantifying the contributions from these two heterogeneous HONO sources, we conducted modeling analyses using our 1-D model. We parameterize the HONO formation in the model to be ground and aerosol surface uptake of NO_2. The ground uptake process is parameterized to resemble that of dry deposition of NO_2 and subsequent release of HONO. We first assume a unity yield of HONO from NO_2, which implies the largest possible contribution from ground. For aerosol uptake, we use the average accommodation coefficient of NO_2 (γ) from literature in the dark for nighttime, and assume a linear dependence of the γ on solar short wave radiation for daytime. The range of γ is determined such that a best agreement with observed HONO can be achieved. Figure 4.5 shows the model results against observations on a diurnal basis. Ground uptake of NO_2 is the dominant source over the night (50% -- 75%), and becomes less important during the day (~20%). Aerosol heterogeneous source contributes roughly 70% of the total HONO formation during daytime. OH plus NO reaction shows a peak in the morning hours and contributes constantly lower than 25% of the total HONO. Since the ground source has been parameterized to make the largest possible contribution, these model results confirmed that the aerosol heterogeneous reaction is the most important daytime HONO source and largely regulates the variability of the heterogeneous HONO source and HONO/NO_2 ratio. The noises due to non-aerosol HONO sources and measurement errors are the reasons why the variability of pHONO could only be partially explained by the aerosol surface area (R^2 = 0.40, Figure 4.3d). We note that the required γ values in the model to

reproduce the daytime HONO level (on the order of 10^{-4} – 10^{-3}) is at the upper bound of those experimental values [Kleffmann, 2007]. More experimental studies targeting aerosols with similar composition as that in Beijing are needed to reconcile our findings with laboratory studies and to assess if the aerosol heterogeneous source in Beijing is applicable to other polluted regions.

4.3.3 Regional distribution of the photoenhanced aerosol heteronomous HONO source

Assuming comparable chemical environments, e.g. aerosol composition, over polluted regions in China, we extrapolate the aerosol heterogeneous HONO source in Beijing to much broader polluted regions over China. We conducted a regional model simulation with the 3-D REAM model using the identical parameterization of HONO sources as in the 1-D model. Figure 4.6 shows that due to the broadly distributed high abundance NO_2 and aerosols, noontime HONO concentrations above 200 pptv are found over most of the East China Plain (ECP), and the Pearl River Delta (PRD). Although these results are subject to the accuracy of model simulated NO_2 and aerosol surface areas, as well as model resolution, the model results showing the high concentration of HONO on a regional level is robust and within expectation, given that the NO_x concentrations and S_A over these regions are comparable or even larger than those at Beijing (Figure 4.6(a)(b)).

4.4 Implications for regional oxidative capacity and air quality

A direct consequence due to the large daytime HONO abundance is enhanced OH centration [Z Liu et al., 2012]. By comparing model simulated OH concentrations with

and without the aerosol heterogeneous HONO source, we find that the aerosol heterogeneous HONO source could result in 20% - 70% enhancement of OH concentrations over ECP and PRD. Due to formation of HONO, the interaction between NO_x and aerosols, both being outstandingly abundant over China, turns out to provide a large primary source of OH, leading to accelerated photochemistry and shortened lifetimes of pollutants. Furthermore, HONO may also have great impact on reactive nitrogen partitioning and deposition through modifying gas phase chemistry and gas/particle portioning [Pathak et al., 2009]. Better understanding and proper representation of HONO formation and other heterogeneous processes in CTMs is essential for reasonably reproduce the regional photochemical environment featuring tight gas and particulate chemical coupling over polluted regions in China. We also note that this aerosol heterogeneous HONO source may also exist historically over other polluted regions, such as over California of the U.S., given the documented even higher aerosol and NO_x concentrations over these places. The way of HONO formation and other heterogeneous processes affect air pollution control effectiveness and air quality trend of over these places are worth further exploring [Meng et al., 1997].

5. [4]EXPLORING THE MISSING SOURCE OF GLYOXAL (CHOCHO) OVER CHINA

5.1 Background and motivation

CHOCHO (CHOCHO) is the smallest di-carbonyl compound and an oxidation product of many unsaturated volatile organic carbons (VOCs) such as isoprene and aromatics. Observations of CHOCHO provide useful constraints on emissions of these VOCs emissions since the primary emissions of CHOCHO are small [Volkamer et al., 2005]. Recently, satellite observations of tropospheric CHOCHO vertical column densities (VCDs) became available from the SCanning Imaging Absorption SpectroMeter for Atmospheric CartograpHY (SCIAMACHY) [Vrekoussis et al., 2009; Wittrock et al., 2006] and Global Ozone Monitoring Experiment-2 (GOME-2) [Vrekoussis et al., 2010]. A number of CHOCHO hot spots were identified in these observations, such as over the tropical ocean and eastern China. CHOCHO abundance over China was found to have increased from 2003 to 20097 [Vrekoussis et al., 2009 and unpublished data].

Global modeling studies of CHOCHO [Fu et al., 2008; Myriokefalitakis et al., 2008; Stavrakou et al., 2009] have consistently shown a substantial underestimation of the columns of CHOCHO over China, when compared to satellite observations. In contrast, much better agreement was found over the high CHOCHO region of the southeastern U.S., driven by biogenic isoprene emissions [e.g., Fu et al., 2008]. Model discrepancies have also been found over tropical regions and the causes are still under

[4] This chapter is an extension of "Exploring the missing source of glyoxal (CHOCHO) over China," submitted to Geophysical Research Letters in 2012. Co-authors are Yuhang Wang, Mihalis Vrekoussis, Andreas Richter, Folkard Wittrock, John P. Burrows, Min Shao, Chih-Chung Chang, Shaw-Chen Liu, Hongli Wang, and Changhong Chen.

discussion. Previous studies over China [e.g., Zhang et al., 2009] highlighted the complexity and large uncertainties in the emissions of reactive VOCs, many of which are precursors of CHOCHO. In this work, we explore the missing source of CHOCHO over China by comparing CHOCHO VCDs from SCIAMACHY and those calculated by a Regional chEmical trAnsport Model (REAM).

5.2 Data and Model descriptionsCHOCHO VCDs

The differential optical absorption spectroscopy (DOAS) technique is applied to observations of the upwelling radiation leaving the top of the atmosphere and measured by SCIAMACHY [Burrows et al., 1995, Bovennsmann et al., 1999, and references therein] to retrieve CHOCHO VCD in the spectral window of 435-457 nm. The retrieval error comprises an estimated absolute error of CHOCHO VCDs of 2×10^{14} molecules cm-2 and the relative error is about 30%. For details of the retrieval processes, please refer to Vrekoussis et al. [2009].

5.2.2 In situ VOC measurements

VOC observations at three sites, in Beijing (39.99 °N, 116.31 °E, August 2007), Shanghai (31.17 °N, 121.43 °E, July 2010) and the Back Garden site (23.5 °N, 113.03 °E, July 2006) over the Pearl River Delta (PRD), are used in model evaluation. The first two are urban sites on the roof top of a building (~ 20 m above ground). The last one (~10 m above ground) is a remote site 60 km NW of Guangzhou. C_2-C_9 (or C_{12}) VOC species were measured by online GC-FID/PID systems. The detection limits are 10-100 pptv and the estimated uncertainty is 5-10%. More details are given in the supplement materials.

5.2.3 REAM-3D model

The 3-D REAM model has been applied over North America, East Asia and the polar regions [e.g., Choi et al., 2005; Wang et al., 2007; Choi et al., 2008ab; Zhao et al., 2009ab; Zhao and Wang, 2009; Zhao et al., 2010; Yang et al., 2011]. The model has a horizontal resolution of 70 km with 21 vertical layers in the troposphere. Transport is driven by WRF assimilated meteorological fields constrained by the NCEP reanalysis products. Most meteorological inputs are archived every 30 min except those related to convective transport and lightning parameterizations, which are archived every 5 min. Chemical initial and boundary conditions for chemical tracers in REAM are obtained from the global simulation for the same period using the GEOS-CHEM model (v7-03-06) driven by GEOS-4 assimilated meteorological fields [Bey et al., 2001]. The chemistry of REAM is extended from that of standard GEOS-Chem by inclusion of aromatics, acetylene, and ethane, which are major precursors for CHOCHO. Biogenic emissions of isoprene and other species are based on MEGAN (v2.1) [Guenther et al., 2006]. The aAnthropogenic VOC emission inventory by Zhang et al. [2009] is used. The biomass burning emissions are obtained from the Global Fire Emissions Database, Version 2 (GFEDv2.1; available at http://daac.ornl.gov/). The precursor emissions and chemistry for CHOCHO in this work are generally consistent with previous modeling studies [e.g. Fu et al., 2008]. The aerosol sink of CHOCHO is not considered, and we note that this additional sink of CHOCHO would only make the magnitude of the missing source of CHOCHO even larger. The model simulated CHOCHO VCDs are sampled at the SCIAMACHY overpass time (10:00am local time) and averaged over a month to compare with the satellite monthly average VCDs.

We chose to conduct inverse modeling of SCIAMACY CHOCHO observations for August 2007 in part because of the full suite of observation data available and well-characterized photochemical simulations during the CAREBeijing-2007 Experiment [Liu et al., 2010; 2012]. The influence of biomass burning sources is much reduced smaller in August than in July. Simulations were also conducted for July of 2006 and 2010 to compare model simulated VOC concentrations to in situ observations in PRD and Shanghai, respectively.

5.3 Results and discussions

5.3.1 Spatial distribution of glyoxal underestimates

We determine the spatial distribution of CHOCHO VCD underestimates by calculating the difference of SCIAMACHY observed and model simulated CHOCHO VCDs from SCIAMACHY observations. Figure 5.1a shows the spatial distribution of ΔC_{CHOCHO} over China in August 2007. While the spatial pattern of ΔC_{CHOCHO} is generally consistent with the previous global modeling results [e.g. Fu et al., 2008], the finer spatial resolution of REAM allows further and more detailed scrutiny of the spatial distribution features of the sources, which are being underestimated. High ΔC_{CHOCHO} values ($>3.5\times10^{14}$ molecules cm^{-2}) much larger than observational errors are identified over the East China Plain, the Pearl River Delta, the Northeast Plain, as well as the Sichuan Basin.

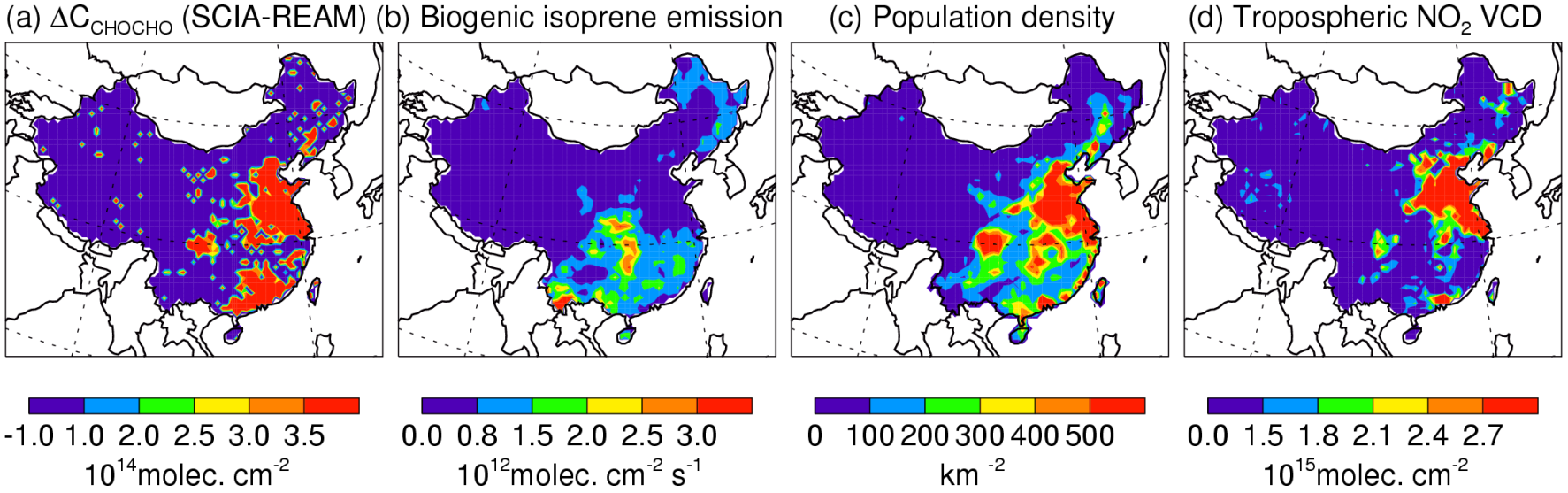

Figure 5.1 (a) Model underestimation of monthly average glyoxal VCDs from SCIAMACHY, (b) monthly average biogenic isoprene emissions, (b) population density, and (4) monthly average tropospheric VCDs of NO_2 from OMI in August 2007.

In order to assess potential origins of the ΔC_{CHOCHO} the spatial patterns of ΔC_{CHOCHO} from the various emission sources over China are analyzed. Previous studies have proposed that significant and quite uncertain biomass burning emissions may result from large-scale agricultural fires over East China Plain in June [Fu et al., 2007]. ATSR fire hotspot map (http://wfaa-dat.esrin.esa.int/) shows that biomass burning is insignificant and restricted over to few areas in August (see Supporting Information). Biomass burning is therefore not likely to be responsible for the widespread source underestimation of CHOCHO in August, shown in Figure 5.1a. Further, ΔC_{CHOCHO} is only significant over regions having low biogenic isoprene emissions (Figure 5.1b) and high anthropogenic emissions, and associated with high population densities (Figure 5.1c) and satellite vertical columns of NO_2 (Figure 5.1d), the latter of which is an indicator of fossil fuel combustion emissions. This implies that the unidentified source is likely to be anthropogenic in nature and not biogenic. Previous global modeling studies also showed that CHOCHO sources from biogenic isoprene oxidation at northern mid-latitudes are reasonably represented in the models [e.g. Fu et al., 2008]. Figure B.2 (Supporting Information) shows the distribution of CHOCHO VCD resulting from the emissions of isoprene, ARO1 (benzene, toluene, ethylbenzene), ARO2 (xylenes and trimethylbenzenes), and acetylene and minor contributions from alkenes and monoterpenes. Comparing Figure B.2 to Figure 5.1, it is clear that the contributions by aromatics (ARO1 and ARO2) are most likely underestimated. Neither isoprene nor acetylene derived CHOCHO distributions resemble that of ΔC_{CHOCHO}. Subsequently inverse modeling has been used in this study to quantify the underestimation of the aromatics emissions.

5.3.2 Top-down inversion

Following previous inverse modeling studies of VOC emissions using satellite column observations [Fu et al., 2007; Shim et al., 2005], we assume a linearized relationship between glyxoal VCDs (C_{CHOCHO}) and the precursor emissions (E_i):

$$C_{CHOCHO}^{observed} \approx \sum_{i=1}^{n} E_i \times \frac{\partial C_{CHOCHO}}{\partial E_i} \quad (1)$$

The relationship is valid only for precursors that are short-lived, i.e., isoprene and fast-reacting aromatics. We first remove the contribution to the regional background by the long-lived acetylene, which cannot explain the ΔC_{CHOCHO} distribution in Figure 5.1. Previous studies suggested acetylene emissions are reasonable over the region [e.g., Carmichael et al., 2003]. We also remove the minor contributions by alkenes and monoterpenes in the inversion since these small contributions cannot be estimated by inverse modeling when the difference between the model and observations is much larger. The contribution by these sources is shown in Figure B.2. We obtain:

$$\Delta E_i \approx \frac{\Delta C'_{CHOCHO}}{\partial C_{CHOCHO} / \partial E_i} \quad (2)$$

where $\Delta C'_{CHOCHO}$ denotes the difference between observed and simulated CHOCHO VCDs after removing the contributions by acetylene, alkenes, and monoterpenes.

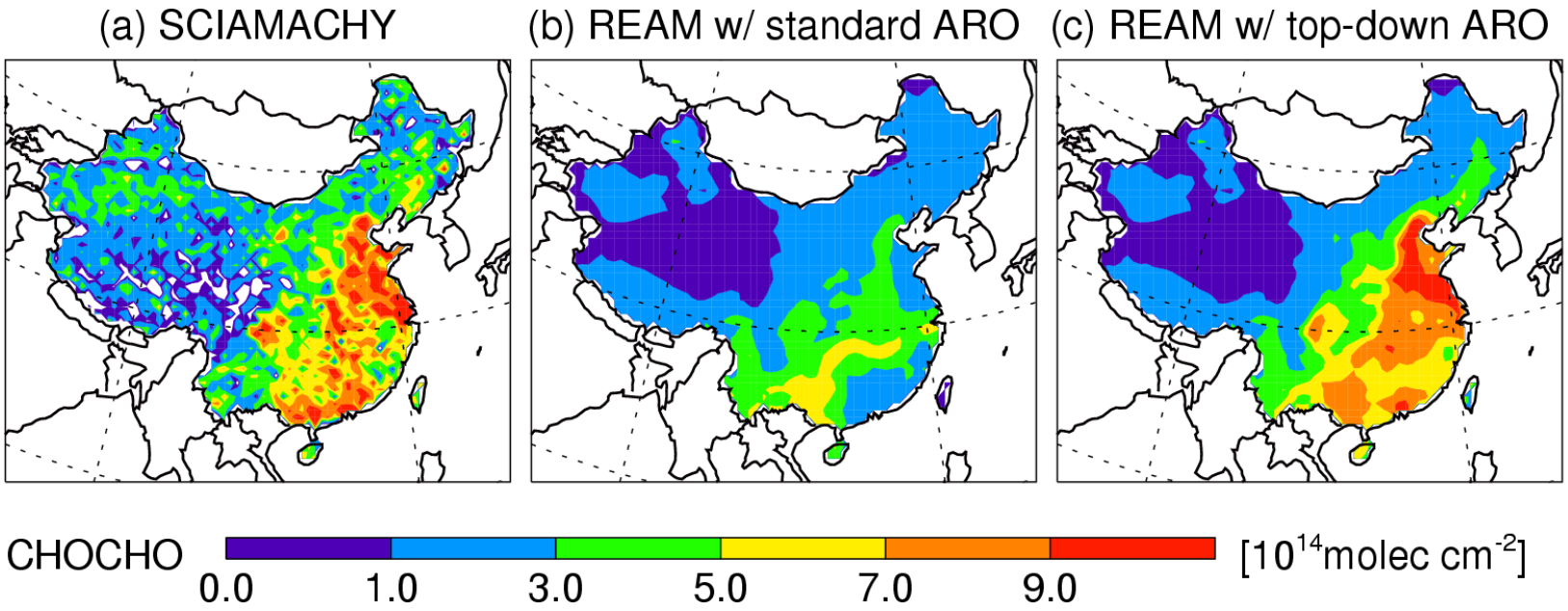

Figure 5.2 (a) Monthly average glyoxal VCDs in August 2007 from SCIAMACHY, (b) simulated monthly average glyoxal VCDs with standard VOC emissions, (c) simulated monthly average glyoxal VCDs with top-down estimates of aromatic VOC emissions.

A general approach of inverse modeling is to assume that the spatial distributions of the sources are correct and that only the emission magnitudes are adjusted to improve model simulations of the observations [e.g., Shim et al., 2005]. Applying this approach, in which the state vectors of the inversion are the emissions of ARO1, ARO2, and isoprene, we found poor agreement between the simulated and observed distributions of CHOCHO after the inversion. The result is not surprising given the large spatial difference between observed CHOCHO and simulated contributions from precursor emissions (Figures 5.1 and B2).

We apply a different approach, in which we derive the emission adjustment for each grid, such that the spatial variability of emission adjustments can be examined. Since satellite CHOCHO VCD observations are not precursor specific, we make use of surface observations of VOCs from Beijing, Shanghai, and PRD sites to further evaluate the validity of the inversion results. We conduct 4 sets of top-down inversion for the emissions of ARO1+ARO2, ARO1 only, ARO2 only, and isoprene only (Figure B.3 in the Supporting information). In the case of isoprene only, we need to increase isoprene emissions by a factor of 6 - 20 over eastern China (Figure B.3), where estimated biogenic emissions are low (Figure 5.1). Comparison with in situ isoprene measurements at the three surface sites using the standard model shows that the ratios of simulated to observed isoprene concentrations are close to or somewhat higher than 1, indicating that the large increases suggested by top-down inversion are unrealistic. Similarly, top-down inversion of ARO1 or ARO2 only leads to large overestimates of ARO2 or ARO1, respectively, at the surface sites.

The best comparison with surface measurements is obtained when both ARO1 and ARO2 are constrained by top-down inversion (Figure 5.3). Top-down inversion increases ARO1 and ARO2 concentrations by a factor of 4 - 10, bringing the model results in much closer agreement with the observations, although simulated concentrations are still a factor of 2 - 3 lower at Shanghai and PRD sites. This top-town inversion significantly increases simulated CHOCHO VCDs in much better agreement with SCIAMACHY observations than the standard model (Figure 5.2).

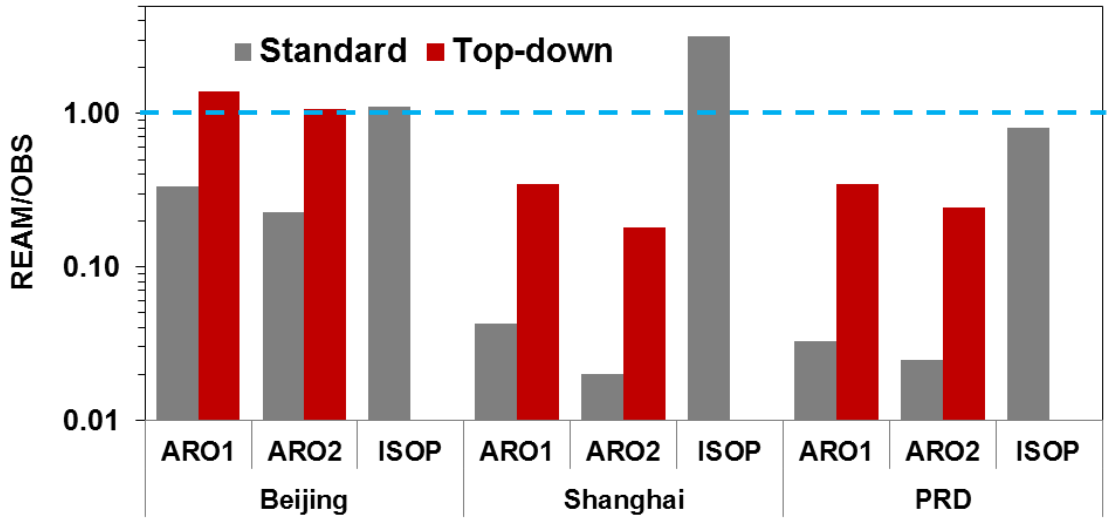

Figure 5.3 Ratios of simulated to observed VOC concentrations at three surface sites. Results for aromatics include the simulations with standard (gray) and top-down (red) emissions, respectively.

Top-down inversion suggests large increases in the emissions of aromatics over eastern China. The increase is a factor of 4 - 8 for central eastern China, and is a factor of > 10 in Yangtze River Delta (YRD) and southern China surrounding PRD. The latter two regions are known for spear-heading the economic developments in China. We now consider the results presented here in light of the uncertainties of the top-down inversion. The uncertainty of ΔC_{CHOCHO} comes mainly from SCIAMACHY retrieval (30%) since

simulated CHOCHO VCDs are too low in the standard model (Figure 5.2). If we assume that the uncertainty of $\partial C_{CHOCHO} / \partial E$ is 100% for ARO1 and ARO2 and the retrieval and model errors are independent, the top-down emission uncertainty is 104%, considerably less than the estimates of emission changes.

5.4 Implications

Large aromatic VOC abundance over polluted regions in China appears to be the major contributor to the elevated CHOCHO concentrations observed over these regions by the satellite. This is quite different from the eastern U.S., where concentrations of aromatics are much lower and isoprene is a major source of CHOCHO (particularly over the Southeast). Our results demonstrate that satellite observations of CHOCHO provide the critical information to better characterize the VOC emissions of aromatics over polluted regions, where information of domestic VOC emission sources are incomplete.

The results from the top-down inversion imply a factor of 5 increase of total aromatics emission over China, i.e. increasing from 2.4 Tg yr^{-1} in the standard inventory to 13.4 Tg yr^{-1}. The resulting increase of the total VOC emission over China by 47% (from 23.2 Tg yr^{-1} to 34.2 Tg yr^{-1}) is still within the 168% uncertainty of the total VOC emission estimated by Zhang et al. [2009]. The underestimates of aromatics at Shanghai and PRD after inversion (although much reduced compared to the standard model) and the exclusion of CHOCHO loss to aerosols in the model indicate that the emissions of aromatics from China after inversion are probably a lower limit and in real emissions are even larger than these top-down estimates.

The large uncertainty of reactive VOC emissions in China has been noted by some recent regional modeling studies [e.g. Chen et al., 2010; Sarwar et al., 2011; Yang

et al., 2011]. The inaccurate and incomplete information for domestic anthropogenic emission sources, e.g. their source profiles, emission factors and source activities, is a major source of uncertainty in emission inventories [Chen et al., 2010]. The specific causes for the systematic bias of VOC emission profiles (particularly aromatics) and likely the total VOC emission magnitude merit further investigations. The locations of model emission underestimation appear to suggest that industrial sources are plausible due to either poor characterization of large emission sources such as petrochemical plants or the omission of the large number of small industrial plants in the provincial statistics.

The consequences of such a nationwide large underestimation of aromatic VOC emissions are manifold. Sensitivity simulations show that as a result of the increased aromatics emissions, concentrations of PAN at the surface of those underestimated regions increase by 100%. This is supported by in situ observations over the region [Liu et al., 2010; Zhang et al., 2009]. The O_3 response to VOC changes is much more complex. Aromatic VOCs are the major precursors of oxygenated VOCs, the photolysis of which provides a major primary radical source and increases O_3 production in Beijing [Liu et al., 2012]. Furthermore, aromatic VOC emissions become a large contributor to the organic aerosol budget over the region by secondary organic aerosols (SOA). A recent modeling study by Henze et al. [2008] estimated that the global aromatics emission of 18.8 Tg yr^{-1} produces SOA at a rate of 3.5 Tg yr^{-1}. Applying this SOA production rate, the additional aromatics emissions from China, which result in more than 50% increase of the global aromatics emissions (from 18.8 Tg yr^{-1} to 29.9 Tg yr^{-1}), would lead to over 50% increase of global aromatic SOA production to 5.5 Tg yr^{-1}. The increase

of 2 Tg yr^{-1} SOA production helps explain model underestimation of organic aerosols found previously over China and the outflow region [Fu et al., 2011; Heald et al., 2005].

6. CONCLUSIONS AND FUTURE WORK

6.1 Summary of findings

6.1.1 The complex and uncertain chemical system over polluted regions in China

Aromatic VOCs as an important and uncertain driving factor

Our and previous observations over China have revealed that aromatic VOCs are outstandingly abundant over polluted regions over China. These aromatic compounds not only contribute to O_3 production via generating first generation peroxy radicals, even more importantly and uncertainly, they also produce large amounts of OVOCs which are major primary sources of ROx radicals. These aromatics make the chemical system much more complex than without them (Chapter 3). Especially, the special structure (6 unsaturated carbons in a ring) of aromatic VOCs and their relatively high reactivity make them the most efficient producers of OVOCs. The outstanding glyoxal abundance over China revealed by SCIAMACHY provides direct evidence of the elevated OVOCs over China (Chapter 5). However, it should be noted that many other OVOCs are also expected to be elevated over the same regions as those glyoxal hotspots, since glyoxal is only one of many similar structured OVOCs that are produced during oxidation of unsaturated VOCs, represented by aromatics over China.

Meanwhile, oxidation chemistry of these aromatics is still not well characterized. There are large uncertainties with respect to the yields and molecular structures of those OVOCs derived from aromatics. As a matter of fact, aromatics are a group of VOCs whose chemistry is the most uncertain. As such, the abundance of aromatics thus becomes a key factor that results in the highly complex and uncertain chemistry over

polluted regions over China (Chapter 2 and 3). As such, much remains to be explored to understand the role of aromatics and OVOCs in chemistry over polluted regions.

Importance of aerosol heterogeneous processes

Heterogeneous reactions are another unique aspect of the chemical environment over China. Our quantitative budget analysis suggests that the presence of large amount of aerosols could substantially affect the HO_2 budget and levels (Chapter 3), and contribute a large portion of the observed HONO during daytime (Chapter 4). Such important role of heterogeneous chemistry has not been found over other places simply due to the fact that the aerosol abundance over China is the highest in the world. A similar ramification as that of aromatics due to incomplete knowledge exists for heterogeneous chemistry. A key issue is that the reactive uptake coefficient remains highly uncertain. The chemical composition and physical properties of aerosols over China are also not well understood yet. Meanwhile, other heterogeneous processes other than HONO formation and HO_2 uptake, such as N_2O_5 uptake, may also be quite important. More future work is needed to further understand the role of heterogeneous chemistry in determining chemical budgets over China. Experimental studies targeting aerosols over China needed to develop mechanistic understanding of those heterogeneous processes.

6.1.2 Uncertain VOC emission inventories over China

Emission data is a critical input for CTMs. Although emissions of some species have been examined more carefully and a reasonable agreement between bottom-up and top-down estimates have been reached, our results in Chapter 5 suggest that VOC emissions over China remain highly uncertain. Given the paramount role of VOCs in the

chemical system (Chapter 2 and Chapter 3), a 3-D CTM with incorrect VOC emissions would simulate unrealistic chemical processes that lead to incorrect interpretation of the model results or observations.

Our results in Chapter 5 suggest that current VOC emission inventory over China need reassessed and revised. The process of compiling emission inventories need improvement, especially in terms of better characterizing domestic emission sources. Meanwhile, satellite observations can provide valuable additional constraint for the emission estimates and should be utilized whenever possible given the challenges and time-consuming efforts required in improving bottom-up emission estimates.

6.1.3 Implications for O_3 simulations over China

O_3 simulation exercises have been carried out extensively. Our results suggest that interpretation of these model results need to be reassessed given the large uncertainties in both chemistry and emissions in these models. The consequence of incorrect emissions and chemistry on chemical budgets could be either straightforward or really complex, depending on what species is concerned. The highly non-linear dependence of O_3 on precursor emissions and the important role of transport on O_3 concentrations make O_3 simulation results difficult to interpret. However, most previous modeling work has been using observed O_3 as a reference to evaluate and calibrate model performance. This is wrong. Observations and modeling studies of other species, such as PAN, which is more sensitive to emission input and chemistry, are needed to reassess the ability of current models in representing the chemical environment over China.

6.1.4 Implications for pollution control strategies

The photochemical pollution over China has been seen before over other developed countries, such as the U.S. As such, there appears to be a convenient way to tackle the problem – to learn from the history. As a matter of fact, the problems and challenges in pollution control found over China in this and previous studies occurred in history as well. For example, VOC emissions in the U.S. were once very uncertain as well, before significant efforts were made to get a better understanding. Experiences, policies, and methodologies in developing a precise emission inventory from the U.S. are the most valuable resources for current efforts over China.

On the other hand, there are also important unique features of air pollution over China. For example, the large concentration of population and emissions due to the clustering of cities and fast developing regions are unprecedented in history. These unique and challenging situations may have substantial impact on regional chemical environment, and should also be taken into account during formulation of pollution control strategies.

6.2 Recommendations for future work

6.2.1 Understand the emission-chemistry interactions

In the present work, the chemical system and the emissions have been isolated and decoupled, before each of them is examined. As a next step, research efforts should be made to couple these two processes, and better understand their interactions. In recognition of the many uncertain factors involved in a 3-D model setting, an improved observation-based 1-D model with emissions taken into account could be utilized to

examine the interactions of emissions and chemistry. Scientific questions that could be addressed include: (1) to understand the factors leading to the elevated NO concentrations observed in Beijing, and the role of chemistry and emissions in determining the ratio of NO/NO_2 and NO_y partitioning; (2) to identify the factors that contribute to define the diurnal profiles of NO_x and VOCs; (3) to examine the sensitivity of chemical vertical profiles to emissions and chemistry.

6.2.2 Further constrain VOC emissions using satellite observations

In this work, emissions of aromatics are examined due to the unique chemistry of glyoxal. As noted earlier, the emissions of other VOC species are likely to be equally uncertain and need to be examined in future too. Other satellite observations such as formaldehyde could be used in conjunction of glyoxal to constrain emissions of other species. Meanwhile, aircraft and ground VOC measurements over different regions over China could be utilized to develop an observation-based regional perspective of the VOC emissions. Given the large uncertainties in spatial distributions of VOC emissions, likely caused by using surrogate data to allocate emissions, efforts could be made to 'redistribute' VOC emissions based on information of large VOC emission sources such as locations of large point sources, e.g. chemical plants, and area sources, e.g. large industrial zones, could be used to develop a more realistic spatial distribution of those emissions.

6.2.3 Understand the role of transport processes in defining the regional chemical environment

Although the present work has been focusing on two processes that determine the chemical environment over China, i.e. emissions and chemistry, vertical and horizontal transport are critical processes that contribute to define the spatial distribution of air pollutants and the regional chemical environment. The roles of the unique topography over eastern China and the highly concentrated emission over the region in contributing to the large scale abundance of air pollutants are worth examination though detailed modeling analysis of transport processes over the region. Such unique topographical condition could also help define the vertical distribution of air pollutants. The ability of current meteorological models in resolving transport over such a region needs to be assessed.

APPENDIX A: AUXILURY MATERIALS FOR CHAPTER 2

The auxiliary materials include: 1) more detailed descriptions of instruments and experimental methods; 2) more detailed descriptions of the 1-D REAM model the meteorological simulations in the 1-D version of REAM model; 3) estimation of model errors; 4) the aromatics oxidation mechanism used in the 1-D REAM model; 5) NMHC model input; 6) comparison of simulated PAN with observations; 7) Average percentage contributions of VOCs to PA radical formation; 8) 3 tables and 2 additional figures (Figure A.1 and A.2) mentioned in the text.

A.1 Descriptions of instruments and experimental methods

A.1.1 O_3 and CO measurements

O_3 and CO were measured with commercial instruments (ECOTECH, EC9810 and EC9830). The EC9810 Ozone Analyzer combines microprocessor control with ultraviolet (UV) photometry to measure O_3 with a detection limit of 0.5 ppbv. The EC9830 series of Carbon Monoxide analyzers use NDIR gas filter correlation photometry to measure Carbon Monoxide (CO). Zero signals were routinely measured every 2 hours by supplying dry purified air into the sample line. We note that as water vapor interferes the CO analyzer, using dry air will give lower baseline values, thus higher CO concentrations. The uncertainties for these measurements are estimated to be 5% (1 standard deviation, and so for all other uncertainties).

A.1.2 NO and NO_y measurements

NO mixing ratios were measured with a custom chemiluminescence detector. The instrument was calibrated periodically (2–4 hours) by a standard addition of a known amount of nitric oxide. Background levels were obtained periodically (30 minutes) by switching the sampled flow through a pre-reactor. NO_y levels were measured by use of a molybdenum converter operated at 300℃. The sample flow to the NO detector was periodically switched between ambient and the converter by a three way Teflon valve. NO_y conversion levels were estimated to be greater than 97% for NO_2. The conversion efficiency for NO_2 were examined before and after the campaign and appears to be quantitative i.e. > 95%. The conversion efficiency for HNO_3 was found to be greater than 85% after the mission. We did not look at anything in Beijing during the measurements, as we didn't have the ability to do so. High conversion efficiency for PAN (greater than 95%) can be expected because PAN will decompose to NO_2 readily at high temperature. The efficiency for NO should be comparable with NO_2, too. Organic nitrates were probably close to 100% converted. The uncertainties for NO and NO_y measurements are estimated to be 5% and 10%, respectively.

A.1.3 PAN measurements

PAN was measured using a chemical ionization mass spectrometer (CIMS). The instrument was calibrated periodically with a photolytic PAN source and the background response of the instrument was determined by periodically scrubbing sampled air through hot stainless steel tubing (200 ^{o}C). The sensitivity of the instrument was found to decrease at high NO_x levels. High levels of NO can lead to a decrease in sensitivity to the CIMS PAN measurements. For the conditions in Beijing, 10 ppbv of NO reduced the

PAN sensitivity by 10% with higher levels decreasing the sensitivity further. NO levels above 10 ppbv were observed 20% of the time but only at night. Consequently, there is essentially no correction for the impact of NO during the day on PAN sensitivity. The measurement uncertainty of PAN at night during high levels of variable NO is larger than during the day. Detection limit for PAN is 7 pptv for 1 second integration period and a signal to noise ratio of 3. The uncertainties for PAN measurements are estimated to be 10%.

A.1.4 HONO measurements

HONO was measured with a liquid coil scrubbing/UV–vis instrument. Briefly, gaseous HONO was trapped quantitatively in a 10-turn coil sampler using 1mm phosphate buffer. The scrubbing solution was then derivatized with sulfanilamine (SA)/N-(1-naphtyl)-ethylendiamine (NED), subsequently analyzed using high-performance liquid chromatography (HPLC), and detected by UV-vis absorption.

Interferences during sampling were studied in our laboratory in Rome and directly at Beijing using sodium carbonate denuders. We used the denuder respectively in front of the Teflon tube and before the trap coils. The denuder in front of Teflon tube was used to study the possible formation of HONO from NO_2 and humidity on the tubing walls. While, the denuder before the inlet traps was used to study the nitrite formation in the water solution due to: $NO_3^- + SO_3 \rightarrow NO_2^- + SO_4^{2-}$. Under summer conditions at Beijing we observed interferences on the order of 2–9% of the observed HONO mixing ratio. The inlet tube was 70 cm and the residence time of the air in the tube was less than 2 sec. The

detection limit of the HONO instrument is less than 0.8 pptv. The uncertainty for HONO measurements is estimated to be 10%.

A.1.5 VOC measurements

C_3-C_9 NMHCs were continuously measured with 30 minute time resolution, using a combination of two online GC-FID/PID systems (Syntech Spectra GC-FID/PID GC955 series 600/ 800 VOC analyzer), one for the C_3–C_5 NMHCs, using a gas chromatograph with pre-concentration on Carbosieves SIII at 5 ^{o}C, followed by thermal desorption and separation on a capillary film column and a capillary PLOT column, and quantification by a photo ionization detector (PID) and a flame ionization detector (FID). The other system is for C_6–C_9 NMHCs analysis; air samples are pre-concentrated on Tenax GR at normal temperature, thermal desorbed, separated on an ATTM-1 column, and detected by a PID. For each analysis, an air sample with a volume of 250mL was sampled. Calibration was performed before and after the campaign by using a gas standard containing 39 target species with mixing ratios of 1ppm in nitrogen, prepared by the gravimetric method (Spectra gases, Restek Corporation, USA). The detection limits are estimated to be 10 to 90 pptv, and the uncertainty is estimated to be 5%.

Another Automated GC/MS/FID system constructed of pre-concentrator with Varian 3800 GC and Saturn 2200 MS was also deployed to measure VOCs. On each day two samples were collected and measured (8:00-9:00 and 13:00-14:00). To encompass VOCs of a wide range of volatility within each analysis, the system uses dual-columns and dual-detectors to simultaneously analyze both low and high-boiling compounds with each injection. The PLOT column connected to a FID was responsible for separation and

detection of C2–C4 compounds, and the DB-1 column was connected to the MS for separation and detection of MTBE and C4–C10 compounds. Each aliquot of 190 ml from the canisters was drawn to the cryogenic trap packed with fine glass beads cooled at –170 ℃ for pre-concentration. During injection, the trap was resistively heated up to 80 ℃ within seconds, and a stream of high purity He flushed the trapped VOCs onto the columns. The oven temperature was initially held at –50 ℃ for 3.1 min, then ramped to –10 ℃ at 20 ℃/min, to 120 ℃ at 5 ℃/min, to 180 ℃ at 20 ℃/min, and held at 180 ℃ for 21.5 min. The precision of the system was examined by repeatedly injecting a standard mixture made from Scott Marrin Company. In general, the precision for the C2–C10 NMHCs were usually below 3%. Linearity was tested by trapping a series of the same standard mixture of various concentrations (0.2-30ppbv). Most compounds exhibited good linearity with RSD of calibration response factors for measured species bellow than 10%.

OVOC compounds were measured using a newly developed PFPH-GC/MS method. 12 types of gaseous carbonyls, including formaldehyde, acetaldehyde, propanal, butanal, heptanal, octanal, acrolein, 2-furfural, benzaldehyde, p-tolualdehyde, glyoxal, and methylglyoxal, were collected within 3-h sampling period onto an adsorbent (Tenax TA) coated with pentafluorophenyl hydrazine (PFPH) followed by thermal desorption and gas chromatographic (GC) analysis of the PFPH derivatives with mass spectrometric (MS) detection (Agilent, GC/MS, 6890/5973N). All of the tested carbonyls are shown to have method detection limits (MDLs) of sub-nanomoles per sampling tube, corresponding to air concentrations of < 0.3 ppbv for a sampled volume of 24 L. These

limits are 2-12 times lower than those that can be obtained using the DNPH/HPLC method. The uncertainty for OVOC measurements is estimated to be 10%.

A.2 Additional descriptions of the 1-D REAM model

A.2.1 Meteorological simulations in the 1-D version of REAM model

Meteorological fields are assimilated for the 3-D REAM domain using the Weather Research and Forecasting (WRF) model (v3.1) constrained by the NCEP reanalysis products (NNRP), with a horizontal resolution of 70km × 70 km and 35 vertical layers from the surface to 10 hPa. The meteorological fields (not including horizontal wind fields) over Beijing are archived every 30 minutes for 1-D REAM model simulations.

A.2.2 Estimation of Model errors

The errors associated to the model can be estimated. The uncertainty associated with chemical mechanism is estimated to be less than 10% based on a sensitivity test, in which using different chemical mechanisms (RACM or REAM) only results in no more than 10% difference of simulated PAN. The uncertainty associated with transport is estimated to be 10% at most, because as stated in the paper, 5 times the modeled diffusion coefficient would only result in less than 10% change of PAN at surface. Taking into account all these aspects, the total error in the model is estimated to be no more than 15% assuming transport and chemistry errors are not correlated and not accounting for the measurement uncertainties of precursors. The latter is hard to compute for a secondary species like PAN.

A.2.3 Oxidation mechanism of aromatics

We adopt the aromatics-oxidation mechanism in the SAPRC-07 chemical mechanism developed for chemical transport models. This mechanism is chosen because comparison between different mechanisms (e.g. SAPRC-99, 07, CB4, CB5, and RACM) and that of REAM indicates that the SAPRC-07 mechanism is the most compatible with REAM and reflects the most recent updates of aromatics chemistry. In Table A.1, we summarize the OH reactions for several key aromatic species, based on which the reactions for the lumped species (ARO1, ARO2) are derived. Among the products, only methylglyoxal (MGLY), glyoxal (GLYX), and biacetyl (BACL)) are shown because they are precursors for acetyl peroxy radical, which is of our interest in this work.

A.2.4 Model VOC input

Individual NMHC compounds were lumped into a number of model species to be used as model input. The mean concentrations for all the individual compounds and their corresponding lumped species are shown in Table A.2. For species only measured at 8:00–9:00 and 13:00–14:00, interpolations were conducted based on ratios between these compounds and other continuously measured compounds with similar lifetimes. Measured concentrations of acetone, acetaldehyde and formaldehyde were used in the model. Other OVOC species that are also important in PAN chemistry but were not measured, such as methyl vinyl ketone, methacrolein, methylglyoxal and biacetyl, are simulated in the model.

A.3 Comparison of simulated and observed PAN

Model simulated and observed hourly PAN mixing ratios are shown in Figure A.2 to show the performance of model to reproduce point-to-point variations. Some peak

values in the afternoon and a number of nighttime values are underestimated by the model, which is consistent with the diurnal profile comparison.

A.4 Average percentage contributions of VOCs to PA radical formation

We calculate the average percentage contributions from major OVOCs to PA radical formation, and from the major NMHC precursors to these OVOCs based on the sensitivity model results. The values are tabulated in Table A.3.

Table A.1 Reactions and rate constants for aromatics species with OH used in SAPRC-07 for deriving the lumped mechanism.

Species	Reactions	k	Mixing ratio (ppbv)	MGLY contribution (%)
Benzene	BENZENE + OH = 0.29 GLYX + Products	1.22E-12	2.2	1
Ethylbenzene	ETHYLBZ + OH = 0.184GLYX + 0.117MGLY + Products	7.00E-12	3.2	4
Toluene	TOLUENE + OH = 0.238 GLY + 0.151 MGLY +Products	5.58E-12	5.9	8
m-Xylene[1]	M-XYLENE + OH = 0.38 MGLY + Products	2.31E-11	2.2	31
o-Xylene	O-XYLENE + OH = 0.238 MGLY + 0.084GLYX + 0.185BACL + Products	1.36E-11	1.7	9
p-Xylene[1]	P-XYLENE + OH = 0.112 MGLY + 0.286GLYX + Products	1.43E-11	2.2	6
1,2,3-Trimethyl Benzene	123TMB + OH = 0.072 MGLY + 0.18GLYX + 0.447BACL+ Products	3.27E-11	0.3	1
1,2,4-Trimethyl Benzene	124TMB + OH = 0.405 MGLY + 0.074GLYX + 0.112BACL+ Products	3.25E-11	0.4	8
1,3,5-Trimethyl Benzene	135TMB + OH = 0.64 MGLY + Products	5.67E-11	0.5	32
ARO1[2]	ARO1 + OH = 0.218 GLYX + 0.138 MGLY + Products	6.15E-12	11.3	15
ARO2[3]	ARO2 + OH = 0.116 GLYX + 0.286 MGLY + 0.104 BACL + Products	2.57E-11	7.3	85

[1] These two species were measured as one species mp-xylene, and we assume the same amount for each in this calculation.
[2] ARO1 includes benzene, ethyl-benzene, and toluene.
[3] ARO2 includes all aromatics other than those included in ARO1.

Table A.2 Average mixing ratios (ppbv) of explicit and lumped NMHCs in the model.

Alkanes		
C2H6[1]	Ethane[2]	3.82
C3H8	**Propane**[3]	**3.73**
ALK4	**isobutane**	**1.85**
	n-butane	**2.14**
	isopentane	**3.50**
	n-pentane	**1.22**
	2,2-dimthylbutane	0.07
	cyclopentane	0.14
	2-methylpentane	0.69
	3-methylpentane	0.50
	n-hexane	**1.40**
	2,4-dimethylpentane	0.06
	methylcyclopentane	0.47
	cyclohexane	0.18
	2-methylhexane	0.21
	2,3-dimethylpentane	0.09
	3-methylhexane	0.25
	2,2,4-trimethylpentane	**0.47**
	n-heptane	**3.47**
	methylcyclohexane	0.14
	2,3,4-trimethylpentane	0.03
	2-methylheptane	0.09
	3-methylheptane	0.09
	n-octane	**0.91**
	n-nonane	0.11
Alkyne		
C2H2	ethyne	5.67

Alkenes		
C2H4	ethene	3.67
PRPE	**Propene**	**1.00**
	trans-2-butene	**0.53**
	1-butene	0.58
	Isobutene	0.37
	cis-2-butene	**0.42**
	3-methyl-1-butene	0.08
	1,3-Butadiene	**0.31**
	1-pentene	**0.57**
	Isoprene	**0.88**
	trans-2-pentene	**0.24**
	cis-2-pentene	0.09
	2-methyl-2-butene	0.18
	Cyclopentene	0.03
	4-methyl-1-pentene	0.00
	2-methyl-1-pentene	0.08
	trans-2-hexene	0.00
	cis-2-hexene	0.04
	alpha-pinene	0.13
Aromatics		
ARO1	**Benzene**	**2.16**
	Toluene	**5.88**
	Styrene	0.12
	Ethylbenzene	**3.25**
ARO2	**m,p-xylene**	**4.30**
	o-xylene	**1.68**
	Isopropylbenzene	0.04
	n-propylbenzene	0.05
	1,3,5-trimethylbenzene	**0.54**
	1,2,4-trimethylbenzene	**0.37**
	1,2,3-trimethylbenzene	**0.32**

[1] Model species are listed to the left and measured species are listed to the right. Lumped model species include multiple measured species.
[2]Species listed in normal font were measured at 8:00-9:00 and 13:00-14:00 each day; the averages of these measurements are shown.
[3]Species listed in bold font were measured continuously each hour; 24-hour averages are shown.

Table A.3 Average percentage contributions from the major OVOCs to PA radicals, and the major NMHC precursors of these OVOCs.

NMHCs	OVOCs	%
aromatics, isoprene, and others	methylglyoxal	50
aromatics	biacetyl	25
alkenes, alkanes, and others	acetaldehyde	20
others		5

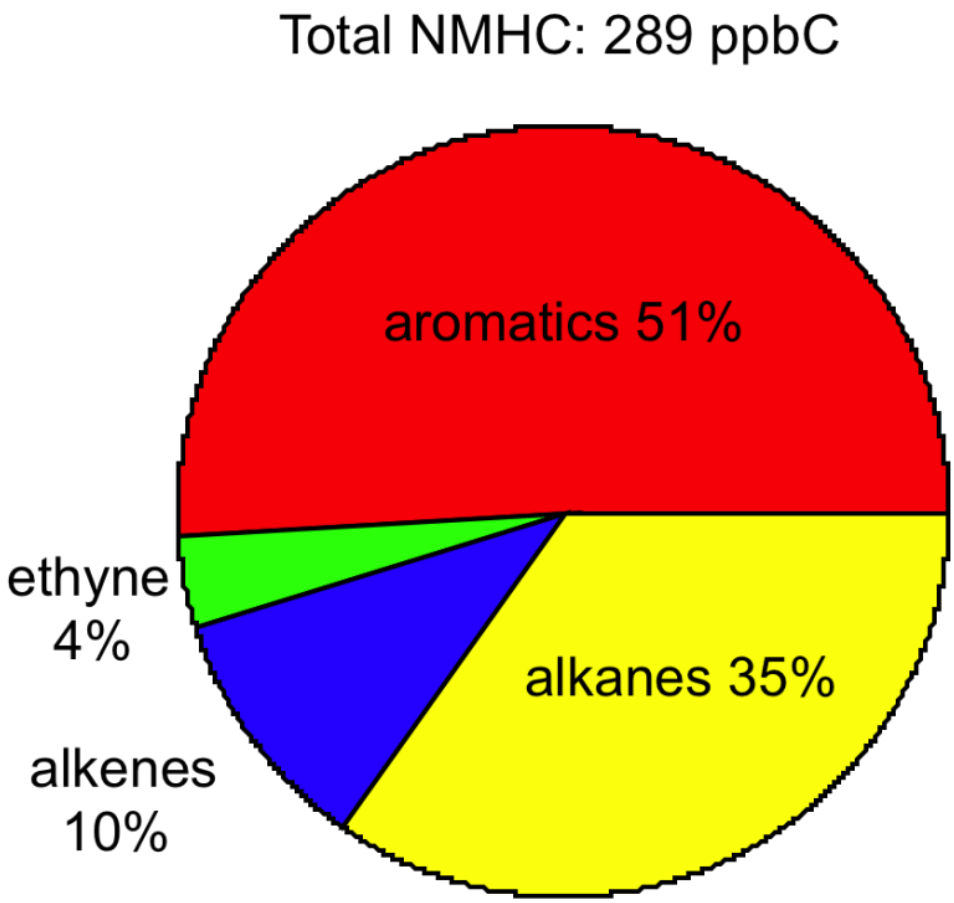

Figure A.1 24-hour average NMHC composition of alkanes, alkenes, and aromatics, and ethyne in terms of carbon during 10-30 August 2007.

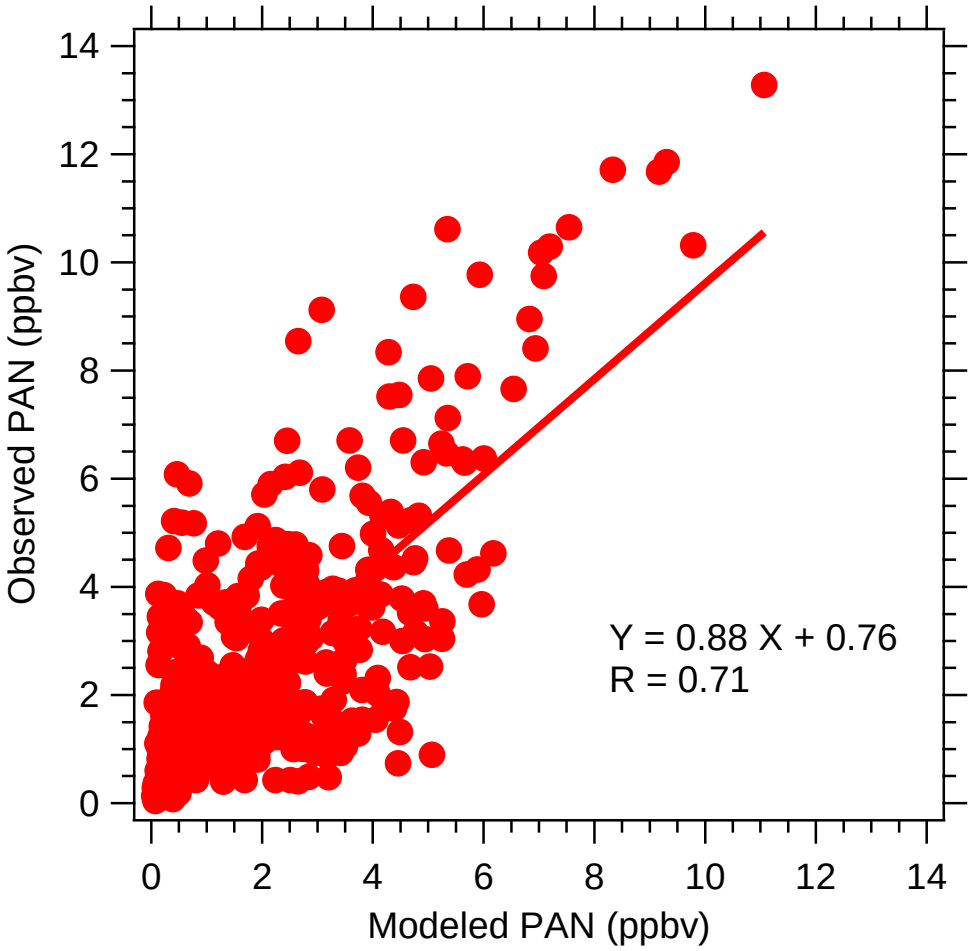

Figure A.2 Hourly observed versus modeled PAN mixing ratios. Data points (less than 10 in total) with important measurement data (such as VOCs and NO) missing (for which averages at the time of the day during the whole campaign were used in the model input) are not included.

APPENDIX B: AUXILURY MATERIALS FOR CHAPTER 5

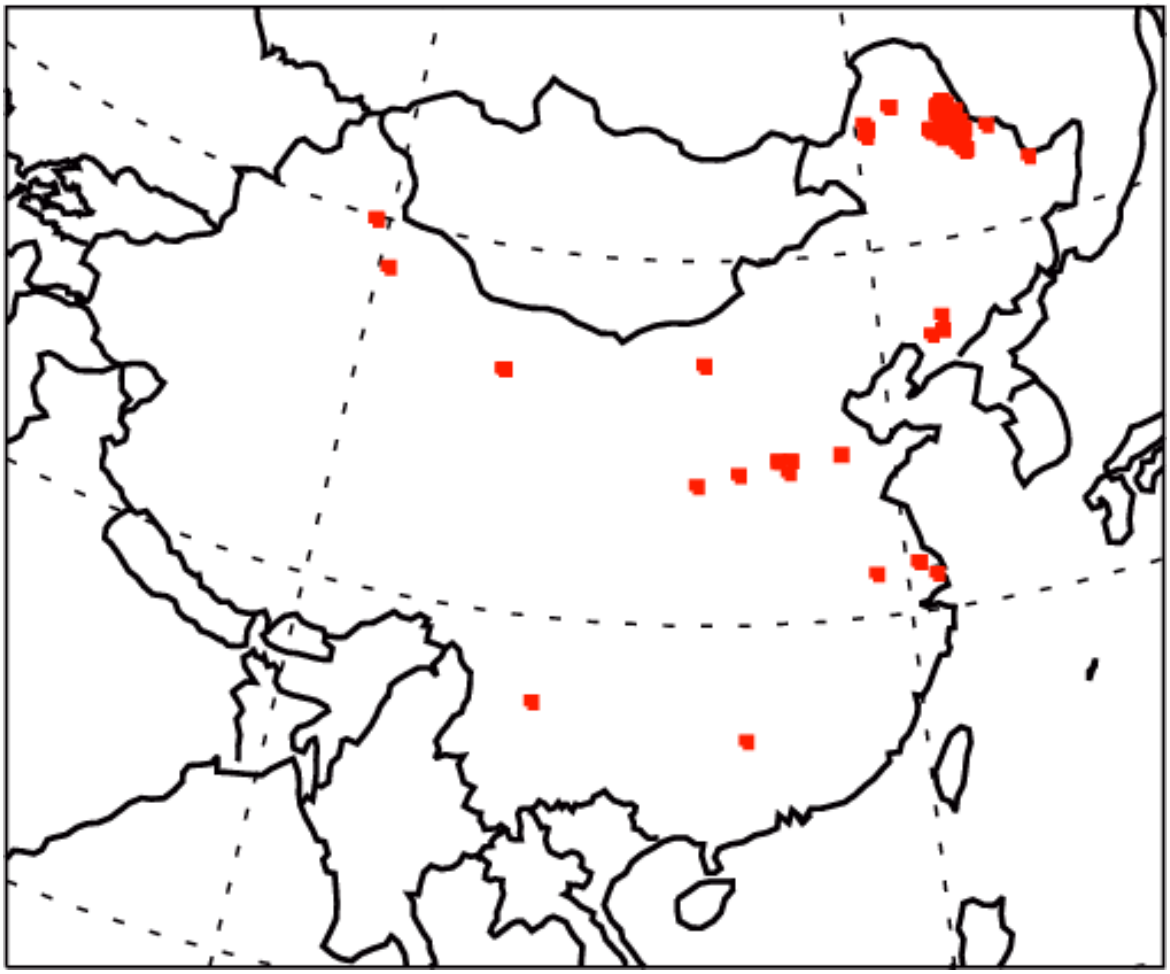

Figure B.1 ATSR fire hotspots in August 2007.

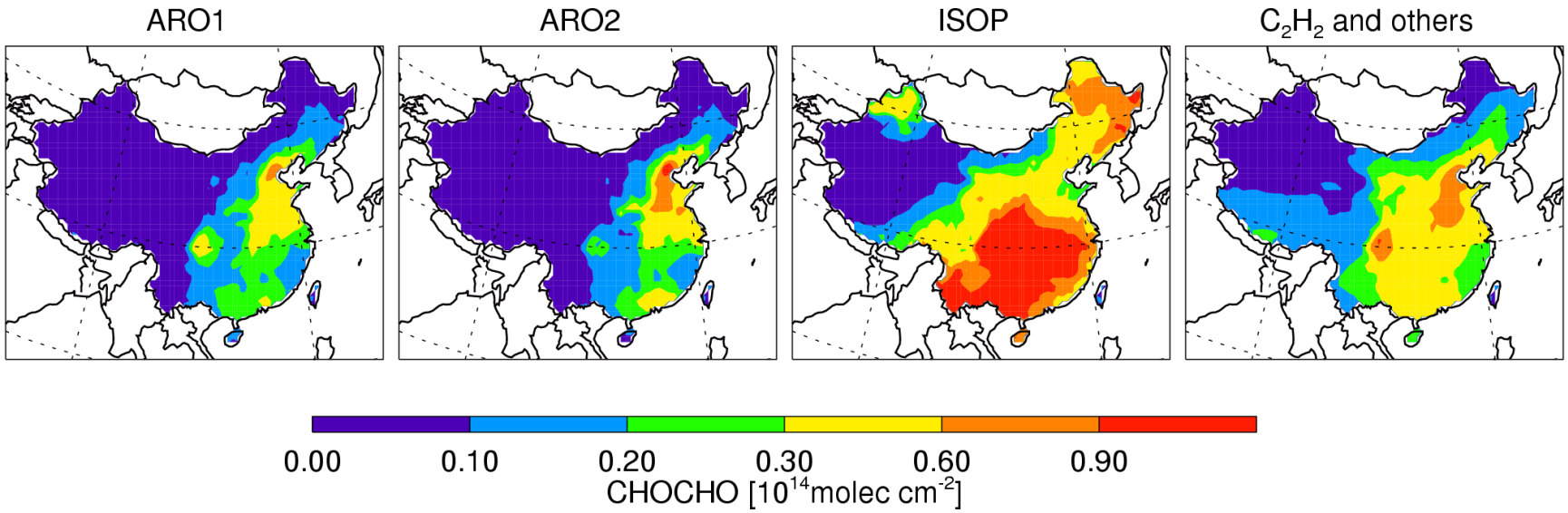

Figure B.2 Contributions to glyoxal VCDs by the emissions of ARO1, AOR2, isoprene, and C_2H_2 (with minor contributions from alkenes and monoterpenes) in the standard model.

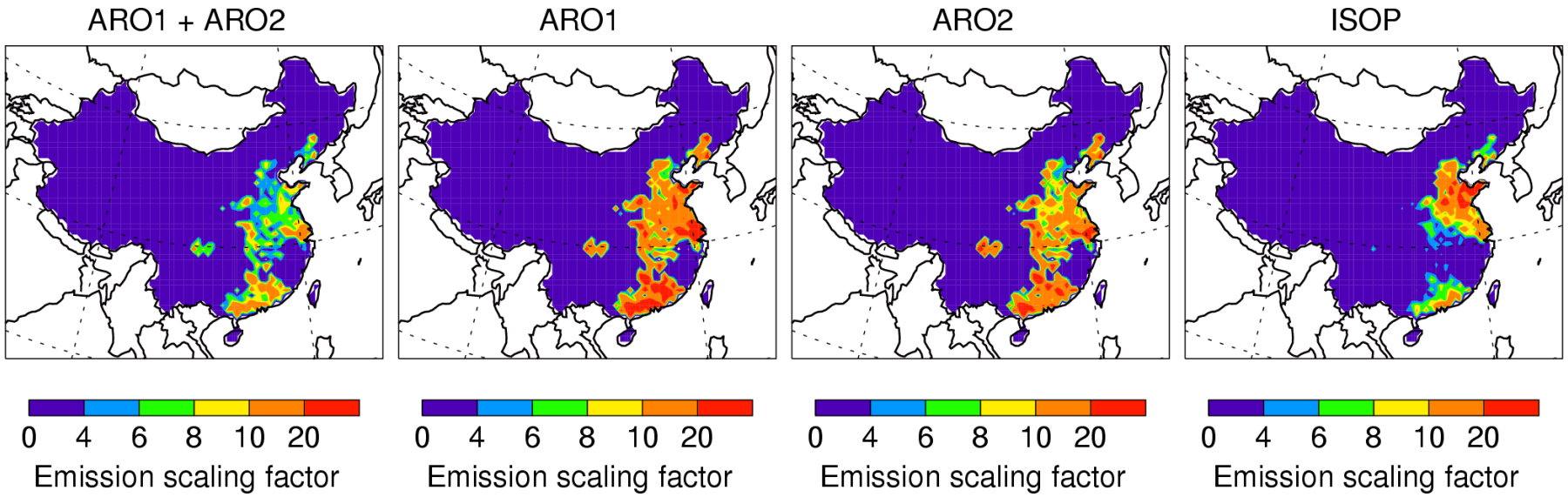

Figure B.3 Top-down scaling factors for the emissions of ARO1+ARO2, ARO1 only, ARO2 only, and isoprene only, respectively.

REFERENCES

Acker, K., D. Moller, W. Wieprecht, F. X. Meixner, B. Bohn, S. Gilge, C. Plass-Dulmer, and H. Berresheim (2006a), Strong daytime production of OH from HNO_2 at a rural mountain site, Geophys. Res. Lett., 33(2), L02809, doi:10.1029/2005GL024643.

Acker, K., et al. (2006b), Nitrous acid in the urban area of Rome, Atmos. Environ., 40(17), 3123-3133.

Alicke, B., U. Platt, and J. Stutz (2002), Impact of nitrous acid photolysis on the total hydroxyl radical budget during the Limitation of Oxidant Production/Pianura Padana Produzione di Ozono study in Milan, J. Geophys. Res.-Atmos., 107(D22).

Alicke, B., A. Geyer, A. Hofzumahaus, F. Holland, S. Konrad, H. W. Patz, J. Schafer, J. Stutz, A. Volz-Thomas, and U. Platt (2003), OH formation by HONO photolysis during the BERLIOZ experiment, J. Geophys. Res.-Atmos., 108(D4).

Amoroso, A., H. J. Beine, G. Esposito, C. Perrino, M. Catrambone, and I. Allegrini (2008), Seasonal differences in atmospheric nitrous acid near Mediterranean urban areas, Water Air Soil Pollut., 188(1-4), 81-92.

An, J. L., W. Zhang, and Y. Qu (2009), Impacts of a strong cold front on concentrations of HONO, HCHO, O_3, and NO_2 in the heavy traffic urban area of Beijing, Atmos. Environ., 43(22-23), 3454-3459.

Amoroso, A., H. J. Beine, R. Sparapani, M. Nardino, and I. Allegrini (2006), Observation of coinciding arctic boundary layer ozone depletion and snow surface emissions of nitrous acid, Atmos. Environ., 40(11), 1949-1956.

Bari, A., V. Ferraro, L. R. Wilson, D. Luttinger, and L. Husain (2003), Measurements of gaseous HONO, HNO_3,SO_2, HCl, NH_3, particulate sulfate and PM2.5 in New York, NY, Atmos. Environ., 37(20), 2825-2835.

Bey, I., D. J. Jacob, R. M. Yantosca, J. A. Logan, B. D. Field, A. M. Fiore, Q. B. Li, H. G. Y. Liu, L. J. Mickley, and M. G. Schultz (2001), Global modeling of tropospheric chemistry with assimilated meteorology: Model description and evaluation, J. Geophys. Res.-Atmos., 106(D19), 23073-23095.

Bloss, C., V. Wagner, A. Bonzanini, M. E. Jenkin, K. Wirtz, M. Martin-Reviejo, and M. J. Pilling (2005), Evaluation of detailed aromatic mechanisms (MCMv3 and MCMv3.1) against environmental chamber data, Atmos. Chem. Phys., 5, 623-639.

Bovensmann, H., J. P. Burrows, M. Buchwitz, J. Frerick, S. Noel, V. V. Rozanov, K. V. Chance, and A. P. H. Goede (1999), SCIAMACHY: Mission objectives and measurement modes, J. Atmos. Sci., 56(2), 127-150.

Bowman, F. M., and J. H. Seinfeld (1994), Ozone productivity of atmospheric organics, J. Geophys. Res.-Atmos., 99(D3), 5309-5324.

Burrows, J. P., E. Holzle, A. P. H. Goede, H. Visser, and W. Fricke (1995), SCIAMACHY - Scanning imaging absorption spectrometer for atmospheric chartography, Acta Astronaut., 35(7), 445-451.

Carmichael, G. R., et al. (2003), Evaluating regional emission estimates using the TRACE-P observations, J. Geophys. Res.-Atmos., 108(D21).

Chameides, W. L., R. W. Lindsay, J. Richardson, and C. S. Kiang (1988), THE ROLE OF BIOGENIC HYDROCARBONS IN URBAN PHOTOCHEMICAL SMOG - ATLANTA AS A CASE-STUDY, Science, 241(4872), 1473-1475.

Chan, C. K., and X. Yao (2008), Air pollution in mega cities in China, Atmos. Environ., 42(1), 1-42.

Choi, Y., Y. H. Wang, T. Zeng, R. V. Martin, T. P. Kurosu, and K. Chance (2005), Evidence of lightning NOx and convective transport of pollutants in satellite observations over North America, Geophys. Res. Lett., 32(2).

Choi, Y., Y. Wang, T. Zeng, D. Cunnold, E. S. Yang, R. Martin, K. Chance, V. Thouret, and E. Edgerton (2008), Springtime transitions of NO_2, CO, and O_3 over North America: Model evaluation and analysis, J. Geophys. Res.-Atmos., 113(D20).

Choi, Y., Y. Wang, Q. Yang, D. Cunnold, T. Zeng, C. Shim, M. Luo, A. Eldering, E. Bucsela, and J. Gleason (2008), Spring to summer northward migration of high O_3 over the western North Atlantic, Geophys. Res. Lett., 35(4).

Chou, C. C. K., C. Y. Tsai, C. J. Shiu, S. C. Liu, and T. Zhu (2009), Measurement of NO(y) during Campaign of Air Quality Research in Beijing 2006 (CAREBeijing-2006): Implications for the ozone production efficiency of NO_x, J. Geophys. Res.-Atmos., 114.

Chou, C. C. K., C. Y. Tsai, C. C. Chang, P. H. Lin, S. C. Liu, and T. Zhu (2011), Photochemical production of ozone in Beijing during the 2008 Olympic Games, Atmos. Chem. Phys., 11(18), 9825-9837.

Cooper, O. R., et al. (2010), Increasing springtime ozone mixing ratios in the free troposphere over western North America, Nature, 463(7279), 344-348.

Costabile, F., A. Amoroso, and F. Wang (2010), Sub-mu m particle size distributions in a suburban Mediterranean area. Aerosol populations and their possible relationship with HONO mixing ratios, Atmos. Environ., 44(39), 5258-5268.

Daum, P. H., L. Kleinman, D. G. Imre, L. J. Nunnermacker, Y. N. Lee, Springston, Sr., L. Newman, and J. Weinstein-Lloyd (2000), Analysis of the processing of Nashville urban emissions on July 3 and July 18, 1995, J. Geophys. Res.-Atmos., 105(D7), 9155-9164.

Dickerson, R. R., S. Kondragunta, G. Stenchikov, K. L. Civerolo, B. G. Doddridge, and B. N. Holben (1997), The impact of aerosols on solar ultraviolet radiation and photochemical smog, Science, 278(5339), 827-830.

Dusanter, S., et al. (2009), Measurements of OH and HO2 concentrations during the MCMA-2006 field campaign – Part 2: Model comparison and radical budget, Atmos. Chem. Phys., 9(18), 6655-6675.

Elshorbany, Y. F., R. Kurtenbach, P. Wiesen, E. Lissi, M. Rubio, G. Villena, E. Gramsch, A. R. Rickard, M. J. Pilling, and J. Kleffmann (2009a), Oxidation capacity of the city air of Santiago, Chile, Atmos. Chem. Phys., 9(6), 2257-2273.

Emmerson, K. M., and M. J. Evans (2009), Comparison of tropospheric gas-phase chemistry schemes for use within global models, Atmos. Chem. Phys., 9(5), 1831-1845.

Emmerson, K. M., N. Carslaw, and M. J. Pilling (2005a), Urban atmospheric chemistry during the PUMA campaign 2: Radical budgets for OH, HO_2 and RO_2, J. Atmos. Chem., 52(2), 165-183.

Emmerson, K. M., N. Carslaw, L. J. Carpenter, D. E. Heard, J. D. Lee, and M. J. Pilling (2005b), Urban atmospheric chemistry during the PUMA campaign 1: Comparison of modelled OH and HO_2 concentrations with measurements, J. Atmos. Chem., 52(2), 143-164.

Febo, A., C. Perrino, and M. Cortiello (1993), A DENUDER TECHNIQUE FOR THE MEASUREMENT OF NITROUS-ACID IN URBAN ATMOSPHERES, Atmospheric Environment Part a-General Topics, 27(11), 1721-1728.

Finlayson-Pitts, B. J. (2009), Reactions at surfaces in the atmosphere: integration of experiments and theory as necessary (but not necessarily sufficient) for predicting the physical chemistry of aerosols, Phys. Chem. Chem. Phys., 11(36), 7760-7779.

Finlayson-Pitts, B. J., L. M. Wingen, A. L. Sumner, D. Syomin, and K. A. Ramazan (2003), The heterogeneous hydrolysis of NO2 in laboratory systems and in outdoor and indoor atmospheres: An integrated mechanism, Phys. Chem. Chem. Phys., 5(2), 223-242.

Fu, T.-M., D. J. Jacob, P. I. Palmer, K. Chance, Y. X. Wang, B. Barletta, D. R. Blake, J. C. Stanton, and M. J. Pilling (2007), Space-based formaldehyde measurements as constraints on volatile organic compound emissions in east and south Asia and implications for ozone, J. Geophys. Res.-Atmos., 112(D6).

Fu, T. M., D. J. Jacob, F. Wittrock, J. P. Burrows, M. Vrekoussis, and D. K. Henze (2008), Global budgets of atmospheric glyoxal and methylglyoxal, and implications for formation of secondary organic aerosols, J. Geophys. Res.-Atmos., 113(D15).

Fu, T. M., et al. (2011), Carbonaceous aerosols in China: top-down constraints on primary sources and estimation of secondary contribution, Atmos. Chem. Phys. Discuss., 11(10), 28219-28272.

Gerecke, A., A. Thielmann, L. Gutzwiller, and M. J. Rossi (1998), The chemical kinetics of HONO formation resulting from heterogeneous interaction of NO2 with flame soot, Geophys. Res. Lett., 25(13), 2453-2456.

Grosjean, D. (2003), Ambient PAN and PPN in southern California from 1960 to the SCOS97-NARSTO, Atmos. Environ., 37, S221-S238.

Grosjean, E., D. Grosjean, L. F. Woodhouse, and Y. J. Yang (2002), Peroxyacetyl nitrate and peroxypropionyl nitrate in Porto Alegre, Brazil, Atmos. Environ., 36(14), 2405-2419.

Guenther, A., T. Karl, P. Harley, C. Wiedinmyer, P. I. Palmer, and C. Geron (2006), Estimates of global terrestrial isoprene emissions using MEGAN (Model of Emissions of Gases and Aerosols from Nature), Atmos. Chem. Phys., 6(11), 3181-3210.

Haagen-Smit, A. J., and Fox, M. M. (1954), Photochemical ozone formation with hydrocarbons and automobile exhaust., Journal of Air Pollution Control Association, 4, 105-109.

Heald, C. L., D. J. Jacob, R. J. Park, L. M. Russell, B. J. Huebert, J. H. Seinfeld, H. Liao, and R. J. Weber (2005), A large organic aerosol source in the free troposphere missing from current models, Geophys. Res. Lett., 32(18), L18809, doi:10.1029/2005GL023831.

Henze, D. K., J. H. Seinfeld, N. L. Ng, J. H. Kroll, T. M. Fu, D. J. Jacob, and C. L. Heald (2008), Global modeling of secondary organic aerosol formation from aromatic hydrocarbons: high- vs. low-yield pathways, Atmos. Chem. Phys., 8(9), 2405-2420.

Ho, S. S. H., and J. Z. Yu (2004), Determination of airborne carbonyls: Comparison of a thermal desorption/GC method with the standard DNPH/HPLC method, Environ. Sci. Technol., 38(3), 862-870.

Hofzumahaus, A., et al. (2009), Amplified Trace Gas Removal in the Troposphere, Science, 324(5935), 1702-1704.

Jacob, D. J. (2000), Heterogeneous chemistry and tropospheric ozone, Atmos. Environ., 34(12-14), 2131-2159.

Jacob, D. J., J. A. Logan, and P. P. Murti (1999), Effect of rising Asian emissions on surface ozone in the United States, Geophys. Res. Lett., 26(14), 2175-2178.

Jenkin, M. E., and K. C. Clemitshaw (2000), Ozone and other secondary photochemical pollutants: chemical processes governing their formation in the planetary boundary layer, Atmos. Environ., 34(16), 2499-2527.

Kanaya, Y., M. Fukuda, H. Akimoto, N. Takegawa, Y. Komazaki, Y. Yokouchi, M. Koike, and Y. Kondo (2008), Urban photochemistry in central Tokyo: 2. Rates and regimes of oxidant (O(3)+NO(2)) production, J. Geophys. Res.-Atmos., 113(D6).

Kanaya, Y., R. Q. Cao, H. Akimoto, M. Fukuda, Y. Komazaki, Y. Yokouchi, M. Koike, H. Tanimoto, N. Takegawa, and Y. Kondo (2007), Urban photochemistry in central Tokyo: 1. Observed and modeled OH and HO2 radical concentrations during the winter and summer of 2004, J. Geophys. Res.-Atmos., 112(D21).

Kanaya, Y., et al. (2009), Rates and regimes of photochemical ozone production over Central East China in June 2006: a box model analysis using comprehensive measurements of ozone precursors, Atmos. Chem. Phys., 9(20), 7711-7723.

Kleffmann, J. (2007), Daytime sources of nitrous acid (HONO) in the atmospheric boundary layer, Chem. Phys. Chem., 8(8), 1137-1144.

Kleffmann, J., T. Gavriloaiei, A. Hofzumahaus, F. Holland, R. Koppmann, L. Rupp, E. Schlosser, M. Siese, and A. Wahner (2005), Daytime formation of nitrous acid: A major source of OH radicals in a forest, Geophys. Res. Lett., 32(5), L05818, doi:10.1029/2005GL022524.

Kleinman, L. I., P. H. Daum, J. H. Lee, Y. N. Lee, L. J. Nunnermacker, S. R. Springston, L. Newman, J. WeinsteinLloyd, and S. Sillman (1997), Dependence of ozone production on NO and hydrocarbons in the troposphere, Geophys. Res. Lett., 24(18), 2299-2302.

Kondo, Y., et al. (2008), Formation and transport of oxidized reactive nitrogen, ozone, and secondary organic aerosol in Tokyo, J. Geophys. Res.-Atmos., 113(D21).

LaFranchi, B. W., et al. (2009), Closing the peroxy acetyl nitrate budget: observations of acyl peroxy nitrates (PAN, PPN, and MPAN) during BEARPEX 2007, Atmos. Chem. Phys., 9(19), 7623-7641.

Lei, W., B. de Foy, M. Zavala, R. Volkamer, and L. T. Molina (2007), Characterizing ozone production in the Mexico City Metropolitan Area: a case study using a chemical transport model, Atmos. Chem. Phys., 7(5), 1347-1366.

Li, X., et al. (2011), Exploring the atmospheric chemistry of nitrous acid (HONO) at a rural site in Southern China, Atmos. Chem. Phys. Discuss., 11(10), 27591-27635.

Li, X., et al. (2012), Exploring the atmospheric chemistry of nitrous acid (HONO) at a rural site in Southern China, Atmos. Chem. Phys., 12(3), 1497-1513.

Liu, S. C., M. Trainer, F. C. Fehsenfeld, D. D. Parrish, E. J. Williams, D. W. Fahey, G. Hubler, and P. C. Murphy (1987), OZONE PRODUCTION IN THE RURAL TROPOSPHERE AND THE IMPLICATIONS FOR REGIONAL AND GLOBAL OZONE DISTRIBUTIONS, J. Geophys. Res.-Atmos., 92(D4), 4191-4207.

Liu, Z., et al. (2010), Evidence of Reactive Aromatics As a Major Source of Peroxy Acetyl Nitrate over China, Environ. Sci. Technol., 44(18), 7017-7022.

Liu, Z., et al. (2012), Summertime photochemistry during CAREBeijing-2007: ROx budgets and O_3 formation, Atmos. Chem. Phys. Discuss., 12(2), 4679-4717.

Lu, K. D., et al. (2010), Oxidant (O_3 + NO_2) production processes and formation regimes in Beijing, J. Geophys. Res.-Atmos., 115, D07303, doi:10.1029/2009JD012714.

Lu, K. D., et al. (2012), Observation and modelling of OH and HO_2 concentrations in the Pearl River Delta 2006: a missing OH source in a VOC rich atmosphere, Atmos. Chem. Phys., 12(3), 1541-1569.

Luke, W. T., P. Kelley, B. L. Lefer, J. Flynn, B. Rappengluck, M. Leuchner, J. E. Dibb, L. D. Ziemba, C. H. Anderson, and M. Buhr (2010), Measurements of primary trace gases and NO_y composition in Houston, Texas, Atmos. Environ., 44(33), 4068-4080.

Mao, J., et al. (2010), Chemistry of hydrogen oxide radicals (HO_x) in the Arctic troposphere in spring, Atmos. Chem. Phys., 10(13), 5823-5838.

Mao, T., Y. S. Wang, J. Jiang, F. K. Wu, and M. X. Wang (2008), The vertical distributions of VOCs in the atmosphere of Beijing in autumn, Sci. Total Environ., 390(1), 97-108.

Marley, N. A., J. S. Gaffney, R. Ramos-Villegas, and B. C. Gonzalez (2007), Comparison of measurements of peroxyacyl nitrates and primary carbonaceous aerosol concentrations in Mexico City determined in 1997 and 2003, Atmos. Chem. Phys., 7(9), 2277-2285.

Martin, R. V., D. J. Jacob, K. Chance, T. P. Kurosu, P. I. Palmer, and M. J. Evans (2003), Global inventory of nitrogen oxide emissions constrained by space-based observations of NO_2 columns, J. Geophys. Res.-Atmos., 108(D17).

Meng, Z., D. Dabdub, and J. H. Seinfeld (1997), Chemical coupling between atmospheric ozone and particulate matter, Science, 277(5322), 116-119.

Molina, M. J., and L. T. Molina (2004), Megacities and atmospheric pollution, J. Air Waste Manage. Assoc., 54(6), 644-680.

Müller, J. F., T. Stavrakou, S. Wallens, I. De Smedt, M. Van Roozendael, M. J. Potosnak, J. Rinne, B. Munger, A. Goldstein, and A. B. Guenther (2008), Global isoprene emissions estimated using MEGAN, ECMWF analyses and a detailed canopy environment model, Atmos. Chem. Phys., 8(5), 1329-1341.

Myriokefalitakis, S., M. Vrekoussis, K. Tsigaridis, F. Wittrock, A. Richter, C. Bruhl, R. Volkamer, J. P. Burrows, and M. Kanakidou (2008), The influence of natural and anthropogenic secondary sources on the glyoxal global distribution, Atmos. Chem. Phys., 8(16), 4965-4981.

NARSTO, 2000: An assessment of tropospheric ozone pollution – A North American perspective. NARSTO Management Office (Envair), Pasco, Washington. http://narsto.org/

NARSTO, 2005: Improving emission inventories for effective Air Quality Management Across North America. NARSTO 05-001. Pasco, Washington, U.S.A.

NRC (National Research Council): Rethinking the ozone problem in urban and regional air pollution, National Academy Press, Washington, D.C., 1991.

Ohara, T., H. Akimoto, J. Kurokawa, N. Horii, K. Yamaji, X. Yan, and T. Hayasaka (2007), An Asian emission inventory of anthropogenic emission sources for the period 1980-2020, Atmos. Chem. Phys., 7(16), 4419-4444.

Palmer, P. I., D. J. Jacob, D. B. A. Jones, C. L. Heald, R. M. Yantosca, J. A. Logan, G. W. Sachse, and D. G. Streets (2003), Inverting for emissions of carbon monoxide from Asia using aircraft observations over the western Pacific, J. Geophys. Res.-Atmos., 108(D21).

Parrish, D. D., D. B. Millet, and A. H. Goldstein (2009), Increasing ozone in marine boundary layer inflow at the west coasts of North America and Europe, Atmos. Chem. Phys., 9(4), 1303-1323.

Pathak, R. K., W. S. Wu, and T. Wang (2009), Summertime PM2.5 ionic species in four major cities of China: nitrate formation in an ammonia-deficient atmosphere, Atmos. Chem. Phys., 9(5), 1711-1722.

Qin, M., P. H. Xie, H. Su, J. W. Gu, F. M. Peng, S. W. Li, L. M. Zeng, J. G. Liu, W. Q. Liu, and Y. H. Zhang (2009), An observational study of the HONO-NO_2 coupling at an urban site in Guangzhou City, South China, Atmos. Environ., 43(36), 5731-5742.

Ramazan, K. A., D. Syomin, and B. J. Finlayson-Pitts (2004), The photochemical production of HONO during the heterogeneous hydrolysis of NO_2, Phys. Chem. Chem. Phys., 6(14), 3836-3843.

Ran, L., C. S. Zhao, F. H. Geng, X. X. Tie, X. Tang, L. Peng, G. Q. Zhou, Q. Yu, J. M. Xu, and A. Guenther (2009), Ozone photochemical production in urban Shanghai, China: Analysis based on ground level observations, J. Geophys. Res.-Atmos., 114.

Ren, X. R., H. Harder, M. Martinez, R. L. Lesher, A. Oliger, T. Shirley, J. Adams, J. B. Simpas, and W. H. Brune (2003), HO_x concentrations and OH reactivity observations in New York City during PMTACS-NY2001, Atmos. Environ., 37(26), 3627-3637.

Richter, A., J. P. Burrows, H. Nuss, C. Granier, and U. Niemeier (2005), Increase in tropospheric nitrogen dioxide over China observed from space, Nature, 437(7055), 129-132.

Roberts, J. M., C. A. Stroud, B. T. Jobson, M. Trainer, D. Hereid, E. Williams, F. Fehsenfeld, W. Brune, M. Martinez, and H. Harder (2001), Application of a sequential reaction model to PANs and aldehyde measurements in two urban areas, Geophys. Res. Lett., 28(24), 4583-4586.

Roberts, J. M., et al. (2007), Measurements of PANs during the New England air quality study 2002, J. Geophys. Res.-Atmos., 112(D20).

Ryerson, T. B., E. J. Williams, and F. C. Fehsenfeld (2000), An efficient photolysis system for fast-response NO_2 measurements, J. Geophys. Res.-Atmos., 105(D21), 26447-26461.

Sander, S. P.; Friedl, R. R.; Golden, D. M.; Kurylo, M. J.; Moortgat, G. K.; Keller–Rudek, H.; Wine, P. H.; Ravishankara, A. R.; Kolb, C. E.; Molina, M. J.; Finlayson–Pitts, B. J.; Huie, R. E.; Orkin, V. L. Chemical kinetics and photochemical data for use in atmospheric studies, Evaluation Number 15, JPL Publication 06–02, 2006; Jet Propulsion Laboratory, Pasadena, CA, USA.

Sander, S. P., J. Abbatt, J. R. Barker, J. B. Burkholder, R. R. Friedl, D. M. Golden, R. E. Huie, C. E. Kolb, M. J. Kurylo, G. K. Moortgat, V. L. Orkin and P. H. Wine "Chemical Kinetics and Photochemical Data for Use in Atmospheric Studies, Evaluation No. 17," JPL Publication 10-6, Jet Propulsion Laboratory, Pasadena, 2011 http://jpldataeval.jpl.nasa.gov.

Sarwar, G., R. Zhang, J. C. H. Fung, and A. K. H. Lau (2011), Examining the impact of a new aromatic chemistry on air quality model predictions over the Pearl River Delta region, China, Conference on air quality and climate, Kona, Hawaii.

Shao, M., S. H. Lu, Y. Liu, X. Xie, C. C. Chang, S. Huang, and Z. M. Chen (2009), Volatile organic compounds measured in summer in Beijing and their role in ground-level ozone formation, J. Geophys. Res.-Atmos., 114.

Shim, C., Y. H. Wang, Y. Choi, P. I. Palmer, D. S. Abbot, and K. Chance (2005), Constraining global isoprene emissions with Global Ozone Monitoring Experiment (GOME) formaldehyde column measurements, J. Geophys. Res.-Atmos., 110(D24).

Shirley, T. R., et al. (2006), Atmospheric oxidation in the Mexico City Metropolitan Area (MCMA) during April 2003, Atmos. Chem. Phys., 6(9), 2753-2765.

Sillman, S., J. A. Logan, and S. C. Wofsy (1990), The sensitivity of ozone to nitrogen-oxides and hydrocarbons in regional ozone episodes, J. Geophys. Res.-Atmos., 95(D2), 1837-1851.

Slusher, D. L., L. G. Huey, D. J. Tanner, F. M. Flocke, and J. M. Roberts (2004), A thermal dissociation-chemical ionization mass spectrometry (TD-CIMS) technique for the simultaneous measurement of peroxyacyl nitrates and dinitrogen pentoxide, J. Geophys. Res.-Atmos., 109(D19).

Song, Y., M. Shao, Y. Liu, S. H. Lu, W. Kuster, P. Goldan, and S. D. Xie (2007), Source apportionment of ambient volatile organic compounds in Beijing, Environ. Sci. Technol., 41(12), 4348-4353.

Stavrakou, T., J. F. Muller, I. De Smedt, M. Van Roozendael, M. Kanakidou, M. Vrekoussis, F. Wittrock, A. Richter, and J. P. Burrows (2009), The continental source of glyoxal estimated by the synergistic use of spaceborne measurements and inverse modelling, Atmos. Chem. Phys., 9(21), 8431-8446.

Streets, D. G., et al. (2003), An inventory of gaseous and primary aerosol emissions in Asia in the year 2000, J. Geophys. Res.-Atmos., 108(D21).

Stutz, J., B. Alicke, and A. Neftel (2002), Nitrous acid formation in the urban atmosphere: Gradient measurements of NO2 and HONO over grass in Milan, Italy, J. Geophys. Res.-Atmos., 107(D22).

Su, H., Y. F. Cheng, M. Shao, D. F. Gao, Z. Y. Yu, L. M. Zeng, J. Slanina, Y. H. Zhang, and A. Wiedensohler (2008), Nitrous acid (HONO) and its daytime sources at a rural site during the 2004 PRIDE-PRD experiment in China, J. Geophys. Res.-Atmos., 113(D14).

Tanimoto, H., T. Ohara, and I. Uno (2009), Asian anthropogenic emissions and decadal trends in springtime tropospheric ozone over Japan: 1998-2007, Geophys. Res. Lett., 36, L23802, doi:10.1029/2009GL041382.

Thornton, J., and J. P. D. Abbatt (2005), Measurements of HO_2 uptake to aqueous aerosol: Mass accommodation coefficients and net reactive loss, J. Geophys. Res.-Atmos., 110(D8).

Thornton, J. A., L. Jaegle, and V. F. McNeill (2008), Assessing known pathways for HO_2 loss in aqueous atmospheric aerosols: Regional and global impacts on tropospheric oxidants, J. Geophys. Res.-Atmos., 113(D5).

van Donkelaar, A., R. V. Martin, M. Brauer, R. Kahn, R. Levy, C. Verduzco, and P. J. Villeneuve (2010), Global Estimates of Ambient Fine Particulate Matter Concentrations from Satellite-Based Aerosol Optical Depth: Development and Application, Environ. Health Perspect., 118(10), 847-855.

Villena, G., J. Kleffmann, R. Kurtenbach, P. Wiesen, E. Lissi, M. A. Rubio, G. Croxatto, and B. Rappengluck (2011), Vertical gradients of HONO, NO_x and O_3 in Santiago de Chile, Atmos. Environ., 45(23), 3867-3873.

Vogel, B., H. Vogel, J. Kleffmann, and R. Kurtenbach (2003), Measured and simulated vertical profiles of nitrous acid - Part II. Model simulations and indications for a photolytic source, Atmos. Environ., 37(21), 2957-2966.

Volkamer, R., L. T. Molina, M. J. Molina, T. Shirley, and W. H. Brune (2005), DOAS measurement of glyoxal as an indicator for fast VOC chemistry in urban air, Geophys. Res. Lett., 32(8), L08806, doi:10.1029/2005GL022616.

Volkamer, R., P. Sheehy, L. T. Molina, and M. J. Molina (2010), Oxidative capacity of the Mexico City atmosphere - Part 1: A radical source perspective, Atmos. Chem. Phys., 10(14), 6969-6991.

Vrekoussis, M., F. Wittrock, A. Richter, and J. P. Burrows (2009), Temporal and spatial variability of glyoxal as observed from space, Atmos. Chem. Phys., 9(13), 4485-4504.

Vrekoussis, M., F. Wittrock, A. Richter, and J. P. Burrows (2010), GOME-2 observations of oxygenated VOCs: what can we learn from the ratio glyoxal to formaldehyde on a global scale?, Atmos. Chem. Phys., 10(21), 10145-10160.

Wang, T., A. J. Ding, J. Gao, and W. S. Wu (2006), Strong ozone production in urban plumes from Beijing, China, Geophys. Res. Lett., 33(21), L21806, doi:10.1029/2006GL027689.

Wang, T., X. L. Wei, A. J. Ding, C. N. Poon, K. S. Lam, Y. S. Li, L. Y. Chan, and M. Anson (2009), Increasing surface ozone concentrations in the background atmosphere of Southern China, 1994-2007, Atmos. Chem. Phys., 9(16), 6216-6226.

Wang, T., et al. (2010), Air quality during the 2008 Beijing Olympics: secondary pollutants and regional impact, Atmos. Chem. Phys., 10(16), 7603-7615.

Wang, X. M., G. Y. Sheng, J. M. Fu, C. Y. Chan, S. G. Lee, L. Y. Chan, and Z. S. Wang (2002), Urban roadside aromatic hydrocarbons in three cities of the Pearl River Delta, People's Republic of China, Atmos. Environ., 36(33), 5141-5148.

Wang, Y., Y. Choi, T. Zeng, D. Davis, M. Buhr, L. G. Huey, and W. Neff (2007), Assessing the photochemical impact of snow NOx emissions over Antarctica during ANTCI 2003, Atmos. Environ., 41(19), 3944-3958.

Wang, Y., M. B. McElroy, J. W. Munger, J. Hao, H. Ma, C. P. Nielsen, and Y. Chen (2008), Variations of O_3 and CO in summertime at a rural site near Beijing, Atmos. Chem. Phys., 8(21), 6355-6363.

Wang, Y. H., Y. S. Choi, T. Zeng, B. Ridley, N. Blake, D. Blake, and F. Flocke (2006), Late-spring increase of trans-Pacific pollution transport in the upper troposphere, Geophys. Res. Lett., 33(1), L01811, doi:10.1029/2005GL024975.

Wang, Y. X., M. B. McElroy, R. V. Martin, D. G. Streets, Q. Zhang, and T. M. Fu (2007), Seasonal variability of NO(x) emissions over east China constrained by satellite observations: Implications for combustion and microbial sources, J. Geophys. Res.-Atmos., 112(D6).

Wentzell, J. J. B., C. L. Schiller, and G. W. Harris (2010), Measurements of HONO during BAQS-Met, Atmos. Chem. Phys., 10(24), 12285-12293.

Wilkening, K. E., L. A. Barrie, and M. Engle (2000), Atmospheric science - Trans-Pacific air pollution, Science, 290(5489), 65-67.

Wittrock, F., A. Richter, H. Oetjen, J. P. Burrows, M. Kanakidou, S. Myriokefalitakis, R. Volkamer, S. Beirle, U. Platt, and T. Wagner (2006), Simultaneous global observations of glyoxal and formaldehyde from space, Geophys. Res. Lett., 33(16), L16804, doi:10.1029/2006GL026310.

Wong, K. W., C. Tsai, B. Lefer, C. Haman, N. Grossberg, W. H. Brune, X. Ren, W. Luke, and J. Stutz (2011), Daytime HONO Vertical Gradients during SHARP 2009 in Houston, TX, Atmos. Chem. Phys. Discuss., 11(8), 24365-24411.

Wong, K. W., C. Tsai, B. Lefer, C. Haman, N. Grossberg, W. H. Brune, X. Ren, W. Luke, and J. Stutz (2012), Daytime HONO vertical gradients during SHARP 2009 in Houston, TX, Atmos. Chem. Phys., 12(2), 635-652.

Wood, E. C., et al. (2009), A case study of ozone production, nitrogen oxides, and the radical budget in Mexico City, Atmos. Chem. Phys., 9(7), 2499-2516.

Yang, Q., Wang, Y. H., Zhao, C., Liu, Z., Gustafson, W. I. J., and Shao, M.: NOx emission reduction and its effects on ozone during the 2008 Olympic Games, Environ. Sci. Technol., 45, 6404–6410, doi:10.1021/es200675v.

Yu, Y., B. Galle, A. Panday, E. Hodson, R. Prinn, and S. Wang (2009), Observations of high rates of NO_2-HONO conversion in the nocturnal atmospheric boundary layer in Kathmandu, Nepal, Atmos. Chem. Phys., 9(17), 6401-6415.

Zhang, J., T. Wang, W. L. Chameides, C. Cardelino, J. Kwok, D. R. Blake, A. Ding, and K. L. So (2007), Ozone production and hydrocarbon reactivity in Hong Kong, Southern China, Atmos. Chem. Phys., 7, 557-573.

Zhang, J. M., et al. (2009), Continuous measurement of peroxyacetyl nitrate (PAN) in suburban and remote areas of western China, Atmos. Environ., 43(2), 228-237.

Zhang, L., D. J. Jacob, M. Kopacz, D. K. Henze, K. Singh, and D. A. Jaffe (2009), Intercontinental source attribution of ozone pollution at western US sites using an adjoint method, Geophys. Res. Lett., 36, L11810, doi:10.1029/2009GL037950

Zhang, N., X. L. Zhou, P. B. Shepson, H. L. Gao, M. Alaghmand, and B. Stirm (2009), Aircraft measurement of HONO vertical profiles over a forested region, Geophys. Res. Lett., 36, L15820, doi:10.1029/2009GL038999.

Zhang, Q., et al. (2007), NO(x) emission trends for China, 1995-2004: The view from the ground and the view from space, J. Geophys. Res.-Atmos., 112(D22).

Zhang, Q., et al. (2009), Asian emissions in 2006 for the NASA INTEX-B mission, Atmos. Chem. Phys., 9(14), 5131-5153.

Zhang, X., Z. M. Chen, S. Z. He, W. Hua, Y. Zhao, and J. L. Li (2010), Peroxyacetic acid in urban and rural atmosphere: concentration, feedback on PAN-NO(x) cycle and implication on radical chemistry, Atmos. Chem. Phys., 10(2), 737-748.

Zhang, Y. H., et al. (2008), Regional ozone pollution and observation-based approach for analyzing ozone-precursor relationship during the PRIDE-PRD2004 campaign, Atmos. Environ., 42(25), 6203-6218.

Zhao, C., and Y. H. Wang (2009), Assimilated inversion of NO_x emissions over east Asia using OMI NO_2 column measurements, Geophys. Res. Lett., 36, L0680510.1029/2008gl037123, 2009.

Zhao, C., Y. H. Wang, and T. Zeng (2009a), East China Plains: A "Basin" of Ozone Pollution, Environ. Sci. Technol., 43(6), 1911-1915.

Zhao, C., Y. Wang, Y. Choi, and T. Zeng (2009b), Summertime impact of convective transport and lightning NO_x production over North America: modeling dependence on meteorological simulations, Atmos. Chem. Phys., 9(13), 4315-4327.

Zhao, Y., C. P. Nielsen, Y. Lei, M. B. McElroy, and J. Hao (2011), Quantifying the uncertainties of a bottom-up emission inventory of anthropogenic atmospheric pollutants in China, Atmos. Chem. Phys., 11(5), 2295-2308.

Zhou, X. L., K. Civerolo, H. P. Dai, G. Huang, J. Schwab, and K. Demerjian (2002), Summertime nitrous acid chemistry in the atmospheric boundary layer at a rural site in New York State, J. Geophys. Res.-Atmos., 107(D21).

Zhou, X. L., et al. (2011), Nitric acid photolysis on forest canopy surface as a source for tropospheric nitrous acid, Nat. Geosci., 4(7), 440-443.

Zhu, T., X. Li, M. Hu, X. Y. Tang, and T. Carebeijing (2009), Air Pollution Characteristics Before, During, and After the Beijing Olympics, Epidemiology, 20(6), S250-S250.

Ziemba, L. D., J. E. Dibb, R. J. Griffin, C. H. Anderson, S. I. Whitlow, B. L. Lefer, B. Rappengluck, and J. Flynn (2010), Heterogeneous conversion of nitric acid to nitrous acid on the surface of primary organic aerosol in an urban atmosphere, Atmos. Environ., 44(33), 4081-4089.

VITA

Zhen Liu

Zhen Liu was born in Xinyang, Henan, China. He received a B.E. in Environmental Engineering from Yanshan University, Qinhuangdao, Hebei, China in 2004 and a M.S. in Environmental Sciences from Peking University, Beijing, China in 2008 before coming to Georgia Tech to pursue a doctorate in Atmospheric Sciences. When he is not working on his research, Mr. Liu enjoys singing, playing guitar and badminton.